DISS. ETH NR. 27773

Charged Lepton Flavour Violation Search and Exotic Physics with the MEG II Apparatus

Positron Beam Calibration Methods, MEG II Spectrometer Characterisation and Towards a Prototype for Future High Precision Calorimetry

A thesis submitted to attain the degree of

DOCTOR OF SCIENCES of ETH ZÜRICH

(Dr. sc. ETH Zürich)

presented by

PATRICK SCHWENDIMANN

MSc ETH Physics
born on 26.12.1989
from Pohlern BE

accepted on the recommendation of

Prof. Dr. Klaus Kirch
Prof. Dr. Günther Dissertori
Prof. Dr. Angela Papa

2021

Abstract

The Standard Model (SM) of particle physics is the most fundamental theory currently available to describe the nature of the matter around us and the forces it interacts with. If including neutrino oscillations in the model, it withstood all experimental tests and no significant deviations were found until now. Some anomalies were observed however, which do not suffice to claim new discoveries yet, but can be considered hints towards possible directions to find new physics. There is no debate that new physics is needed due to cosmological observations such as dark matter or the matter-antimatter asymmetry in the universe.

The search for the Charged Lepton Flavour Violating (cLFV) $\mu \to e\gamma$ decay started shortly after the discovery of the muon. It provides an excellent opportunity to search for evidence of yet undiscovered physics due to the well understood SM decay channels of the muon. The most recent upper limit on the branching ratio $BR(\mu \to e\gamma) < 4.2 \times 10^{-13}$ at 90 % confidence level (C.L.) is provided by the MEG experiment [1]. The upgraded MEG II experiment [2] is currently in the commissioning phase. It aims to search for this decay with an improved sensitivity to a BR down to 6×10^{-14}.

As part of this work, the code for the spectrometer calibration based on Mott scattered positrons has been adapted to the new apparatus and extended to the timing counter. The analysis codes have been proven to be working based on simulations. They allow to gather information about the resolutions obtainable in positron momentum vector and time by the spectrometer.

Further, extensive simulations on new scintillating materials coupled to state of the art Silicon PhotoMultipliers (SiPMs) were performed. In the direct comparison, LYSO performs better than $LaBr_3$(Ce) for the currently available crystal sizes. For 55 MeV photons, an energy resolution below 2 %, a time resolution of 30 ps and a position resolution of the order of a few mm is obtained for available crystal sizes.

A prototype using a LYSO crystal will soon be built and tested as an auxiliary detector for MEG II. It will represent an upgrade of the tagging detector used for the charge exchange reaction calibration method (CEX calibration), crucial to assess the detector performances of the LXe calorimeter, a prototype for future large high performance calorimeters working at this energy scale and a first auxiliary detector to investigate new physics channels with the MEG II detector.

Moreover, two additional processes that can be investigated with the MEG II apparatus are discussed. They provide an extension to the MEG II physics programme. The first option is to search for the decay $\mu \to eX$ with a yet unknown and elusive boson X in the vast amount of ordinary muon decay data acquired as part of the $\mu \to e\gamma$ searches. The simulations done for this purpose underline the importance of precise theoretical predictions as well as detailed calibration of the detector. Given these, MEG II should reach a competitive sensitivity to a BR below 1×10^{-5} with about 10^7 to 10^8 reconstructed events.

The second physics result studied as part of this work is an independent measurement of the beryllium anomaly. It was observed by a Hungarian group at Atomki [3] and still lacks an independent confirmation by a different experiment. As shown with simulations in this thesis, the MEG II apparatus could provide such a confirmation or exclude their claimed region. This requires only a minor adaptation of the experimental setup and could provide sufficient data within a few days of physics data acquisition.

Zusammenfassung

Das Standardmodell (SM) der Teilchenphysik stellt zur Zeit die grundlegenste Theorie über die uns umgebende Materie sowie deren Wechselwirkungen dar. Wenn man Neutrinooszillationen im Modell einschliesst, hielt das SM allen experimentellen Überprüfungen stand und es wurden keine aussagekräftigen Abweichungen festgestellt. Dennoch gibt es kleinere Ungereimtheiten, die als solche nicht die Behauptung rechtfertigen, man habe Physik jenseits des SM gefunden. Jedoch kann man diese als Hinweise sehen, in welcher Richtung man möglicherweise solche neuen, physikalischen Phänomene finden kann. Denn es steht ausser Frage, dass das SM kosmologische Beobachtungen wie das Verhältnis von Materie zu Antimaterie im Universum oder die Existenz von Dunkler Materie nicht erklären kann.

Die Suche nach dem leptonfamilienzahlverletzenden Zerfall $\mu \to e\gamma$ begann schon kurz nach der Myonentdeckung. Dieser bietet aufgrund der wohlverstandenden Natur der Myonenzerfälle

im SM eine ausgezeichnete Gelegenheit für die Suche nach bislang unentdeckter Physik. Die letzte Messung durch das MEG Experiment ergibt bei einem 90 % Vertrauensintervall, dass nicht mehr als 4.2×10^{-13} aller Myonen neutrinolos in ein Positron und ein Photon zerfallen [1]. Das erklärte Ziel des MEG II Experiment ist es, dieses Resultat deutlich zu verbessern und mit einer Empfindlichkeit von 6×10^{-14} nach diesem unterdrückten Zerfall zu suchen.

Als Teil dieser Arbeit wurde der Programmcode, welcher für die Eichung des Spektrometers mittels Mottstreuung von Positronen verwendet wird, den neuen Gegebenheiten des verbesserten MEG II Experiments angepasst und erweitert. Neu umfasst diese Methode auch den Zeitzähler des Spektrometers und Simulationen ergaben, dass die entsprechenden Methoden funktionieren und Informationen zum Auflösungsvermögen des Spektrometers im vektoriellen Positronimpuls sowie in der Positronzeit liefert.

Des Weiteren wurden neue Szintillatormaterialien simuliert, welche an eine Vielzahl von siliziumbasierten Photomultiplikatoren gekoppelt und so ausgelesen wurden. Im direkten Vergleich zeigte sich klar, dass die zur Zeit verfügbaren LYSO-Kristalle den entsprechenden $LaBr_3(Ce)$ Kristallen überlegen sind. Die Simulationen ergaben eine Energieauflösung unter 2 %, eine Zeitauflösung um die 30 ps und eine Positionsauflösung von einigen wenigen mm für 55 MeV Photonen.

In naher Zukunft wird ein Prototyp mit einem LYSO-Kristall gebaut und als Hilfsdetektor beim MEG II Experiment getestet. Dies stellt eine Verbesserung bei der Identifizierung geeigneter Ereignisse für die auf Ladungsaustausch basierende Eichung des Flüssigxenonkalorimeters dar, welche entscheidend zur Bestimmung des Leistungsvermögen des Kalorimeters beiträgt. Zusätzlich handelt es sich um einen Prototypen für zukünftige Hochleistungsdetektoren in diesem Energiebereich, sowie um einen Detektor, mit dem man neue Zerfallskanäle beim MEG II Experiment untersuchen kann.

Ferner werden zwei weitere Phänomene beschrieben, die ebenfalls mit dem MEG II Versuchsaufbau untersuchbar sind. Diese bieten eine attraktive Erweiterung des Physikprogramms des Experiments. Einerseits bietet sich die Möglichkeit, nach dem Zerfall $\mu \to eX$ mit einem bislang unbekannten und schwer messbarem Boson X in den Myonzerfallsdaten zu suchen, welche während der Suche nach dem $\mu \to e\gamma$ Zerfall aufgezeichnet worden sein werden. Die dazu durchgeführten Simulationen berkäftigen die Wichtigkeit von präzisen Theorievorhersagen und genauen Eichungen der Detektoren. Sind diese gegeben, kann MEG II mit 10^7 bis 10^8 vermessenen Myonenzerfällen eine Empfindlichkeit von unter 1 in 10^5 so zerfallenen Myonen erreichen.

Das zweite Physikresultat, das hier beschrieben wird, ist eine Überprüfung der so genannten Berylliumanomalie, die auf eine ungarische Gruppe am Atomki zurückgeht [3]. Bislang mangelt es an einer unabhängigen Bestätigung durch ein weiteres Experiment. Wie mittels Simulationen in dieser Arbeit gezeigt wird, kann man mit dem MEG II Versuschsaufbau unter minimalen Anpassungen innert weniger Tagen Messzeit genügend Daten erheben, um eine solche Bestätigung zu liefern oder deren Behauptung entkräften.

Acknowledgements

I would like to express my deepest thanks to my supervisor Angela Papa for the discussions about the results obtained from simulation, for the support in pursuing my goals, for the experiences shared in the experimental hall, for the leisure talks in the breaks and lastly for the meals shared at the end of long days of beam time.

Further, I thank Stefan Ritt, head of the muon group at PSI, for his help and support in all matters related to working on MEG and at PSI. No matter the circumstances, he would always be there when his help was needed. Furthermore I want to acknowledge his great support on the matter described in the chapter about the detector hut temperature control.

Then I would like to thank my academic thesis supervisor and head of the laboratory for particle physics at PSI, Klaus Kirch. In our regular discussions, he managed to give a kind feedback on the progress and was able to ask the right question that needed to be answered next. It was a pleasure to benefit from his experience.

I am very grateful to these three people that I was given the chance to work at PSI as part of the MEG II collaboration. This allowed me to deepen my knowledge of what it means to be an experimentalist and expand my experiences in- and outside of the field.

Moreover, I want to express my gratitude to the MEG II Collaborators. They provided an international environment and enriched my cultural experiences, be it at a conference in Italy or at

a collaboration meeting in Tokyo. Furthermore, they provided valuable discussions on the topics of my work and expanded my views thereby. In particular, I want to acknowledge the help of Yusuke Uchiyama for his valuable support on the MEG II computational resources and software as well as the Italian colleagues Marco Chiappini, Marco Francesconi, Luca Galli, Manuel Meucci and Francesco Renga regularly encountered in the experimental hall that would eagerly lend a hand if required.

In the context of the temperature control of the detector hut, the valuable help from the electronics pool has to be acknowledged. My thanks go in particular to Ueli Hartmann for providing electronic devices and drawing the schemata. In general, the help from the whole group has to be acknowledged for their various and crucial contributions to many aspects of the experiment that eventually affected my work.

The studies performed on the Majoron search were heavily supported by the theory group at PSI. In particular I was supported by Andrea Gurgone and Yannick Ulrich. They provided the tables used as theory input to the simulations shown in this work. Further I want to thank them for their endeavours to explain the main concepts of the theory to me.

Further, the development of program code, which is included in almost every aspect of the thesis, benefited highly from contributions of countless members of various online communities. These include the people posting problems and those that provide solutions for example on the ROOT forums or the GEANT4 forums as well as on platforms like `stackoverflow.com`. This further includes all the helpful people that prepared small code snippets to illustrate the proper use of commands and offer them to the public as examples and inspiration.

Then I would like to thank to the former and current members of the muon group as well as our quasi-permanent guests. They were available for discussions about topics of the work, topics related to work and topics not related to work as well. In particular I want to thank Aldo for raising the mood when needed and always knowing the right person, Anna for the appreciated cups of tea and her well equipped toolbox, Laura for organising group hikes, Stella for the random laughs shared and Ivana for the Miaus shared. A special thanks goes to the fellow PhD students with whom we were making ice cream during the hot summer days.

Although not directly related to the work described in this thesis, the whole collaboration in general and me in particular benefited from tremendous support by the various technicians from each group at PSI. They would readily help with whatever problem occurred, starting from liquid helium supply to issues with vacuum pumps, craning of heavy equipment or last minute production of small parts. Their “Keis Problem” (No Problem) or “Chönd mer mache” (We can do that) and similar statements were soothing balm on the soul in stressful beam times.

Then I am very grateful to Anita van Loon who took care of the administrative aspects that came with the employment at PSI in a very efficient and organised manner. She would assist with whatever task came up including the organisation of flights or applying for a visa. I am fully convinced that my time as PhD student at PSI would not have been anywhere near as smooth and coordinated without her.

Further I want to express my deep appreciation for the huge effort by my girlfriend Jasmin Stoff in proofreading the whole thesis and finding typos as well as badly explained passages. Additionally, I want thank my supervisor Angela Papa for reading the thesis and suggesting scientific improvements amongst others. Then I am grateful to Jonas Nuber who offered his opinion and suggestions on potential improvements for parts of the thesis.

Moreover, I am grateful to Klaus Kirch and Günther Dissertori for their suggestions and comments that allowed to make the thesis better understandable for someone not working on the topics on a daily basis as well as the additional typos they identified.

Another great thanks goes to my family members that greatly supported me in my career. In particular, I am grateful to my grandfather Fritz who brought me to the path of science but unfortunately did not live long enough to witness the completion of this thesis. Further, I am thankful to my grandmother Ruth, who is still an excellent cook despite her old age, my father Andreas and my siblings Stephan and Seraina for their support during my years of study.

Finally, I want to thank to Anna, Felix, Giovanni, Jasmin, Lukas, Nick and Patricia with whom I regularly played DnD during the COVID pandemic if beam time allowed it. This allowed for a minimal amount of urgently needed social interaction in this difficult times with a lot of restrictions and limited possibilities, during the last one and a half year of my PhD research time. Let the good dice roll!

Contents

List of Figures

List of Tables

Part I

Introduction

Chapter 1

Charged Lepton Flavour Violation Searches

1.1 A Brief Introduction to the Standard Model of Particle Physics

This section provides a brief overview of the Standard Model (SM) of particle physics. In addition, a few selected observations are presented that could potentially be interpreted as hints towards physics beyond the SM.

From ancient times, humans sought to understand the nature of their surroundings. Through the ages, new explanations and descriptions of what we can observe were given. Models were created, tested through experiments and compared to observations. Hypotheses were then either advanced with the new findings or rejected due to shortcomings in explaining them.

With the discovery of new aspects of nature, new fields of research were opened and new hypotheses created. With improved technologies, developed through these advanced research, it was possible to push further and further and on the quest for new physics, knowledge was gained that revolutionised the life of humankind.

The last century was exceptionally fruitful in terms of scientific advancements. Amongst countless other improvements, one was trying to understand the most fundamental nature of our surroundings. According to our latest understanding, all the matter around us consists of so called fundamental particles such as electrons and quarks that interact through fundamental forces. Their interplay is described by what is called the Standard Model (SM) of particle physics.

The SM is a collection of countless contributions and the most advanced theoretical model to describe the behaviour of the observed particles. It describes all observables by a set of fundamental particles and their interactions. At this point, it is noteworthy, that what an ordinary person understands as a particle is treated as an excitation of a corresponding quantum field by the theory.

The particles can be grouped in two main groups. On the one hand there are bosons characterised by an integer spin. On the other hand, there are fermions characterised by a spin $\frac{1}{2}$. Fermions are further separated in leptons and quarks. Please check Figure 1.1 for a graphical representation of these particles.

The elementary bosons are the Higgs boson (H) and the gauge bosons (g, γ, $W^{\pm}$, Z). Through interaction with the Higgs field, the other particles acquire their masses. The gauge bosons are the mediators of the three fundamental forces included in the SM.

The strong force is mediated by gluons. It couples to the colour-charge of particles such as quarks. Gluons can actually interact with themselves which limits the range of the strong force despite the massless mediator. Moreover, the strength of the strong force increases at lower energies or larger distances. This leads to the fact that the energy added when separating quarks is sufficient to create quark-antiquark pairs and cause the separating quarks to form individual hadrons. This process is referred to as hadronisation.

The massless photon γ serves as mediator for the electromagnetic force. This replaces the electric and magnetic fields known from classical physics. It couples to the electrically charged particles.

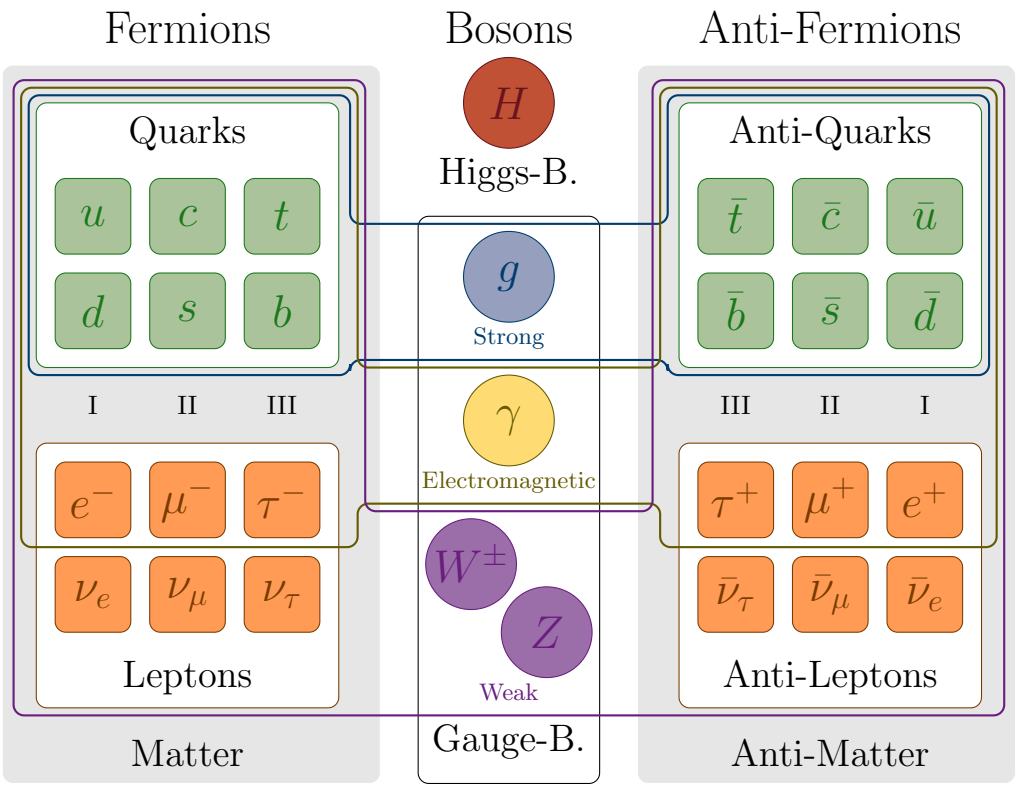

Figure 1.1: Particles of the Standard Model. The roman numerals refer to the family or generation of leptons and quarks. Note that the antifermions are in fact fermions as well. This distinction was made to underline the fact that for each fermion particle, there is a "mirrored" anti-particle. Detailed description in the text.

Having massless mediators that do not directly interact with themselves, the electromagnetic force is the only force in the SM that has an infinite reach. This allows light to travel throughout the whole universe.

The weak force is mediated by the $W^{\pm}$ and Z bosons. These are massive particles, i.e. particles that couple strongly to the Higgs. The mass of these particles limits the range of the weak force which is thus only short ranged. In combination with the photon, it is referred to as the electro-weak interaction and unified theories for these two forces are available [4, 5].

The known leptons are the electron (e^-), muon (μ^-) and tau (τ^-) with their corresponding neutrino (ν_e, ν_μ, ν_τ) and for each of them the corresponding antiparticle (e^+, μ^+, τ^+, $\bar{\nu}_e$, $\bar{\nu}_\mu$, $\bar{\nu}_\tau$). While the charged leptons ($e^{\pm}$, $\mu^{\pm}$, $\tau^{\pm}$) may interact either with the weak force or the electromagnetic force, the electrically uncharged neutrinos may only interact via the weak force.

The electron and electron neutrino in combination with their corresponding antiparticles form the first lepton family. The muon and its corresponding particles form the second family and the third family consists of the tau and its associated particles. Note that the theory of the electro-weak interaction does not allow the mixing of lepton flavours, i.e. the number of leptons of a family is predicted to be conserved.

The known quarks are up u, down d, strange s, charm c, bottom or beauty b and top t as well as their antiparticles. While the up-types (u, c and t) have an electric charge of $\frac{2}{3}$, the down types (d, s, b) have a charge of $-\frac{1}{3}$. Opposed to leptons, quarks carry a colour-charge and thus are able to interact with all fundamental forces.

Due to the nature of the strong force, quarks always form hadrons. They can either form mesons consisting of a quark and an antiquark or baryons that consist of three quarks respectively three antiquarks for an antibaryon. The most notable baryons are the proton (uud) and the neutron (udd).

In the SM both the number of leptons and the number of baryons is conserved when assigning a negative number to antiparticles. This immediately hints for a shortcoming as this allows for the

production of a baryon only under simultaneous production of an antibaryon and the same goes for leptons. This suggests that the amount of matter and antimatter in the universe should be equal, yet only negligible amounts of antimatter are found.

For each of the particles in the SM, there is a set of defined propagators that define how this particle moves through time and space as well as matrix elements that define the interactions between the particles. Knowing them all through measurements, the SM allows precise predictions from the magnetic moments of electrons, to various muon decays up to the behaviour of particle collisions and subsequent decays at the large hadron collider.

Ever since the SM was established, its predictions matched with the experimental results. With the discovery of the Higgs particle in 2012 [6, 7], the last missing piece was found. Thus the SM is complete and appears to explain how the matter around us works.

However, as already hinted at before, even this highly sophisticated model has its shortcomings. It completely fails to explain certain phenomena that are not observed in the laboratory but when one is looking upwards into the depth of the universe. There is clearly more matter out there than antimatter. According to the SM, no such clear asymmetry is supposed to exist. Furthermore, the evidence of dark matter is rather well established while the Standard Model offers no explanation.

In addition to these cosmological observables, there are a few indicators that suggest the existence of new physics beyond the SM. A well established fact that goes against SM predictions are neutrino oscillations [8, 9, 10]. This proves lepton flavour violation in the neutrino sector.

Further, some recent measurements with B-Mesons may suggest that differences from the SM predictions potentially could exist [11]. Neither of them however reaches the necessary significance to back the claim for the existence of new physics. Additionally, a 4.2σ deviation was measured for the muon anomalous magnetic moment [12], which would indicate that there are contributions of so far unknown physics missing in the theoretical prediction.

1.2 Charged Lepton Flavour Violation - a Possible Access to new Physics

This section outlines why Charged Lepton Flavour Violation (cLFV) is a crucial sector to test the SM on. Moreover, potential channels that would imply physics beyond the SM are discussed. Special focus is given to the $\mu \to e\gamma$ decay channel.

These anomalies could be taken as hints towards the existence of not yet discovered physics and potentially imply the existence of new particles. To unveil such new particles, one can either directly detect them or find evidence in the form of deviations between measurements and SM predictions. These deviations occur due to virtual contributions to intermediate states that will potentially affect several processes simultaneously. To find such a deviation, one needs on the one hand the experiment to perform the high precision measurement and on the other hand an outstanding theoretical prediction of the SM value.

For this reason, charged lepton flavour violating processes are of extraordinary interest. The SM offers a description of the electroweak interaction that is well understood and allows high precision predictions. Moreover, in the SM on its own, the lepton flavour number is a conserved quantity. This means, that not only the total number of leptons stays the same but the number of first (e, ν_e), second (μ, ν_μ) and third (τ, μ_τ) generation leptons are individually conserved.

That this is actually wrong was shown when observing neutrino oscillations [8, 9, 10]. Still, given the extremely small neutrino masses compared to the W boson mass, the charged lepton flavour mixing is highly suppressed and so are charged lepton flavour violating processes. These include various decay channels for muons or taus or conversions of these particles to a charged lepton of a different generation.

This makes the investigation of physics with either muons or taus worthwhile. Muons are lighter, comparably long-lived and easier to handle. It is easily possible to guide them from production to an experiment and stop them to observe muon decays at rest. Due to their low mass, the potential number of decay channels is minimal. Taus on the other side are heavier and decay within a short time. They decay through a host of leptonic and hadronic decay channels. Their larger rest energy however may enhance the probability to interact with heavier, so far undiscovered particles.

When investigating for Charged Lepton Flavour Violation (cLFV) with muons, there are basically three channels to investigate. First, there is the decay of the anti-muon into a positron and a

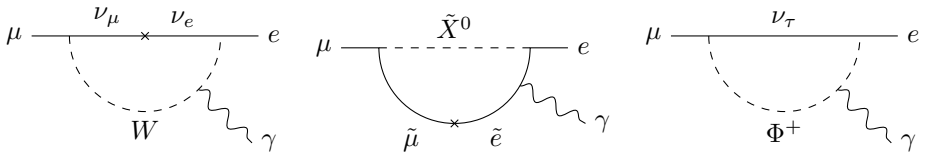

(a) Standard Model (b) Supersymmetry (c) Singly Charged Scalar

Figure 1.2: Different processes for the $\mu \to e\gamma$ decay.

photon. This decay is looked for by the MEG II experiment [2] at PSI. The second potential decay channel is the decay of the anti-muon into two positrons and an electron searched for by the Mu3e experiment [13]. The third option is the conversion of a muon into an electron in the proximity of an atomic nucleus searched by Mu2e [14] and COMET [15].

While the SM on its own with massless neutrinos excludes these decays, the observed neutrino oscillations would allow them albeit highly suppressed by the mass ratio of the neutrino to the W-boson. Models used to explain the observed anomalies would add new particles with additional contributions to these processes. Independent of the model to be used, precise knowledge about the branching ratios of muon cLFV processes is used to confine the potential parameter space.

A selected few processes that could give rise to the $\mu \to e\gamma$ decay are presented in Figure 1.2. The first option is the SM process in combination with neutrino oscillations depicted in Figure 1.2a. As stated above, this channel is highly suppressed.

Another possibility are super-symmetric particles that would mix [16]. One option for this is depicted in Figure 1.2b. Note however that the first predictions of these SUSY models are nowadays already heavily restricted. Thus, a new upper limit on the $BR(\mu \to e\gamma)$ immediately translates to further restrictions on the parameter space of SUSY theories.

A more recent theory that could result in a sizeable branching ratio of the $\mu \to e\gamma$ decay is the introduction of a singly charged singlet scalar [17] as depicted in Figure 1.2c. Although this model aims to offer a different hypothesis in case the B-anomalies persist, the couplings could give rise to the $\mu \to e\gamma$ decay for certain parameter choices. Thus the measurements of the branching ratio already put severe constraints on the parameter space.

Even if one avoids making any kind of assumption on the theory that is supposed to complement and complete the SM, the $BR(\mu \to e\gamma)$ is a crucial quantity. By merely assuming that the SM is an effective field theory approximation of the underlying high energy model, one can define a set of potential operators corresponding to particle couplings, which would result in cLFV [18]. By measuring the $BR(\mu \to e\gamma)$, coefficients for these operators can be constrained [19]. Thus, observing or not observing these decays will restrict a broad variety of current and even future theories not yet thought of.

1.3 A Brief History of the Muon Decay Channel $\mu \to e\gamma$

1.3.1 The Discovery of the Muon

This section deals with the first experimental evidence and investigation of the muon. This includes the discovery and its lifetime measurement.

The first hint of what is known nowadays as a muon was found in the early 1930s when investigating so called "Ultrastrahlung". P. Kunze observed a positive particle track of unknown nature [20]. He only stated that its ionisation neither matches a positive electron nor a proton, yet he didn't elaborate further. The identification of a new particle with a rest mass between the electron and proton happened shortly thereafter in the second half of the 1930s by S. Neddermeyer and C. Anderson. They were measuring energy losses of particles originating in cosmic ray showers when passing either through lead or platinum inside a cloud chamber. Their data acquisition basically consisted of a photo camera, either triggered by Geiger counters or at random. In their articles [21, 22] they claimed that their experiments suggest a charged particle heavier than the electron yet still much lighter than a proton. Further they proposed that these particles are removed by a very effective process as they are not observed elsewhere.

Shortly thereafter, J. Street and E. Stevenson found clear evidence of such a particle [23] with a somewhat more dedicated setup. They were selecting the penetrating type of particles in cosmic ray showers by using a three counter telescope with a lead filter in between. By adding veto counters after their cloud chamber, they could trigger the camera on events originating from penetrating particles near the end of their range. Out of the 1000 photos they took, there was one track that suggested a particle with a rest mass of about 130 times the rest mass of an electron.

The results of a more accurate measurement were published in 1939 by S. Neddermeyer and C. Anderson in [24]. As in the previous measurements, a cloud chamber in a magnetic field was used. A Geiger-Müller counter placed inside the cloud chamber served as trigger for the camera in that specific setup. A photograph taken with this apparatus indicates a muon mass of about 220 ± 35 electron masses.

Nowadays it is known that these particles called muons have a mass of $m_\mu \approx 106\,\mathrm{MeV/c^2}$ and a lifetime of $\tau \approx 2.20\,\mu\mathrm{s}$. They are roughly by a factor of 200 heavier than electrons and almost a factor 10 lighter than the proton, so Street and Stevenson were slightly off the true value, yet their achievement is still remarkable, considering the equipment of their time.

Lifetime measurements of the muon were done in the early 1940's by B. Rossi and N. Nereson[25, 26] amongst others. They used absorbers to stop cosmic muons, called "Mesotrons" (intermediate particles [27]) at that time, which was the only known source back then. With the help of various Geiger counters, referenced only as "counters" as there was nothing else available to turn radiation into an electrical signal, they detected entrance and decay of the muon. Further they used a "time circuit", that generated an electric pulse equal to the delay between entrance and decay signal, and a pen-writer. With these means, they managed to record the "integral disintegration curve", from which they could extract the lifetime $\tau = (2.15 \pm 0.07)\,\mu\mathrm{s}$.

The use of an absorber of various materials to stop cosmic muons in combination with counters is typical for the first era of muon science. The other detection system available at that time were either cameras in combination with cloud chambers or later on photographic emulsions. Some of these experiments are described in more details in the next section.

1.3.2 Detailed Investigation of the Muon Decay

A short overview over the experiments dedicated to the nature of the muon decay is presented here. It concludes with the theoretical modelling of the Michel decay.

Early on, the parallels between the muon decay and the radioactive β-decay were recognised. As at that time it was a common misconception, that only one neutrino was emitted during β decay, a mono-energetic electron was expected at half the muon rest mass.

Consequently, C. Anderson et al.in 1947 concluded wrongly a muon mass, which is roughly by a factor of 100 larger than the electron mass, when interpreting a photograph of a muon decay inside a cloud chamber [28]. To obtain this photograph, the whole experimental apparatus was placed inside a B29 plane and brought to an elevation of 9200 metres.

Out of the whole series, one photograph was interpreted as a positive muon that came to rest inside the cloud chamber and thereafter produced a positron of 24 MeV. Based on the assumption of a two-body decay, a mass between 90 and 110 electron masses was concluded, which is off by a factor of 2. Further, it is annotated, that previous measurements [24] suggested twice the mass obtained from this measurement, yet this discrepancy could be accommodated within the statistical fluctuations.

In a work published by J. Steinberger in 1948 [29] it was shown, that the range spectrum of the decaying electrons differs significantly from what would be expected for mono-energetic particles. For this experiment, four counter trays separated by absorbers were used. He looked for coincidences of the two upper trays, followed by a delayed coincidence in the lower two trays. This corresponds to a muon entering through the upper two trays being stopped between tray 2 and tray 3. The decay product then passes through the lower two trays.

To determine the range of the decay products, the event rate as a function of the absorber thickness between tray 3 and tray 4 was measured. From the results reported in [29], one concluded that the electrons from muon decays are not mono-energetic. Thus the conclusion was, that the muon cannot decay into two particles only. As the obtained spectrum could not be fitted perfectly well with the curve obtained from theoretical calculations, the possibility to explain this behaviour

by two concurring decays was considered as an explanation, their low signal to background ratio for highly penetrating electrons as another.

Not even a year later in 1949, a first energy spectrum distribution for the decay products of the muon was published by R. Leighton et al. [30]. They were using a cloud chamber to determine the energy of the decay particles directly out of the curvature of the electron or positron track observed. Out of the 15 000 photographs taken at a rate of about ten events per hour, they found 75 tracks that allowed for a proper determination of the energy of the decay products.

As they observed clearly a continuous energy spectrum, it was proven that the muon decays at least into three particles. From the endpoint of the spectrum, they concluded that the other two particles have to be neutral and of low mass. Assuming the simplest of all cases, where the muon decays into an electron and two neutrinos, they concluded that the muon is of half-integer spin.

A theoretical description of the muon decay followed shortly after in 1950 by L. Michel in his publication on the interaction of four half-spin particles [31]. He noticed that the observed experimental curve matches perfectly with his theoretical predictions assuming the decay of the muon into an electron and two neutrinos. As a result, the standard muon decay $\mu \to e\nu_\mu\bar{\nu}_e$ was named after him as the "Michel decay".

1.3.3 The Search for $\mu \to e\gamma$ Begins

In this section, a wide list of experiments searching for $\mu \to e\gamma$ is presented. Their setup is described and potential improvements with respect to the previous ones outlined.

The first negative results in the search for the $\mu \to e\gamma$ decay were published in 1948. One of the measurement was performed by E. Hincks and B. Pontecorvo published in [32]. Their experiment consisted of three separate rows of Geiger-Müller counters. Between the second and the third row, a graphite absorber was placed with some lead placed towards the counter rows. A coincidence between the first and the second row marked the entrance of a muon into the graphite absorber. A photon emitted in the muon decay could potentially interact with the lead around the graphite absorber and the subsequent electrons trigger a counter. In such a case, the signal would look as a coincidence of the first and the second row followed by a coincidence in the second and the third row.

The main background for this experiment were events, where a second muon would trigger the coincidence between the second and the third row of counters within the specified time window after the first muon triggering the coincidence between the first and the second row. After the background subtraction, they published the result, that the coincidence rate was $0^{+0.06}_{-0}$ counts per hour. Based on their expectation of about one count per hour, should $\mu \to e\gamma$ be the default muon decay, one can consider their measurement as a first upper limit for the branching ratio of the $\mu \to e\gamma$ decay.

In a similar measurement R. Sard and E. Althaus came to the same conclusion [33]. The basic concepts of their apparatus were identical to the one used by Hincks and Pontecorvo, yet their detection scheme and some materials were different. Instead of graphite, they used brass to stop the cosmic muons. Further, they used five rows of Geiger-Müller counters with the brass absorber to stop the muons between the second and the third row.

Thus a coincidence of the first two in anti-coincidence with the third row indicates the arrival of a muon stopped in the brass absorber. A photon emitted downwards would likely pass through the third row of counters and has some chance to be converted into an electron-positron pair inside a lead layer below the third row. Either of the particles could thereafter trigger a coincidence in the fourth and the fifth row of detectors.

With this setup, they were looking for the delayed emission of a γ photon rather than the $\mu \to e\gamma$ decay, yet still they excluded the emission of γs in most of the cases. They suggest that less than 5 % of the muon decays are accompanied by a high energy photon. This upper limit matches perfectly fine with the previous observation by Hincks and Pontecorvo.

At this point it is noteworthy, that both of their experiments would potentially detect a radiative muon decay $\mu \to e\nu\nu\gamma$ as a $\mu \to e\gamma$ decay. This is due to the simple reason that neither of their experiments was able to perform any kind of energy measurements and the angular resolutions were restricted to say whether a particle was moving upwards or downwards. However, their upper limits of 5 % on the branching ratio for the emission of a high energy photon are not yet sensitive enough

to detect the radiative muon decay whose branching ratio is of the order of 1 %, depending on the energy cut placed on the photon.

With the availability of proton accelerators to produce pion beams, the possibilities in particle physics in general improved drastically. This affected the opportunities to search for $\mu \to e\gamma$ in particular. Instead of waiting for cosmic muons to arrive in the experiment, one could obtain large numbers of pions stopped in a target that would then decay to muons.

To benefit from a good stopping power for the incoming pions and having as few material as possible in the path of the emitted positrons, Parker, Anderson and Rey [34] decided to use a slanted target. This feature is still used in today's MEG II experiment. To detect the emitted γ they relied on conversion in lead. Moreover, they used a combination of scintillators and spark chambers to detect the direction of the charged particles together with carbon plates to estimate the range thereof.

Given the high rate of the pions ($20\,000\,\frac{1}{\mathrm{s}}$) in comparison to the readout speed of the detector, they had to deal with the fact that many of their recorded events were accidental background. While the angular resolution was good enough to serve as cut criterion in the analysis, the range could only be used to reject the low energy positrons but not in the detailed analysis. Based on their likelihood analysis, they claim that the most probable $BR(\mu \to e\gamma) = 0$ and that this probability falls to 10 % of the maximum for a $BR(\mu \to e\gamma) = 2.2 \times 10^{-8}$ [34].

About a decade later, another experiment was performed at SIN by H.P. Povel et al. that benefited from two major steps forward [35]. On the one hand, they could use a muon beam. In combination with advancements in the data acquisition electronics, this allowed to use a higher rate of 5×10^5 muons per second stopped on the slanted target.

On the other hand, they used sodium iodide crystals to detect photons and positrons. This technology allowed to measure the energy deposited by the particles. Later, such a detector will be named calorimeter. While the position of the positron was measured by MultiWire Proportional Chambers (MWPC), the position reconstruction for photons relied on conversion prior to the large sodium iodide crystal.

While the previous experiments had to rely on the timing and the angular distribution to reject background, this experiment now additionally added photon and positron energies. They reported that the observations matched the expectations of the radiative Michel decay $\mu^+ \to e^+\nu\bar{\nu}\gamma$ and published a new upper limit of $BR(\mu \to e\gamma) < 1.1 \times 10^{-9}$ [35].

The trend to more complex experiments continued. The next notable experiment searching for cLFV in muon decays was Crystal Box [36]. It is noteworthy that unlike previously mentioned experiments, this experiment was given a name, that stems from the design of the apparatus. As the name suggests, Crystal Box featured a large number of sodium iodide crystals that formed an outer box around the target and the inner drift chamber as well as scintillator detectors.

It is designed to detect the position of charged particles with the drift chamber. Their time is estimated based on the scintillators and their energies using the outer sodium iodide detectors. To reconstruct photons the information from the sodium iodide crystals forming the outer box is used. Given its large acceptance, this experiment was sensitive to a broader range of cLFV decays such as $\mu \to e\gamma$, $\mu \to eee$ or $\mu \to e\gamma\gamma$.

Although the beam rate was lower with respect to the previous experiment, this experiment improved the stopping rate by using a beam of surface muons with a lower momentum compared to the previous one. Additionally, this experiment features a significantly increased acceptance for potential signal events given the much larger amount of detectors deployed.

Another novelty used for this experiment was the simulation of the detector response. Due to improvements on the available computational power, Monte Carlo simulation of events inside the detector geometry could be performed. Moreover, they described various calibration methods deployed, some of which are still in use in state of the art experiments with appropriate adaptions. Their likelihood analysis suggests a $BR(\mu \to e\gamma) < 4.9 \times 10^{-11}$ at 90 % confidence level [36].

In the next decade, a different approach to measure the energy was deployed. The MEGA experiment [37] was using spectrometers to measure the momentum vector of the positrons and photons. These spectrometers basically consisted of three main ingredients. First, a magnetic field was used to curve the tracks of the charged particles similar to what was used previously in cloud chambers on a different scale. Second, a gaseous detector was used to detect hits along the tracks of the charged particles while having a minimal effect on the tracks. Third, plastic scintillators are used to measure the timing information after sufficient information is gathered about the track.

The MEGA positron spectrometer was formed of a set of eight MWPC. This formed the inner part of the detector around the slanted target. The scintillators for time measurements were placed towards the upstream respectively downstream of the detector in a barrel around an absorber to terminate the positron tracks. Due to the curved tracks, the initial momentum from the muon decay is estimated by propagating the measured positron momentum in the chambers back to the target structure. This makes detailed knowledge about the target position and deformations crucial.

In order to detect photons with a spectrometer, they first have to be converted to an electron positron pair. This is done by the use of some dense material. For MEGA lead foils have been used. This process implies a loss of detection efficiency as the conversion efficiency of a photon to an electron-positron pair is limited. To counteract this, the photon spectrometer consisted of three concentric layers. Each layer consisted of MWPCs and drift chambers to detect the hits along the track and scintillators inside the lead layer such that they are hit only after the charged particles passed through the drift chambers.

This design however has the issue that positrons from the decay that are emitted close to perpendicular to the homogeneous magnetic field keep spiraling there for a comparably long time. Not only will they generate a large signal due to multiple hits inducing cross-talk between channels. They also exhibit a high chance to pile up with further events. Even more so given the fact that the used beam exhibited a macro-structure, i.e. the incoming muons were not homogeneously distributed over time.

The data acquisition period for the physics data spanned over the years 1993 - 1995. They published a new upper limit $BR(\mu \to e\gamma) < 1.2 \times 10^{-11}$ at 90 % confidence level in 2002 [37]. This is by about two orders of magnitude worse than the previously estimated sensitivity of 4×10^{-13}. They attribute this to the fact, that cross-talk in the positron spectrometer degraded the performance thereof and limited the muon stopping rate. Similar effects degraded the performance of the photon spectrometer and an incident with the crane reduced the scintillator efficiency and affected the time resolution between the particles [37].

Benefiting from half a century of $\mu \to e\gamma$ searches and their experiences the MEG experiment was designed [38]. Aiming for a high number of stopped muons while keeping accidental background at a minimum, the choice fell naturally to the PiE5 beamline [39] at PSI providing a continuous surface muon beam. Positron detection works by means of a spectrometer with some significant changes to correct for the shortcomings of the MEGA design. Photons were detected by the means of a calorimeter based on liquid xenon.

The MEG spectrometer consists of drift chambers to detect the positron tracks and thus reconstruct the initial momentum and vertex by propagating the track back to the target plane and a timing counter made of plastic scintillators. These are placed on the upstream and downstream side of the detector.

While MEGA used a uniform magnetic field, MEG was designed to use a dedicated magnet such that the bending radius depended only on the positron momentum but not their angle of emission relative to the target. Thus it is referred to as COnstant Bending RAdius (COBRA) magnet. This offers the additional benefit that positrons emitted almost perpendicular to the beam axis will experience a Lorentz-force that accelerates them along the beam axis and thus removes them from the spectrometer in an efficient manner.

The liquid XEnon Calorimeter (XEC) consisted of one large volume containing up to 900 l of liquefied cryogenic xenon. This yields a single large sensitive volume. PhotoMultiplier Tubes (PMTs) were placed on all surfaces of the vessel to collect the scintillation light to determine the deposited energy and the position of the conversion. Due to the faster light emission in xenon compared to the previously used sodium iodide, the xenon based calorimeter was able to simultaneously provide a high precision in energy and time. This was a huge improvement with respect to previous experiments.

The MEG experiment completed data acquisition in 2013 after several years and published in 2016 the final result $BR(\mu \to e\gamma) < 4.2 \times 10^{-13}$ at 90 % C.L. [40]. The original sensitivity goal [41] was missed by an order of magnitude as the positron track matching efficiency between drift chambers and timing counter was by a factor two worse and the detector performance was worse than assumed in the design phase. This is reported in more detail in [38].

In addition to the $\mu \to e\gamma$ search, events where two photons were detected have been analysed and a search for the decay $\mu \to eX, X \to \gamma\gamma$ with a yet unknown particle X was performed. Upper limits in dependence of the mass of the X particle were published in 2020 [42].

Chapter 2

The Search for Exotic Physics with the MEG II Experiment

While the MEG II experiment is designed to search for the $\mu \to e\gamma$ decay, its capabilities reach beyond this single process. Using the highly performing detectors of the MEG II apparatus, additional signatures originating from exotic particles may be observed. Two candidates are briefly discussed in this chapter.

2.1 Majoron Search

Multiple theories predict low energy particles (X) that could be candidates for the decay $\mu \to eX$. A brief listing of candidates is mentioned in the theoretical introduction. Further, the current state of research and how MEG II can contribute will be discussed.

2.1.1 Theoretical Introduction

Assuming any particle candidate X with a mass $m_X < m_\mu$ that could result from the decay $\mu \to eX$, its lack of detection so far makes it obvious, that this branching ratio is bound to be comparably low with respect to the default Michel decay of the muon. The signature to detect is an at leading order monochromatic peak on top of the Michel positron spectrum. Radiative corrections at Next to Leading Order (NLO) may broaden the peak.

As the name of the section suggests, one potential candidate is the Majoron. This particle was introduced as Goldstone boson arising from spontaneous global symmetry breaking of the lepton number yielding majorana mass terms for neutrinos [43, 44, 45]. Further candidates are axions and axion like particles [46, 47, 48, 49, 50, 51], familons [52, 53, 54, 55], flavons [56, 57], the flaxion [58] or the hierarchion [59].

Although these candidates commonly arise from spontaneous symmetry breaking resulting in a neutral boson with low mass, their origins differ and so do their couplings. Thus, searching independently of the model for a monoenergetic signature in the Michel background is a good approach to detect such a new particle or to place new constraints on the $BR(\mu \to eX)$. Thus, such a search is limiting the parameter space for current and future theories.

2.1.2 Current State of Research

The current limits on branching ratios that result in monoenergetic positron signals are set by two different experiments, depending on the assumed mass m_X of the boson and its coupling. For masses in the range from $13\,\mathrm{MeV/c^2}$ to $80\,\mathrm{MeV/c^2}$ the upper limits are provided by the TWIST collaboration [60]. For masses below $13\,\mathrm{MeV/c^2}$, the older results by Jodidio et al. [61] are currently the best available upper limits for certain couplings.

This separation is easily explained by the design of the corresponding experiments. The experiment by Jodidio et al. was explicitly considering positrons emitted backwards with respect to the anti-muon spin [61]. For positrons emitted towards the kinematic endpoint of the Michel spectrum,

this direction is suppressed by the parity violating nature of the weak interaction. Thus, they had a clearly reduced background, yet required that the decay $\mu \to eX$ does not exhibit the same parity violating behaviour as the Michel decay. They published the upper limit $BR(\mu \to ef) < 2.6 \times 10^{-6}$ where they denote the familon by f [61], for which an isotropic emission is assumed.

On the other hand, the TWIST detector [62] follows a different geometry. The sensitive volume is placed perpendicular to the beam axis and is thus collecting more positrons from the ordinary Michel decay $\mu \to e\nu\nu$. Furthermore, their experiment was designed to perform a precision measurement of the Michel decay spectrum and thus enabled to accept lower positron energies. This allows to set limits on the $BR(\mu \to eX)$ for a wide range of m_X.

In addition, the large angular acceptance of the detector allows the analysis of different models for anisotropic emission of positrons. They can thus provide a meaningful result even under the assumption that the $\mu \to eX$ decay follows the same parity violating pattern as the ordinary Michel decay. They obtain upper limits for $BR(\mu \to eX)$ depending on the mass and coupling model of the order of $\mathcal{O}(10^{-5})$ for $13\,\mathrm{MeV/c^2} < m_X < 80\,\mathrm{MeV/c^2}$ and values that go up to 5.8×10^{-5} for $m_X < 13\,\mathrm{MeV/c^2}$ [60].

2.1.3 Majoron Search with the MEG II Apparatus

The MEG II experiment provides an excellent spectrometer to measure the energy spectrum of positrons emitted from muon decays. In addition large amounts of positron data will be recorded when the MEG II reaches the intended sensitivity for the $\mu \to e\gamma$ decay. From this data a subset can be selected to search for the decay $\mu \to eX$. In addition, once can consider the option of a dedicated run to search for $\mu \to eX$ using the dedicated Michel trigger.

The MEG II spectrometer was designed to detect $\mu \to e\gamma$ events, which results in good angular acceptance while the momentum acceptance is limited to high energy positrons to reduce pileup from low energy positrons. The trigger efficiency for positrons below 45 MeV worsens drastically and is almost negligible once the positron energy drops below 40 MeV. This reduces the sensitivity to the $\mu \to eX$ decay channel for larger masses m_X of the Majoron or other candidates.

The theoretical prediction on the probability density function for the Michel decay changes rapidly close to the kinematic endpoint around 52.8 MeV. In a situation where the absolute energy scale of the experiment is affected by some unknown systematic offset, this will degrade the sensitivity to the $BR(\mu \to eX)$ for low masses m_X of the unknown particle.

As stated above, the signature of the decay $\mu \to eX$ is a monoenergetic positron peak. This is due to the fact that any of the above mentioned X candidates is interacting very weakly with matter and thus will escape detection unless very short-lived and decaying into SM particles (i.e. $X \to ee$ or $X \to \gamma\gamma$).

The most prominent background is the ordinary Michel decay $\mu \to e\nu\nu$. This makes detailed theoretical knowledge about this decay mandatory to perform a search like this. Predictions and tools to do so are available up to the NNLO [63, 64, 65] with more precise calculations on their way [66].

Thus, the search for the Majoron or any other boson that may act as candidate in the decay $\mu \to eX$ is an excellent addition to the main physics goal to push the sensitivity for the $BR(\mu \to e\gamma)$ down by another order of magnitude. No dedicated adjustments to the apparatus or data acquisition are required. However, detailed theoretical models need to be included in the simulation code and the experimental systematics well understood.

2.2 Fifth Force Search

This section offers a brief overview over the beryllium anomaly, which was observed by A. J. Krasznahorkay et al. [3]. Their experimental observation could either be interpreted as particle or a combination of detector geometry and higher order contributions to the process within the SM. A second, independent measurement with the MEG II apparatus is set to provide clarity.

2.2.1 Current State of Research

The first indication of a potential new particle that is referred to as X-Boson was published by A. J. Krasznahorkay in [3]. They were investigating transitions from excited ^{8}Be states to the ground

state under the emission of an electron-positron pair and observed a deviation from the theoretical predictions of that time. In more detail, they populated the 17.6 MeV and the 18.15 MeV excited states by the use of the nuclear reaction

$$^{7}\mathrm{Li} + p \rightarrow {}^{8}\mathrm{Be}^{*} \tag{2.1}$$

where the inbound proton beam is tuned to the $E_p = 441\,\mathrm{keV}$ respectively to the $E_p = 1.03\,\mathrm{MeV}$ resonance.

By default, these excited $^{8}\mathrm{Be}^{*}$ states decay to the ground state by the emission of a photon.

$$^{8}\mathrm{Be}^{*} \rightarrow {}^{8}\mathrm{Be} + \gamma \tag{2.2}$$

However, there is a certain chance that an electron-positron pair is emitted instead of the photon.

$$^{8}\mathrm{Be}^{*} \rightarrow {}^{8}\mathrm{Be} + ee \tag{2.3}$$

Later decay was investigated by A. J. Krasznahorkay and his colleagues. The SM explains it by the conversion of a virtual photon and this process is referred to as internal pair conversion (IPC).

In the description of their detector [67], they give an energy resolution of about 10 % at 1.8 MeV and an angular resolution of below 10°. MWPCs were used to detect the position of the emitted electron-positron pairs and five $\Delta E - E$ detector telescopes to measure energies and assert coincidences.

They report [3] the observation of an anomaly in the isoscalar magnetic dipole transition from the excited 18.15 MeV state to the ground state of ^{8}Be. In more detail, the distribution of the angle between the emitted electron and the emitted positron was investigated. An excess with respect to the theoretical IPC prediction of that time was observed above 130°.

No such anomaly could be observed for the transition from the 17.6 MeV excited state to the ground state. It is suggested in the same publication, that this anomaly could be best explained by a boson with a mass of $16.70 \pm 0.35(\mathrm{stat}) \pm 0.50(\mathrm{syst})\,\mathrm{MeV/c^2}$ and a branching ratio of about 5.8×10^{-6} with respect to the deexcitation of the 18.15 MeV state through emission of a γ.

Initially, there was some major doubt about this finding due to the outdated theoretical model. Although no nuclear effect was known to cause this anomaly, the models were not precise enough to exclude the existence of such an anomaly.

The same group published new evidence for the existence of this hypothetical particle in 2019 [68].They report the observation of a similar anomaly in ^{4}He. When observing the transition from the 21.01 MeV state of ^{4}He, they observed an excess with a 7.2σ significance. They explain their observation by assuming a particle with a rest mass of $16.84 \pm 0.16(\mathrm{stat}) \pm 0.20(\mathrm{syst})\,\mathrm{MeV/c^2}$, which could be the same particle used to explain the anomaly in beryllium.

2.2.2 Theoretical Explanation

A first attempt to explain this anomaly within the known physical theories was performed by X. Zhang and G. A. Miller [69]. They noticed that the nuclear model used in the analysis was missing some additional corrections. They provide an advanced model that reduces the significance of the observed beryllium anomaly by at least one standard deviation. Moreover, they manage to explain the anomaly by adding a form factor. This however does not seem plausible as such a form factor would have shown up in previous measurements.

Just recently in 2021, A. Aleksejevs and his colleagues published NLO QED calculations for the transition from the excited 18.15 Mev state of ^{8}Be to the ground state [70]. With these corrections, they managed to describe the shape of the observed anomaly using non-resonant SM processes in combination with the detector configuration used by Krasznahorkay et al. and thus could explain the observed anomaly without the need for exotic physics beyond the SM. Yet, the paper does not provide information if the anomaly observed in helium can be explained in a similar way.

2.2.3 Fifth Force Search with the MEG II Apparatus

As all experimental measurements of the anomaly were performed by the same group with the same detector technology at the same laboratory, an independent measurement using a different experimental setup is needed. The MEG II experiment offers ideal conditions for this cross check.

Assuming the higher order theoretical corrections by Aleksejevs and his colleagues [70] in combination with the detector setup used by Krasznahorkay and his group are the true explanation for the observed anomaly, the anomaly should take a different shape due to the fact the MEG II experiment deployed a clearly different detector configuration. The detailed studies were not yet finished by the time this thesis was completed.

Moreover, the MEG II apparatus is designed for an outstanding positron momentum reconstruction. Being able to measure the momentum of the involved electron and the positron as well as their relative angle, the invariant mass spectrum can be investigated with the MEG II apparatus. This enhances the ability to discriminate between the hypothesis of the higher SM corrections using non-resonant processes and the resonant new exotic physics hypothesis with the new X-Boson.

With respect to the measurement, the Cockcroft-Walton proton accelerator used for calibrations of the xenon calorimeter is available and can be used for this purpose. The beam energy needs some adjustment to excite the 18.15 MeV resonance in beryllium rather than the 17.6 MeV resonance used for the XEC calibration.

Moreover, the spectrometer of the MEG II experiment is designed for the reconstruction of 53 MeV positrons. One must however consider, that the electrons and positrons of interest have a lower energy than the usual MEG II signal positron. Thus an adaptation of the magnetic field is required for the X-Boson measurement. The reduced field was already mapped by collaborators and found to scale reasonably well. Moreover, a minor adjustment of the analysis code is needed for an appropriate reconstruction of electron-positron pairs emitted.

Additionally, the lithium borate target used for calibration purposes does not match the geometric requirements for the planned measurement. A new target is thus designed with a thin layer of lithium oxide placed on a thin substrate layer. Moreover the material budget is much lower for the electron-positron pair with respect to the γ photons used in the XEC calibration. Thus, a dedicated target structure needs to be developed to confirm or refute the claim of the newly discovered $X(16.7)$ boson.

Chapter 3

The MEG II Experiment

This chapter offers a summary of the MEG II experiment. It discusses its sensitivity, signal and background as well as the detector construction.

The ultimate goal of the MEG II experiment is to find the branching ratio BR of the cLFV decay

$$\mu \longrightarrow e + \gamma$$

or to set a new upper limit to it. The current upper limit $BR(\mu \to e\gamma) < 4.2 \times 10^{-13}$ at 90 % Confidence Level (C.L.) is set by the preceding MEG experiment [1]. The MEG II experiment will be more sensitive by approximately an order of magnitude. It is estimated that MEG II reaches a sensitivity down to a branching ratio of 6×10^{-14} within three years of data taking in the upcoming years[2, 71].

For this purpose, an anti-muon beam is stopped in such a way that the anti-muons decay at rest in the laboratory frame. This will lead to an emission of a positron and a gamma, each carrying half of the energy (52.8 MeV) in a back-to-back geometry in the lab frame [1]. Anti-muons are favoured because they do not get trapped by the atomic nucleus. Muons can enter specific orbitals around the nucleus, thus leading to an additional uncertainty in the total energy prior to the decay. In the worst case, muons can even get absorbed by the nucleus [72].

3.1 Event Signature and Backgrounds

This section shortly describes the properties of the $\mu \to e\gamma$ signal as well as the irreducible background from radiative Michel decay $\mu^+ \to e^+\bar{\nu}_\mu\nu_e\gamma$ and the accidental background of multiple events that fake a signal.

The $\mu \to e\gamma$ decay is a two body decay. This implies that in the centre of mass frame, the signature is bound to be a back to back geometry where each particle carries exactly half the muon's rest energy. Moreover, as both particles originate from the same decay, they are in coincidence.

$$E_e^* = E_\gamma^* = \frac{1}{2} m_\mu = 52.8\,\text{MeV} \tag{3.1}$$

$$\Theta_{e\gamma}^* = 180° \tag{3.2}$$

$$\Delta t_{e\gamma}^* = 0\,\text{ns} \tag{3.3}$$

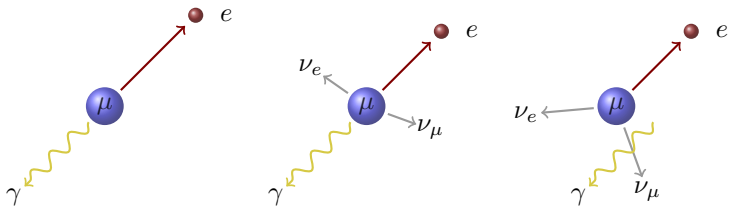

(a) Signal (b) Background (c) Background

Figure 3.1: Signal Events and Backgrounds

In the equations above, the energies E^* of the respective decay particles are given in the centre of mass frame as well as the angle $\Theta^*_{e\gamma}$ between the positron and the photon and the time difference $\Delta t^*_{e\gamma}$ between the emission of the particles.

By stopping the muons in the centre of the experiment, the laboratory frame and the centre of mass frame coincide. Consequently these conditions apply to the particle energies E_e, E_γ, their relative angle $\Theta_{e\gamma}$ and the time difference $\Delta t_{e\gamma}$ between their emission

$$E_e = E_\gamma = \frac{1}{2} m_\mu = 52.8\,\text{MeV} \tag{3.4}$$

$$\Theta_{e\gamma} = 180^\circ \tag{3.5}$$

$$\Delta t_{e\gamma} = 0\,\text{ns}. \tag{3.6}$$

The expected signal event is depicted in Figure 3.1a. This signal signature gives rise to two main backgrounds, the irreducible background depicted in Figure 3.1b and the accidental background depicted in Figure 3.1c.

The irreducible background stems from so called radiative muon decay or RMD for short. This refers to the muon decay, where a positron, two neutrinos and a photon are produced.

$$\mu^+ \longrightarrow e^+ \gamma \nu_e \bar{\nu}_\mu \tag{3.7}$$

The two neutrinos produced are so weakly interacting, that they are invisible to any reasonable detector dedicated for the $\mu \to e\gamma$ search.

If the undetectable neutrinos carry a vanishing amount of energy, it may appear that the decay particles' energies $E_\gamma \approx E_e \approx \frac{1}{2} m_\mu$ sum up to the total muon mass within the uncertainties as well as the needed back to back geometry of the signal signature. As this background stems from the decay of a single particle, the positron and the photon are a priori coinciding in time.

Although excellent resolutions in terms of position and energies can improve the situation, this kind of background cannot be suppressed and it scales with the muon beam rate as do the signal events. This background has to be countered with solid theory predictions in the end [73].

The accidental background is a collection of events that fake the signature of a signal event. Typically it consists of a Michel decay with the positron at its kinematic endpoint at 52.8 MeV that overlaps with a photon from any other source, such as a second muon decaying via a RMD with the photon carrying half the muon rest energy. Alternatively, such a photon may originate from an annihilation in flight of a positron with an electron.

If the positron and the photon from these two totally uncorrelated events pass close enough on the target in almost a back to back geometry, they can easily be mistaken for an actual signal event. Due to their nature to include two different decays, an intelligent detector design in combination with excellent detector performance can remedy the situation and reject these background events to a certain extent.

While the detector design and some reasoning behind is presented in the next section, it is noteworthy that both signal and irreducible background originate from the decay of a single muon. The corresponding rates are thus expected to be proportional to the beam rate R_μ, the corresponding branching ratios, the detector acceptance and the detection and selection efficiencies. The accidental background on the other hand includes at least two different muons decaying. For the accidental background rate R_{acc} it is predicted by integrating the appropriate probability density functions that

$$R_{\text{acc}} \propto R_\mu^2 \times \Delta E_\gamma^2 \times \Delta p_e \times \Delta \Theta_{e\gamma}^2 \times \Delta t_{e\gamma} \tag{3.8}$$

where ΔE_γ refers to the photon energy resolution, Δp_e to the positron momentum resolution, $\Delta \Theta_{e\gamma}$ to the resolution in the relative angle between positron and photon and $\Delta t_{e\gamma}$ the resolution on the time difference between the emission of the two particles [2]. It is crucial to be aware of the fact, that this rate is modified by the geometrical acceptance of the detector, as well as detection and rejection efficiencies. Some special measures to get a good rejection efficiency are discussed in the next section.

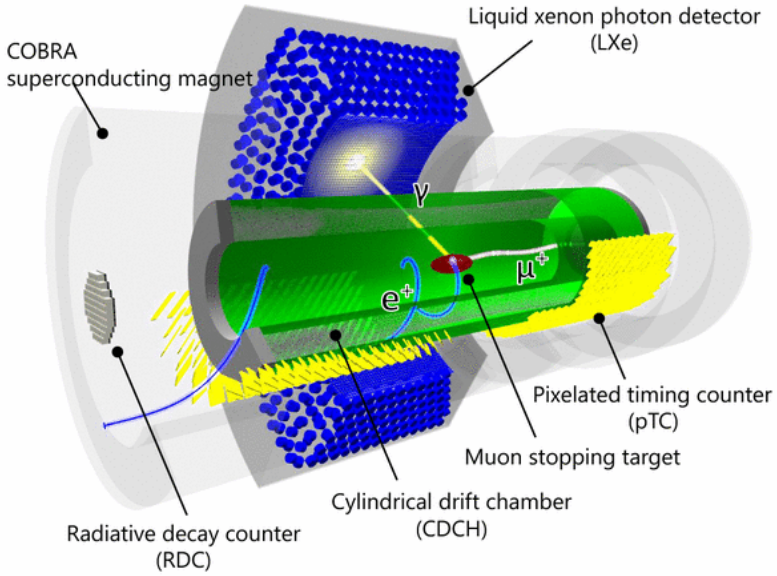

Figure 3.2: Schematic design of the MEG II experiment. Taken from [2].

3.2 Setup of the MEG II Apparatus

This section describes the apparatus of the MEG II experiment in some more detail. The important subsystems are described in dedicated subsections. Moreover, some of the calibration methods necessary for the understanding of this thesis are described. For more details, please refer to the dedicated publication [2].

The purpose of the MEG II apparatus is to stop the beam muons and to detect the signature of a $\mu \to e\gamma$ event while rejecting the backgrounds as efficiently as possible. To detect the signature of the $\mu \to e\gamma$ decay, a 52.8 MeV photon and a 52.8 MeV positron have to be registered in a back-to-back geometry at the same time.

As the MEG II apparatus is an upgraded version of the MEG apparatus, their basic design is very similar and multiple parts are recycled. The schematic design published in [2] is shown in Figure 3.2. The shortcomings of the MEG apparatus were analysed, substantial upgrades implemented and improved equipment installed. Roughly speaking, the goal of the upgrade was to improve each aspect of the apparatus by a factor of two.

As in previous experiments, the muons are stopped in the centre of the experiment on a dedicated slanted stopping target, which is placed inside a magnetic field. It is arranged in such a way that the emitted positrons curve through the spectrometer, that consists of the cylindrical drift chamber (CDCH) and the pixelated timing counter (pTC) placed inside the superconducting solenoid.

Just outside of the superconducting solenoid, the calorimeter for photon detection is located. It consists of a C-shaped volume filled with liquid xenon. While the CDCH surrounds the target in almost all directions, the xenon calorimeter (XEC) just covers a small fraction of the solid angle. The pTC is placed in such a way, that a positron from a $\mu \to e\gamma$ event should hit it, if the photon hits the XEC.

The magnetic field needed is provided by the COBRA-magnet. COBRA stands for COnstant Bending RAdius, referring to the special gradient field resulting in a bending radius that only depends on the energy of the emitted positron and not its emission angle - at least not in the angular range of interest for the $\mu \to e\gamma$ search. The magnet itself consists of an inner superconducting solenoid and an outer compensation coil.

3.2.1 Beam

The MEG II experiment uses the PiE5 beamline at PSI [39]. It is able to provide one of the most intense, continuous muon beams worldwide. For the MEG II experiment, surface muons at

a momentum of 28 MeV/c are chosen. By adjusting the tuning of the beamline, one can select to transmit either positrons or pions as well.

Notable elements of the beamline are a set of slits, a separator and a dedicated Beam Transport Solenoid (BTS). The slits can be set remotely and are used to adjust the beam rate for the MEG II experiment. The separator works based on electric and magnetic fields and is used to select between muons and positrons. In normal operation, it is used to suppress the positron contamination in the beam reaching the experiment.

The superconducting BTS is the final element of the beamline directly connecting to the experiment. It is crucial to transport the muon beam into the experiment and obtain the desired distribution on the target. The use of a superconducting magnet over an ordinary quadrupole triplet was selected as the iron core of an ordinary magnet would badly interfere with the COBRA magnetic field.

Although the exact rate varies and depends on the beam current delivered by the main proton accelerator, the whole beamline is able to deliver around 10^8 μ^+/s. For the operation of the MEG II experiment, the slits are adjusted in such a way, that the number of stopped muons is 7×10^7 μ^+/s.

3.2.2 Target

The main purpose of the target is to stop the incoming muons in the centre of the detector. As in previous experiments, the target is tilted with respect to the beam axis to provide maximum muon stopping power while having a minimal impact on the muon decay products.

Currently, a target made of polyvinyltoluene is in use. It has a thickness of 130 µm and measures 260 mm×70 mm without frame [2]. This material has additional scintillating properties. Thus, the incoming beam can be monitored via mirror and CCD-camera during the data acquisition without disturbing the experiment itself.

High mechanical stability and precise measurements of the position are crucial for the target, since the curved tracks as reconstructed from the measurements are propagated back to the target plane to estimate the vertex where the muon decayed. Moreover, the target has a measurement and a parking position inside the experiment. The measurement position is at the centre of the experiment and highly reproducible as it is used for most of the data taking. The parking position is slightly upstream and off-axis. The main target is moved there if an alternative target for calibration measurements is used.

3.2.3 Liquid Xenon Calorimeter

To detect the emitted photons, a C-shaped tank filled with liquid xenon is used as calorimeter. The inner surface of the xenon calorimeter (XEC) is covered with silicon photomultipliers (SiPMs). Photomultiplier tubes (PMTs) are placed on the other surfaces of the xenon volume. Installing the SiPMs on the inner surface was one of the main efforts of the MEG II upgrade. As described in the upgrade proposal [71], this was done to improve the homogeneity of the light detection for shallow events and thus improving the overall performance.

The use of a single large volume filled with a liquid scintillator is preferred over a segmented approach using solid scintillating crystals, as energy deposits in dead material between crystals is avoided and the scintillation light is distributed over more photon sensors, eventually allowing for improved reconstruction of the position of the first conversion. Simulations presented in [2] suggest a photon energy resolution of about 1 %, a time resolution of about 50 ps to 70 ps and a position resolution of a few millimetres for photons of the signal energy.

3.2.4 Cylindric Drift Chamber

The cylindric drift chamber (CDCH) is used to reconstruct the track of the positrons. It consists of an almost 2 m long cylinder filled with a gas mixture of 90 % helium due to its radiation length and 10 % isobutane as quencher. During preengineering runs, this gas mixture was slightly changed and tiny amounts of isopropyl alcohol and oxygen added. This was done to enhance the electric stability of the CDCH and was required to operate at the designed working point [74].

The drift chamber uses gold coated tungsten sense wires and silver coated aluminium field wires. Additionally, there are guard wires to ensure the desired field on the innermost and outermost layer. In total, there are a bit more than 12 000 wires. Due to corrosion in the presence of humidity, some

of the 40 µm field wires were damaged critically, resulting in broken wires which had to be removed. Similar effects were observed for the 50 µm guard wires, although at a much lower rate. More details are found in [75].

The wires are arranged in drift cells with an approximately square shape and a width of 6.6 mm for the innermost to 9 mm for the outermost cells. They are arranged in a criss-crossing pattern to enhance the resolution. First estimates predict a Gaussian resolution of $\sigma_r = 110\,\mu\text{m}$ in radial direction perpendicular to the beamline and $\sigma_z = 1\,\text{mm}$ in the axial direction for the hit position[2].

A charged particle passing through a drift cell will lead to an ionisation cluster. This is used to reconstruct the passing of a particle referred to as a hit. Based on the reconstructed hits, the positron track is fitted. From the fit, the positron momentum along the track is estimated and eventually propagated back to the target structure. Based on this propagation, the position of the muon decay vertex is calculated as well as the initial positron momentum vector at the vertex position. Simulations suggest a positron energy resolution of 130 keV, and an angular resolution of a few mrad. The vertex position resolution should be of the order of 1 mm. More detailed numbers are given in [2].

3.2.5 Pixelated Timing Counter

The pixelated timing counter (pTC) is the second part of the MEG II spectrometer. Its primary purpose is a precise measurement of the time of the detected positrons. This is necessary as the CDCH does an excellent job in vertex and momentum reconstruction yet is comparably slow and does not match the time resolution requirements to identify a time coincidence of a photon-positron pair.

The pTC consists of two main parts, referred to as the upstream (US) pTC and the downstream (DS) pTC. Each of them is made of 256 tiles made of plastic scintillators coupled to SiPMs. Although they only cover a small fraction of the solid angle, they are placed such that a positron from a $\mu \to e\gamma$ decay will pass through the pTC if the photon of that decay is emitted in the XEC acceptance. The tiles are arranged such that a signal positron track passes close to perpendicular to each tile.

For a single tile, the timing resolution of a positron hit is estimated to be around 70 ps to 90 ps. Proper positron tracks at signal energy will however pass multiple tiles of the pTC. Thus pTC clusters are formed. The time resolution of reasonably large clusters is clearly improved and below 40 ps.

3.2.6 Auxiliary Detectors

3.2.6.1 Radiative Decay Counter

The radiative decay counter is mounted at the downstream end of the experiment. It consists of LYSO crystals and plastic scintillating plates. It's purpose is to detect positrons that are too low in energy to enter the drift chamber. They potentially emerge from the process $\mu \to e\bar{\nu}\nu\gamma$ and are thus a tell-tale sign if they appear in time coincidence with a high energy photon in the XEC. Thus this detector is used as a veto to reduce the accidental background.

3.2.6.2 BGO Auxiliary Detector

As the name suggests, this auxiliary detector uses BGO crystals coupled to photomultipliers. Its purpose is the detection of high energy photons as part of the charge exchange (CEX) calibration. The detector is designed movable such that it can be placed opposite to any part of the XEC and be used as trigger for back-to-back events of the CEX calibration described below.

3.2.6.3 Cosmic Ray Counter

Cosmic rays are used for calibration purposes of the CDCH. In order to trigger on such an event, a dedicated cosmic ray counter (CRC) has been installed. For this purpose, some scintillator bars of the old MEG timing counter were recycled. Four of these were installed on top of COBRA and another four below. They are arranged in such a way that a muon passing through the upper and the lower CRC will pass through the CDCH.

3.2.7 Calibration Methods

For the MEG II experiment a wide set of calibration methods are deployed. They range from light sources to radioactive sources over nuclear reactions up to low energy particle physics processes. For listing of all potential methods, please consider the appropriate tables in [2] and [38] for the description of most methods in the context of the previous MEG experiment. Here, only a selected few methods are presented as required for the context of this thesis.

3.2.7.1 The Double Turn Method

For the best possible result of the data gained, the exact resolutions in the positron momentum as well as polar and azimuthal angle of the positron have to be known. The ordinary calibration method based on Mott scattered positrons may yield quasi monochromatic positrons, yet their momentum still exhibits variations due to the momentum spread of the incoming positron beam as well as its divergence.

An elegant solution to circumvent these restrictions is selecting a positron track that passes the drift chamber at least twice. Knowing that both partial tracks in the drift chamber are created by the same particle, one should obtain the same momentum and direction by analysing them individually. The difference between the two values may either be explained by the extra material passed between the turns or in statistical uncertainties in the reconstruction and analysis process.

Due to the low material budget of the drift chamber, a collision with a significant amount of matter is rare. It may occur by a second pass through the target structure, a collision with a drift chamber wire or, if the track leaves the drift chamber to the outside, a hit on the timing counter structure. The fine tuned merging algorithm however rejects the merging of tracks in the case of an excessive energy or direction mismatch.

This implies that for any two partial tracks that pass the merging criteria, the underlying positron's momentum and emission angle is equal to a rather high precision. Thus, it is safe to assume that the true values are equal for both parts. The deviations of the two reconstructed variables thus can be presumed to origin from reconstruction uncertainties of the detector.

These differences obtained from individual tracks by Mott scattered positrons of 53 MeV are computed and their overall distribution considered. These distributions contain vital information about the intrinsic resolution achievable by the drift for positrons in the signal region.

Due to the updated geometry of the pixelated timing counter, a similar approach can be used to extract the intrinsic time resolution of the spectrometer. This is referred to as the double cluster method and discussed later in more detail.

3.2.7.2 The Charge Exchange Calibration

To determine the absolute energy scale of the liquid xenon calorimeter in the interesting energy regime around 52.8 MeV a γ source in this very regime is required. Such a source is offered by the charge exchange (CEX) reaction of negative pions on hydrogen and the subsequent decay of the boosted neutral pion into two photons.

Practically, the default MEG II target is replaced by a dedicated liquid hydrogen target. The π^- beam is stopped therein and the reaction

$$\pi^- + p \longrightarrow \pi^0 + n$$

takes place. After this reaction, the π^0 is boosted with respect to the laboratory frame and moves with a momentum of 28 MeV with respect to the detector, corresponding to 20 % of the speed of light.

The neutral pion π^0 is short-lived and decays predominantly into two photons

$$\pi^0 \longrightarrow \gamma\gamma.$$

By going through the simple math, one finds that the extremal energies of the photons are given

by

$$E_\gamma^{\max} = \frac{m_{\pi^0}}{2}\sqrt{\frac{1+\beta}{1-\beta}} = 82.9\,\mathrm{MeV} \tag{3.9}$$

$$E_\gamma^{\min} = \frac{m_{\pi^0}}{2}\sqrt{\frac{1-\beta}{1+\beta}} = 54.9\,\mathrm{MeV} \tag{3.10}$$

where $\beta = 0.2$ represents the speed of the initial π^0 as fraction of the speed of light.

The extremal energies are observed if one photon is emitted in forward direction while the other is emitted in backwards direction with respect to the π^0 movement. Such an event is characterised by a back to back geometry event in the laboratory frame.

As a result, the photon energy is known to either be 54.9 MeV or 82.9 MeV if a back to back geometry is observed. Such a geometry can be enforced by a dedicated experimental modification by a lead collimator in front of the LXe calorimeter and an auxiliary detector directly on the opposite side of the target. By requiring a coincidence in both detectors, two clearly distinct lines for 54.9 MeV and 82.9 MeV are obtained that can be used to define the energy scale of the calorimeter as well as to estimate the achievable photon energy resolution in the signal energy range.

For this purpose solely, any kind of calorimeter that is able to detect an inbound γ will suffice to assert the back to back geometry. As such, it provides an excellent opportunity to test out new technologies as auxiliary detector and determine their potential for future experiments in the cLFV sector.

3.2.7.3 Proton Beam based Calibrations

While in usual operation mode, the muon beam arrives from the upstream side to the experiment, there is the possibility to stop this operation and move the muon stopping target to the parking position. Thereafter, a dedicated proton beam line ending in a dedicated lithium borate target can be inserted from the downstream side. A low energy proton beam from a dedicated Cockcroft-Walton (CW) accelerator can then be shot at the target.

Depending on the energy of the proton beam, different resonances can be triggered. At lower accelerating voltages of 500 kV, the reaction $^7\mathrm{Li}(p,\gamma)^8\mathrm{Be}$ is predominant, which emits high energy photons in the deexcitation process of the 17.6 MeV resonance of beryllium. These photons are then used to ascertain the stability of the XEC energy scale, monitoring its purity and uniformity.

Alternatively, by tuning the proton beam energy at 900 keV one can excite the transition $^{11}\mathrm{B}(p,\gamma\gamma)^{12}\mathrm{C}$ which produces two photons at 4.4 MeV and 11.6 MeV respectively. For the purpose of the calibration, these are coinciding in time and thus are used to calibrate the time offset between pTC and XEC.

Please note that this dedicated CW accelerator is operated mostly independent of the main proton accelerator and the secondary beam lines of PSI. While it is connected to the main person safety elements for obvious reasons, this accelerator can be operated when the main accelerator is switched off and the assembly of this proton beam line is within the MEG II collaborators responsibility. Thus this beam line can be modified to accommodate the $X(17.6\,\mathrm{MeV})$-boson search if deemed non-interfering with the main MEG II goals.

3.2.8 Data Acquisition

As part of the MEG II upgrade, the number of channels for the subdetectors increased by more than a factor of two. The most notable increase in terms of absolute numbers stems from the replacement of the comparably large PMTs by much smaller SiPMs on the XEC inner surface. Apart from the additional channels associated with the improved subdetectors, further channels are required for newly added detectors such as the RDC.

This increased number of channels comes along with additional electronics and an increased amount of data to be digitised and handled. Simply extending the previous MEG data acquisition concept to MEG II was not an option for lack of space at the experimental area. Furthermore, the increase of the beam rate implies an increased trigger rate which the MEG concept could not sustain.

For these reasons, a new system was developed [76]. Its main component is the newly developed WaveDREAM board (WDB). Each WDB offers 16 readout channels, digitises the waveforms and is able to perform low-level trigger tasks. A programmable high-voltage supply can be mounted piggy-back. This enables the WDB to provide the individual bias voltage for each connected SiPM individually.

Up to 16 WDB can be placed in a custom crate. They are complemented by a trigger concentrator board (TCB) for real-time data analysis and a data concentrator board (DCB) which is used for remote operating the WDBs and eventually getting the recorded data written to disks. Thus one such a crate offers a flexible and programmable trigger and data acquisition (TDAQ) system.

For the MEG II experiment, numerous crates are combined by arranging the TCBs in a tree structure. For this purpose, extra TCBs are placed in a dedicated trigger crate. Moreover, ancillary boards were designed to distribute reference clock and control signals to the individual TDAQ crates. Finally, the DCB of each crate is directly connected to the back end computer via ethernet. More details can be found in [76].

Part II

The MEG II Experiment

Chapter 4

Detector Hut Temperature Control

4.1 Introduction

A short note to why the temperature in the detector hut needs to be controlled with a PID controller.

The temperature inside the MEG II detector hut environment is highly affected by various parameters. On the one hand there are daily and seasonal fluctuations in the temperature of the main experimental hall that pass on to the detector hut. On the other hand, there are various sources of heat inside the detector hut, ranging from the electronics to the normal conducting coil of the COBRA magnet.

These fluctuations were found to eventually carry over to the data acquisition electronics. Unfortunately, the performance of the data acquisition depends on the temperature. Although it is possible to calibrate for this effect, that calibration only holds for a certain temperature. This effect was found to affect the performance of the XEC adversely [77].

Moreover, the massive heat load by the equipment would increase the overall temperature to the point where the electronics overheats and automatically switches off [78]. A first attempt to counter this effect was undertaken by the installation of a cooling system. This chiller would start cooling once an upper limit is reached and then run at maximum power until the temperature of the coolant dropped again below a predefined value.

This managed to lower the effect of the environment outside the hut on the temperature inside, yet caused fluctuations on its own. These appeared as spikes in the temperature when the chiller started or stopped. In order to improve the situation further, the decision to implement a PID-control was taken.

4.1.1 The PID-Control

This section describes the working principle of a PID control. Further, the parameters to be used in this context are defined.

A possible way to handle these spikes generated by the chiller is to control the valve connecting the cool water tank with the heat exchanger. In this situation a PID-control is implemented. Its name comes from the three terms acting on the controlled valve opening: a proportional term P, an integral term I and a differential term D.

The proportional term P is most straight forward. It is proportional to the deviation ΔT between the measured temperature and requested (constant) temperature. The constant k_p has to be determined experimentally.

$$P = k_p \Delta T \tag{4.1}$$

This term reacts linearly on the deviation and yields no contribution once the measured value equals the desired one. Thus this term will yield a constant difference ΔT under ideal circumstances where the cooling due to the proportional term compensates the heating of the experiment.

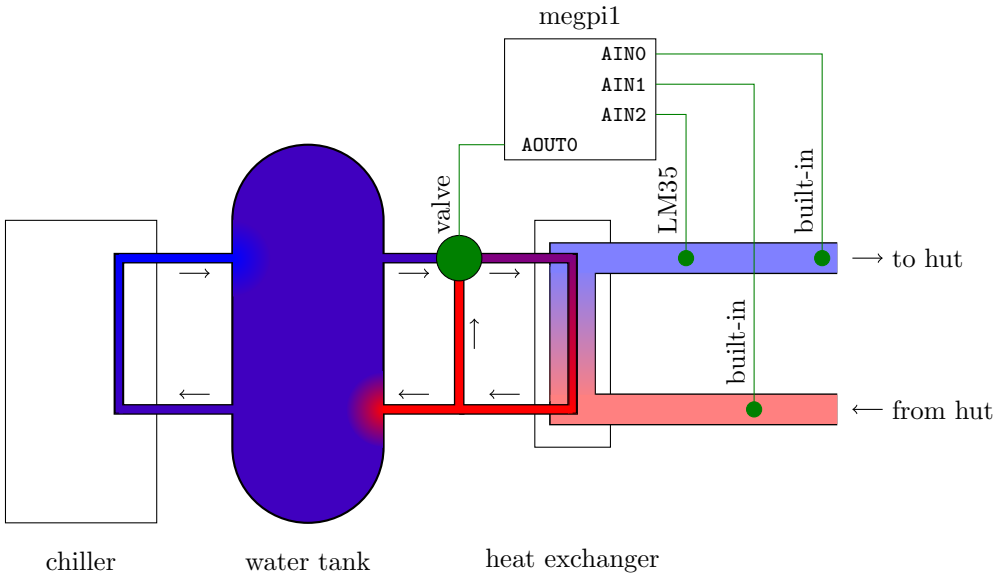

Figure 4.1: Schema of the cooling system. Description in text.

The integral term I is proportional to the integral of all the previous deviations ΔT_n with a constant k_i, that needs experimental determination.

$$I = k_i \sum_n \Delta T_n \tag{4.2}$$

This term is crucial to remove residual deviations that the proportional part cannot take care of. Even a small deviation summed over a long enough time will become significant enough to result in an appropriate impact of the integral term.

The differential term D is proportional to the first derivative of the deviation with respect to time. The constant k_d has to be determined from measured data as well.

$$D = k_d \frac{d\Delta T}{dt} \tag{4.3}$$

As this term reacts to changes of the temperature difference, it leads to a faster response on sudden changes either in the measured or requested temperatures. Additionally it helps to reduce overshooting, i.e. it helps to dampen oscillations.

The controlled variable v (e.g. valve position) is then determined by the sum of the three terms.

$$v = P + I + D = k_p \Delta T + k_i \sum_n \Delta T_n + k_d \frac{d\Delta T}{dt} \tag{4.4}$$

The controlled variable is calculated after every step and the system adjusted accordingly, e.g. the valve opens a bit more if it is too hot. After some time, an adjustment of the controlled variable (e.g. opening the valve) has an effect on the temperature. Using this feedback, the temperature can be controlled. Any deviation from the requested temperature will then lead to an appropriate counter measure, providing that the parameters k_p, k_i, k_d were tuned correctly.

4.2 Hard- and Software

This section first describes the hardware used for the temperature control in the detector hut. In the second half, the software developed to control the hardware is described. This includes user interfaces for easy access.

The cooling system for the temperature control of the detector hut is depicted schematically in figure 4.1. It consists of a water circuit on the left side coupled to the air cycle of the hut on the

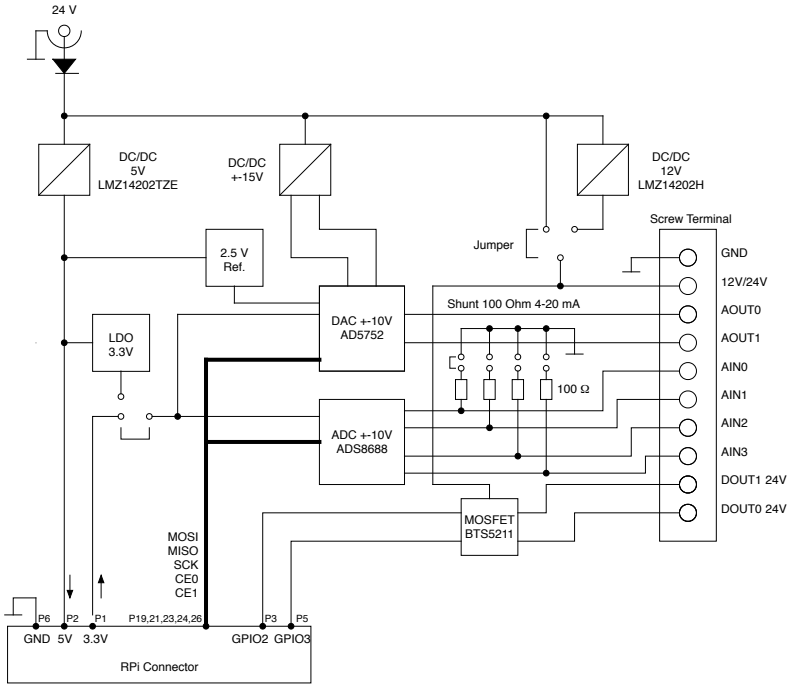

Figure 4.2: Schema of the custom board attached to the Raspberry Pi. Apart from the ground (GND) and voltage (12V/24V) it provides two analogue outputs (AOUT0, AOUT1, two digital outputs (DOUT0, DOUT1) and four analogue inputs (AIN0 - AIN3). Board and Schematics produced by U. Hartmann [80]

right side. They are coupled by a heat exchanger. In addition sensors are placed in the air cycle for a feedback on the temperature.

The chiller to the very left is the source of cooling. It maintains the water in the 35 l tank between 11 °C and 13 °C. Whenever the measured water temperature goes above the upper threshold, cooling kicks in until the lower threshold is reached. This yields a characteristic pattern observable in the hut temperature if it were not for the regulation discussed in this chapter.

The water fed to the heat exchanger consists of a mixture of cold water from the tank and warm water returning from the heat exchanger. The mixture is adjustable by the valve. The valve's position can be set continuously by the Raspberry Pi (megpi1). Thus the temperature of the water fed into the heat exchanger can be controlled.

The cold air from the heat exchanger is then fed to the detector hut. On the way there it passes two temperature sensors. The LM35 sensor [79] is the first one and currently in use. The second one was delivered and built in with the entire setup. It does not serve any particular use and is depicted only for legacy reasons. After passing through the detector hut the warmed up air returns to the heat exchanger passing the third temperature sensor.

The heart piece of the control is a Raspberry Pi (megpi1) reading the sensors out, setting the valve and providing an interface to adjust parameters. It runs Linux to host the custom software needed. In addition to the usual input and output channels, a custom board is attached. The block schematics for this board is presented in Figure 4.2.

The control of the valve is attached to the analogue output channel 0 (AOUT0). The valve can be set by adjusting the voltage between 0 V and 10 V, although the valve does not respond linearly. No significant changes were observed below 4 V and above 8V. This suggests that the ideal operation point would be somewhere in between.

The built in temperature sensors of the venting system are connected to analogue input channels. The sensor measuring the cooled air fed to the detector hut is connected to AIN0. Although read out, the obtained data is not used any further. The sensor measuring the air returning from the detector hut is read out using AIN1. Their resolution is unfortunately limited to 0.1 °C leading to jumps in the measured temperature.

To bypass this limitation an additional LM35 temperature sensor was installed. In a first step

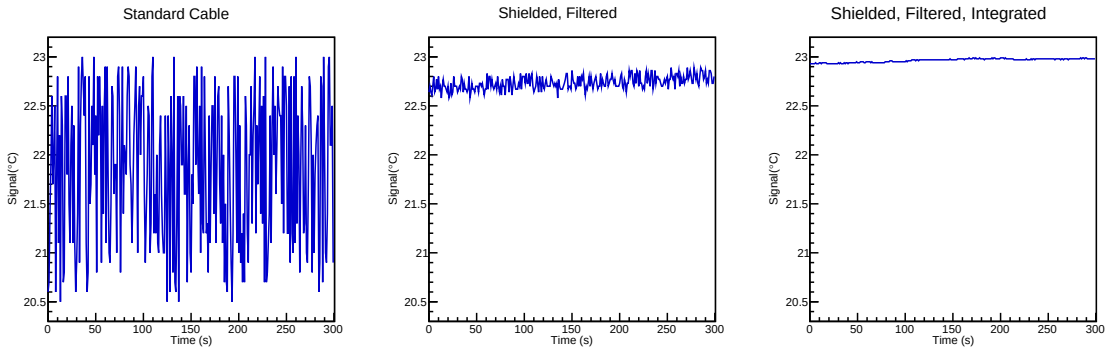

Figure 4.3: Obtained signal from the LM35 temperature sensor. To the left is the signal without any measures taken to reduce the noise. The middle figure shows the signal obtained after filtering voltage supply and signal in addition to shielding the connection. The right signal is obtained after averaging numerically in the readout software. Note that these measurements were taken one after another while the ambient temperature was gradually increasing, hence the increase in temperature from left to right.

it was connected directly to the analogue input channel AIN2 using twisted cables. This however was found to be noise dominated and unfit for the designed usage. The signal obtained that way is shown in the leftmost picture of Figure 4.3.

To improve the signal quality a shielded cable was taken. In addition filters have been added. A first set stabilises the voltage supplied from the Raspberry Pi. A capacitor just next to the voltage supply of the LM35 sensor filters high frequencies from the supplied voltage collected on the way through the cable. A final lowpass filter clears high frequency noise from the signal cable just before the Raspberry Pi. The sum of these hardware based measures yields the signal shown in the middle of figure 4.3.

The final signal used is shown on the right of figure 4.3. In addition to the hardware measures, the software was improved. Instead of one individual measurement, a set of 10 000 measurements is taken over a period of 1 s and then integrated afterwards.

In order to achieve the final goal of a constant temperature in the detector hut, two types of disruptions need to be considered. The first one comes from the chiller itself. Its periodic cooling pattern leads to jumps in the temperature of the air feed and as a consequence results in oscillations of the hut temperature itself. The second type comes from changes in the surroundings, e.g. day and night cycle.

The chiller effects can be dealt with a first feedback loop with the purpose to control the temperature of the air feed. Therefore the temperature measured by the LM35 sensor is compared to the requested value. Based on the difference between these two temperatures, the valve position is adjusted by the Raspberry Pi. This allows to adjust the temperature of the air feed to a desired value.

Changes based on the environment like the day-night cycle or ramping up the magnets can be observed in the temperature measured in the hut and the air flowing back to the heat exchanger. Under typical running conditions, these changes are much slower than the effects from the chiller.

These changes are dealt with through a second feedback loop by adjusting the requested temperature of air feed controlled by the first feedback loop. Thus a small increase in the temperature of the hut will lead to a reduced temperature of the air blown into the hut. This results in an increased cooling power countering the temperature increase.

The software on the Raspberry Pi is written in C++. It contains both PID controls used in the feedback loops mentioned above along with all the sensor readouts and valve steering. Each of the feedback loops is updated once every second. The updated status then is added to the memory-resident history and written to a history file.

To avoid running out of memory and stay efficient none the less, a cyclic design of the memory-resident history was chosen. This means that a container of defined size is allocated when the process gets started. The current position in this array is stored in an index. Whenever an entry is added it is placed at the position the index is pointing to. This potentially overwrites an old entry

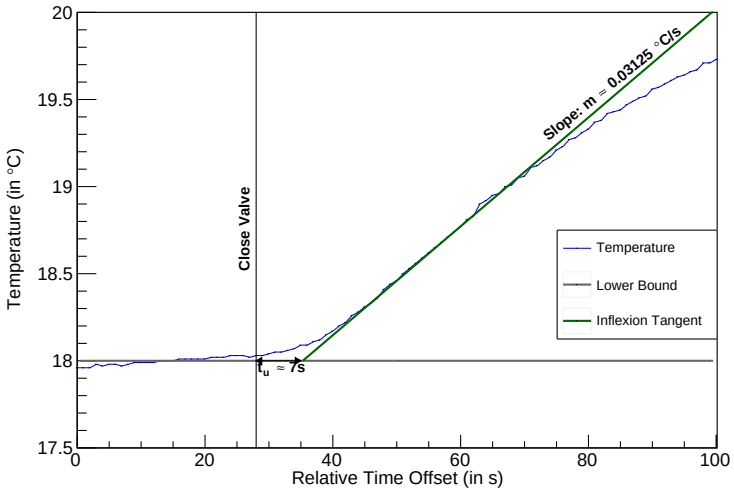

Figure 4.4: Temperature response curve to suddenly closing the valve. This is used to estimate the parameters k_p and k_i of the feedback loop.

at that position. Afterwards, the index is increased and if it passes the end of the container set again to the start.

In addition the software runs a lightweight web server [81] providing easy access to most of the aspects. It can be reached under `http://megpi1:8080` from the PSI internal network if running. To avoid accidental messing up with certain parameters, the human access is separated into default, user and expert access.

The default access `http://megpi1:8080/index.html` is used for display only purposes. It displays the temperatures read out from the sensors as well as the valve position and the requested temperatures. In addition the history in a desired time window is displayed in a diagram.

The user access `http://megpi1:8080/user.html` provides in addition to the default access the possibility to adjust the requested hut temperature and to switch both feedback loops together on or off. This is intended for usage by anyone operating parts of the experiment.

The expert access `http://megpi1:8080/expert.html` provides access to all relevant aspects. One can switch on or off each of the feedback loops individually. Furthermore the relevant parameters for each of the feedback loops can be read or set for each of the feedback loop or the valve position directly accessed if not controlled by the first feedback loop. This should only be used by experienced users.

In order to read the current status of the hut temperature control automatically, a dedicated UDP is created. This interface is used as access by the appropriate MIDAS slow control front end. Consequently, the full functionality of MIDAS is available to monitor the status of the temperature control. Manipulation of the PID control software through this UDP connection would be an option yet was not implemented to avoid modifications by shifters or other non-expert users.

4.3 Tuning of the PID Cycles

This section describes the first approach to determine the factors k_p, k_i and k_d. Further the issues encountered with them are shortly mentioned and the way they were resolved. This is however not a detailed manual on how to fine tune a PID control. Finally, the impact of the PID control on the temperature of the air feed is shown.

In a first step only proportional and integral terms are considered by setting $k_d = 0$. The values for k_p and k_i are estimated by the use of the Nichols Ziegler method [82]. For this purpose, the cooling was activated to reach a certain temperature without being necessarily stable. At a certain point, the valve was suddenly fully closed and the response of the temperature acquired.

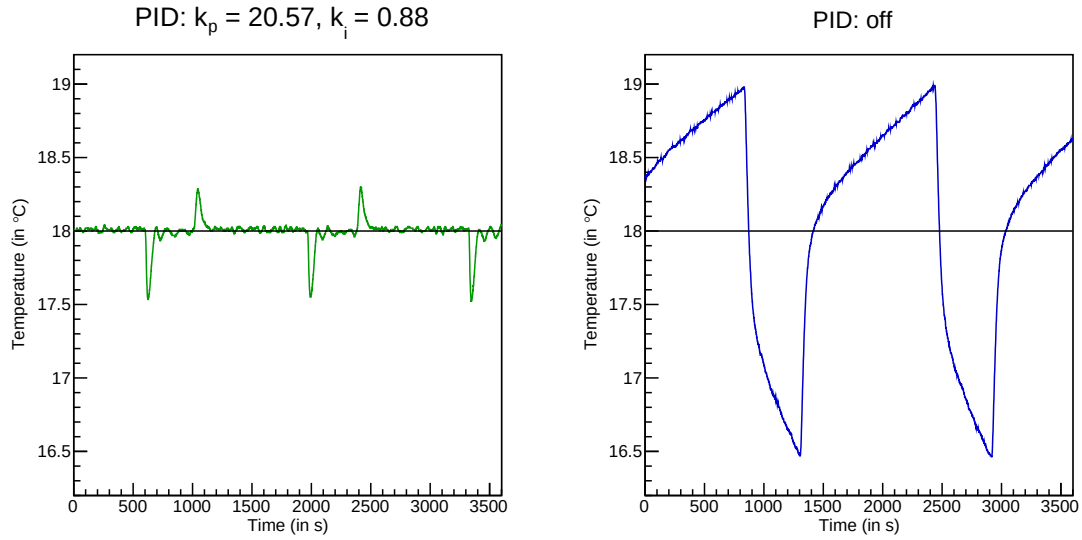

Figure 4.5: Effect of the PI-Feedback loop. On the left side, the temperature control is on regulating the air temperature to 18 °C. Any effects from the chiller can be seen as small peaks that get countered aggressively with some overshoot. On the right side, an unregulated curve is plotted for reference.

The obtained temperature curve is displayed in figure 4.4. The tangent to the point of inflexion of this curve is estimated. From this tangent one can estimate the slope $m = 0.031\,25\,\frac{^\circ\mathrm{C}}{\mathrm{s}}$ and the time difference $t_u \approx 7\,\mathrm{s}$ between closing the valve and the point where the tangent crosses the original temperature 18 °C.

From these two values one can estimate the parameters k_p and k_i by adjusting the tuning rules by Nichols and Ziegler to the given situation:

$$k_p = 0.9\frac{1}{t_u m}\cdot 5 = 20.57\,\frac{1}{^\circ\mathrm{C}} \qquad k_i = 0.27\frac{1}{t_u^2 m}\cdot 5 = 0.88\,\frac{1}{^\circ\mathrm{C\,s}} \tag{4.5}$$

The factor ·5 is not part of the original formula but was introduced based on experience and intuition. Earlier attempts without this factor showed to be slow to react and unfit to counter fluctuations efficiently.

A first test of these parameters is represented in Figure 4.5. The result with the control switched on is displayed in the left, a curve taken with the feedback switched off is displayed on the right for reference. One can clearly see that the effects of the chiller that cause the large oscillations on the right get reduced to small, sharp peaks. Each of the peaks is countered in aggressive manner at the cost of some overshooting.

These overshoots on their own are not a problem for the system as the final goal is to keep the hut temperature at a constant level. The observed spikes and the overshoots thereafter are only visible in the temperature of the air streaming into the detector hut. The detector itself will hardly react to these fluctuation due to its large heat capacity.

During operation when hardly any cooling was necessary due to the cold environment and many devices being switched off, large overshooting and slowly damped oscillations in the cold air temperature were temporarily observed. These were dealt with by setting $k_d = 60\,\frac{\mathrm{s}}{^\circ\mathrm{C}}$ and leaving $k_p = 20.57\,\frac{1}{^\circ\mathrm{C}}$ and $k_i = 0.88\,\frac{1}{^\circ\mathrm{C\,s}}$. These parameters worked very well in keeping the temperature stable during the pre-engineering run in 2020.

Using the same approach as initially used for the air temperature control, the parameters for the hut temperature control were estimated. During the pre-engineering runs, the parameters $k_p = 5\,\frac{1}{^\circ\mathrm{C}}$ and $k_i = 0.007\,51\,\frac{1}{^\circ\mathrm{C\,s}}$ proved to work. The differential part was not required to stabilise the temperature and thus $k_d = 0\,\frac{\mathrm{s}}{^\circ\mathrm{C}}$ was used for the hut temperature control.

Note however that these parameters were estimated without having the full electronics available inside the detector hut. Nonetheless, the PI-control implemented for the detector hut managed to stabilise the temperature inside the detector hut when the COBRA magnet was switched on

respectively off. The ideal working temperature has yet to be determined once all heat loads are installed in the final configuration during the upcoming engineering run later this year.

Chapter 5

Calibrations based on Mott Events

5.1 Introduction

This introduction sums up the theoretical background and formulas used for the Mott scattering process of the positron on the MEG II target. This builds the foundation for the implementation of the process in the MEG II simulation code briefly summarised in the second subsection.

5.1.1 A Short Summary of the Theoretical Background

The name "Mott Events" refers to the underlying Mott scattering process [83], that happens when a particle with spin, a positron in this case, scatters off a resting nucleus. In order to profit from this process, a positron beam from the target E is used. By tuning the PiE5 beam line [39] appropriately, a positron beam of highly relativistic 53 MeV positrons is obtained.

Given that the positron momentum is a factor 100 larger than the positron mass, one can treat it as massless for the purpose of calculating the scattered momentum p'. Under this assumption and neglecting the thermal motion of the scattering target, it can easily be shown that the scattered momentum p' can be calculated as

$$p' = \frac{p}{1 + \frac{p}{Mc}(1 - \cos\Theta_\mathrm{s})} \tag{5.1}$$

where p is the momentum of the positron before it was scattered and Θ_s the angle between the incoming and the outgoing direction. The mass M is given by the nuclei in the scattering target, which corresponds to the ordinary muon stopping target made of polyvinyltoluene. The mass of a hydrogen nucleus is $M = 938\,\mathrm{MeV/c^2}$ whereas for a carbon nucleus, the value $M = 11.2\,\mathrm{GeV/c^2}$ is assumed.

When considering the ratio between momentum of the positron and the mass of the nucleus only small changes to the positron momentum are expected in case of a hydrogen nucleus and a minimal one for carbon. The analytical functions are shown in Figure 5.1.

With the incoming beam well controlled, positrons with known properties are passing through the spectrometer. Note that for the scattering process on carbon nuclei, the momentum difference due to the recoil is comparable to the initial momentum spread due to the acceptance of the positron beam.

In order to estimate the rate obtained by this process in the spectrometer, one requires the probability for a positron to be scattered under a certain angle. Thus, the differential scattering cross-section is required. It is described in detail by Hofstadter [84] and a short summary of the most important findings is presented here. For a pointlike nucleus, this can be written as

$$\left(\frac{\mathrm{d}\sigma}{\mathrm{d}\Omega}\right)_\mathrm{point} = \left(\frac{Ze^2}{2E_0}\right)^2 \frac{\cos^2(\Theta/2)}{\sin^4(\Theta/2)} \frac{1}{1 + \frac{2E_0}{Mc^2}\sin^2(\Theta/2)} \tag{5.2}$$

with the atomic number $Z = 1$ for hydrogen nuclei and $Z = 6$ for carbon. The energy E_0 is the initial energy of the incoming positron. As the positron is highly relativistic in this particular case,

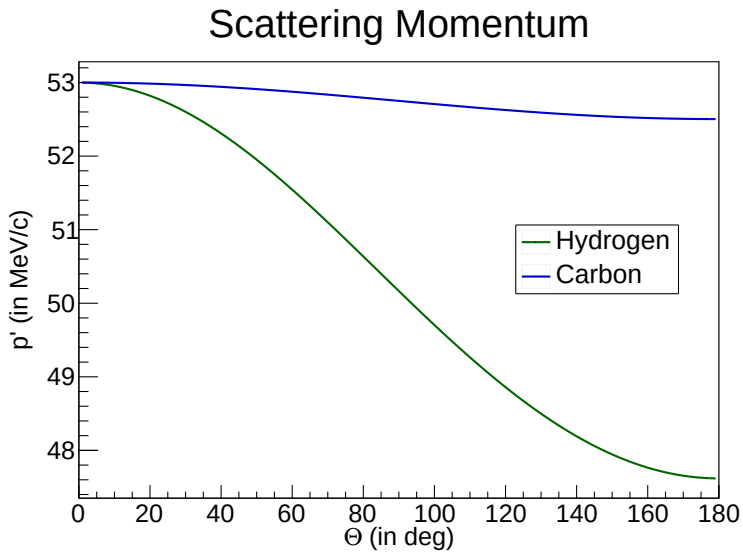

Figure 5.1: Momentum p' of the scattered particle as function of the scattering Angle Θ.

energy and momentum are considered to be equal, i.e. $E_0 = pc$. As described by Hofstadter, the finite size effects can be dealt with by adjusting the formula to

$$\frac{\mathrm{d}\sigma}{\mathrm{d}\Omega} = \left(\frac{Ze^2}{2E_0}\right)^2 \frac{\cos^2(\Theta/2)}{\sin^4(\Theta/2)} \frac{|F(q)|^2}{1 + \frac{2E_0}{Mc^2}\sin^2(\Theta/2)} \tag{5.3}$$

where a nuclear form factor $F(q)$ was introduced. It is the same form factor as observed in x-ray and electron diffraction, which seems reasonable, considering how closely related the processes are. The implementation for the MEG experiment is documented in [85] and no reason was seen to change any of the models or numerical values when adapting the method for MEG II. In summary the form factor was approximated as

$$F(q) = 3\frac{\sin(x) - x\cos(x)}{x^3} \qquad x = \frac{qR_u}{\hbar c} \tag{5.4}$$

where q stands for the momentum transfer and the radius R_u is obtained when approximating the atomic nucleus as an uniformly charged sphere. This approximation was taken from [86] and is fully sufficient for these considerations. The momentum transfer q can be calculated as

$$q = \sqrt{2pp'(1 - \cos\theta)} \tag{5.5}$$

as can be confirmed with a simple calculation.

5.1.2 The Implementation of Mott Events in the Simulation

In order to optimise the performance of the simulation in GEM4, a dedicated primary particle generator was implemented for the MEG experiment. As the underlying physics remains unchanged for MEG II, no major changes were needed to adapt this part of the code to the new needs of the MEG II experiment. This dedicated particle generator allows to take control over the detailed generation process. This is crucial, as the scattering cross-section is largest for small scattering angles, i.e. for positrons that are scattered at angles too small to enter the acceptance of the detector.

The generation of the scattered positron consists of several steps. The first of which is to determine its initial momentum and direction, which happens based on the measured beam profiles. This includes properties like the beam momentum and its standard deviation, the beam position and extent as well as the beam divergence. These parameters are set by a macro at run time.

Based on the incident momentum, the Mott scattering cross-section for that very momentum is calculated for each event. For practical reasons, only the relative ratio between different scattering

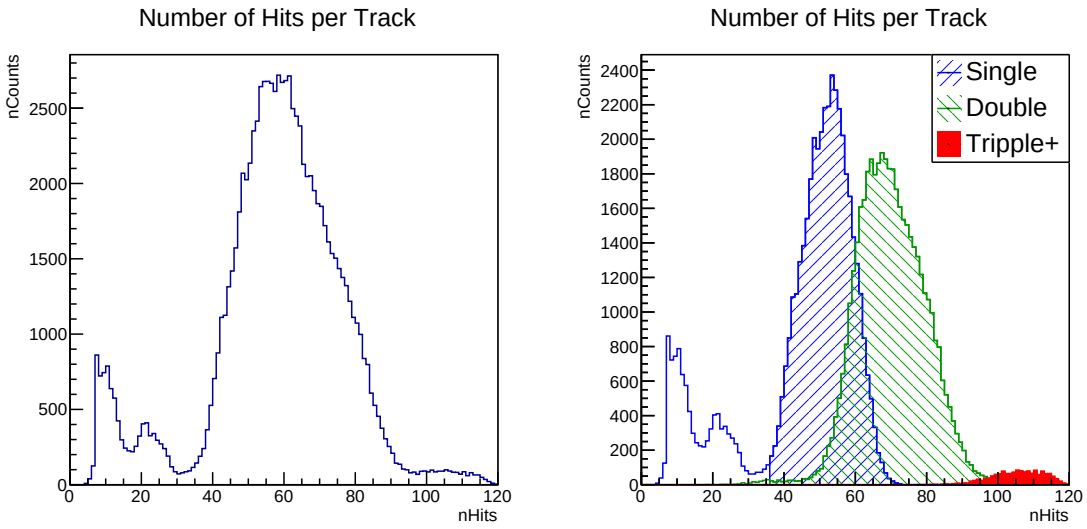

Figure 5.2: The number of hits per reconstructed track. On the right side, they are split by the numbers of turns in the CDCH the track is associated with. Roughly 42 % of the good reconstructed tracks are single-turns, 47 % are double-turns.

angles is considered while the distribution is not normalised in this step. Eventually, a scattering angle is randomly selected according to the calculated distribution. This step then defines the outgoing direction as well as the outgoing momentum. The generator is designed in such a way that it allows to accept minimal scattering angle and bounds in terms of the resulting azimuth direction. These limitations are set by a macro at run time of the simulation.

In a last step, the particle is placed on the MEG II target structure with the calculated outgoing momentum and direction. Only at that point, the propagation of the particle starts through the use of usual GEANT4 particle propagation tools [87]. The further processing happens through the simulation procedures by GEM4, detector response generation by MEGBartender and event analysis by MEGAnalyzer. More details about the MEG and MEG II simulation software can be found in [88].

5.2 Characterisation of the MEG II Cylindrical Drift Chamber with Mott Simulations

This section deals with the potential of using Mott scattered positrons for the characterisation of the drift chamber. The first part is about the benefits without deploying additional analysis techniques while the last part deals with the double-turn method. While these methods are not new and were already used in the MEG experiment [85], they have been adapted, improved and applied to the MEG II situation.

5.2.1 Expected Number of Hits per Track

The first thing one needs are good criteria to select the tracks worth being further investigated. The simplest possible criterion is based on the number of hits in the drift chamber. Their distribution is shown in Figure 5.2.

In the left graphic, the number of hits per reconstructed track is shown. On the right side, they are sorted by the number of turns of the associated track in the detector. From this, one can extract that a single-turn track consists of 35 to 70 hits, a double-turn of 50 to 100.

The two peaks to the left below 35 hits have their origin in only partially reconstructed tracks. Although it was possible to fit the cluster of CDCH hits, they could not be merged with any other clusters to form a complete track. This can happen for several possible reasons.

The most obvious one is that the positron track hits some pixels of the timing counter (pTC)

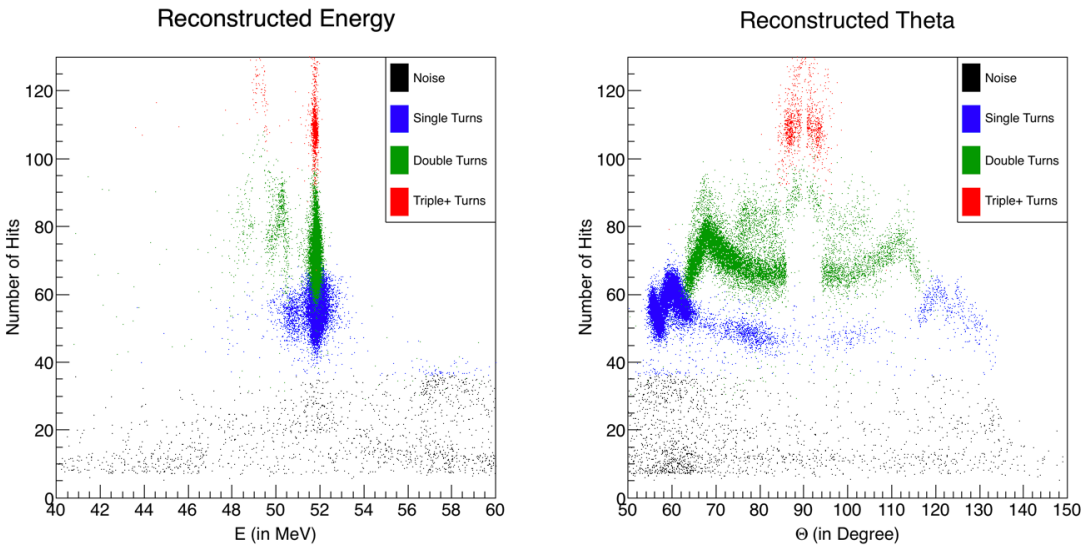

Figure 5.3: The number of hits in dependency of energy on the left side and in dependency of theta on the right side. They are coloured according to the number of reconstructed turns. To discriminate between noise and ordinary single turns, a threshold of 35 hits was set.

or any other material. This leads to an energy loss or scattering of the positron. If the positron then returns back into the CDCH, its momentum vector has been altered to the point where the matching algorithm does not combine these tracks as the second half with the altered energy would spoil the resolution.

Additionally it is possible that the track passes through the end face getting just a few hits in the CDCH itself. Due to the low amount of hits, the track does not get fitted properly with large deviations in the parameters. These parameters differ too much from the rest of the track such that they don't get matched.

Thus, partial tracks that are not properly matched can get reconstructed even if the algorithm does not provide meaningful results. They can come either from a partial crossing of the CDCH (e.g. ending in the endplate) or a single crossing that remains unmatched for good reasons. Observing two peaks in Figure 5.2 implies that a single crossing of the CDCH corresponds to roughly 15 to 35 hits.

This explanation is supported by the results shown in Figure 5.3. For clusters containing only about 10 hits, the reconstructed energy in the left plot seems to behave arbitrarily in a range from far below the nominal value to far above the initial energy. Especially the second case can only happen if the momentum of the positron is badly estimated. Although the Θ distribution does not show such a clear evidence of bad reconstruction, the Θ distribution is naturally spread out in contrast to the energy distribution. Thus a similar relative error is far less obvious in Θ than in energy.

The well reconstructed turns are separated in single-turn tracks (blue), double-turn tracks (green) and tracks with at least three turns (red). For a good track, the number of recorded hits is roughly proportional to the track length inside the CDCH. On the left plot one can see, that the resolution of the reconstructed energy increases with the number of turns, corresponding to more data points for the fit.

For the positrons scattered on carbon, their energy of roughly 52 MeV does not show any correlation with the number of hits in the CDCH. Positrons scattered on a hydrogen core exhibit a dependency between energy and the number of hits. This is due to the fact that for these kind of positrons there is a strong correlation between scattering angle Θ and the energy of the scattered positron.

For geometric reasons, there is a strong dependency between the total length of the track inside the CDCH and the scattering angle Θ. This immediately implies a dependency of the number of hits on the scattering angle. This can be seen from the different curves present in figure 5.3. In general, the closer the angle Θ is to 90°, the shorter is one crossing of the drift chamber - thus the

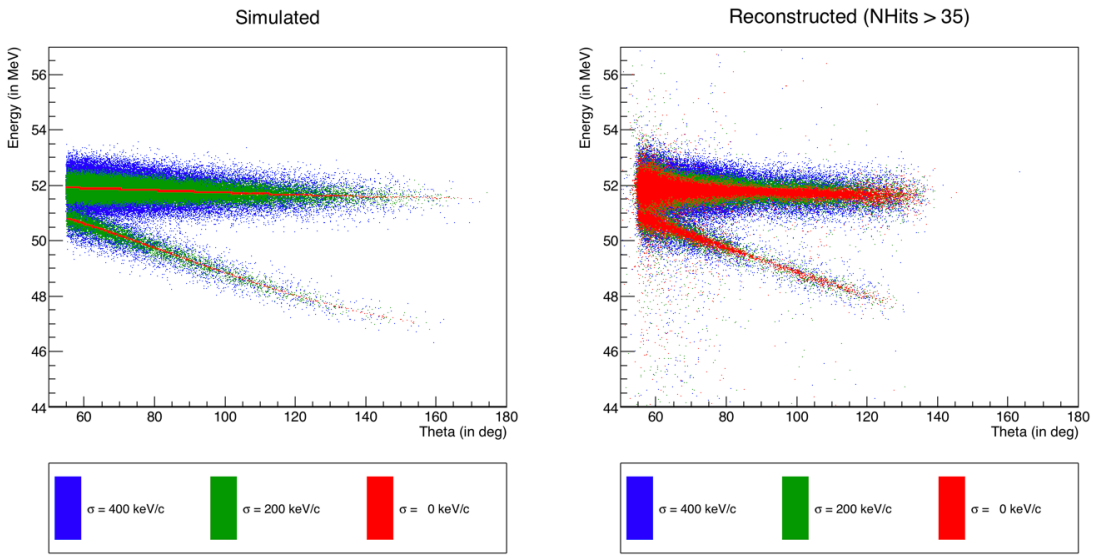

Figure 5.4: Energy in the simulation vs the polar angle Θ. The figure on the left side represents the simulated values as generated in the simulation code. The figure on the right shows the values obtained by the reconstruction algorithms. Three different sets of data are drawn. They correspond to different values for the spread in momentum of the incoming positron beam.

number of hits per segment of the track decreases towards 90°.

At certain scattering angles (e.g. between 63° and 67°), the track starts to cross the CDCH an additional time, leading to a new segment of the track in the CDCH and thus generating another cluster. This results in an increase of detected hits. If the additional cluster is added from the center to the outer part of the drift chamber as it is the case around 65°, the track begins an additional turn.

Although geometry predicts only one number of turns for a given angle Θ, there are more than one number of matched segments present for certain angles. Especially around 80°, single and double-turn tracks appear at the same time. The most probable reason for this is a failed matching in the analysis code. For some of the tracks at a given angle, the last partial track gets attached to the full track while for others, the deviation from the rest of the track is too large and thus the last fragment is rejected. This results in additional tracks in the CDCH that act as source of the noise described above.

5.2.2 Reconstruction of the Positron Variables

Based on the analysis of the number of hits per good track, only tracks with more than 35 hits are considered in the further evaluations. Amongst the reconstructed positron variables in the CDCH, three of them are of major interest for the MEG II experiment. These are namely the energy of the positron, the polar angle Θ with respect to the direction of the incoming positron beam and the azimuthal angle ϕ.

In Figure 5.4 the reconstructed energy is plotted against the polar angle Θ. On the left side, there are the simulated values as they are generated in GEM4. On the right side are the reconstructed values obtained after running the analysing algorithms. Three sets of data are plotted. The red one corresponds to no spread in the momentum of the incoming beam. The set represented in green corresponds to a momentum spread of $\sigma = 200\,\mathrm{keV/c}$ which is an optimistic estimate of the true beam quality and the blue set was generated with a pessimistic assumption of a beam spread of $\sigma = 400\,\mathrm{keV/c}$. The exact value depends on the tuning of the beamline as well as the chosen slit positions. Closing the slits lowers the momentum spread as well as the positron rate such that a trade-off has to be made.

As expected, the larger the spread in momentum of the incoming beam, the larger the spread is in the reconstructed energy. Note that there is a negligible amount of events reconstructed with a polar angle Θ larger than 140°. This is due to the geometric acceptance of the DCH. Another

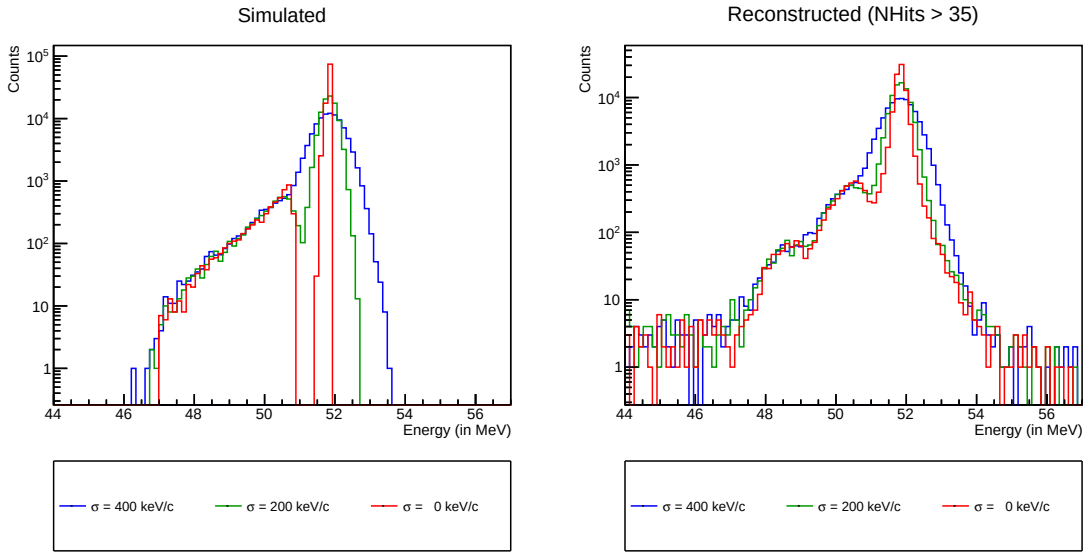

Figure 5.5: Energy spectra of the simulation. The figure on the left side represents the simulated values as generated in the simulation code. The figure on the right shows the values obtained by the reconstruction algorithms. Three different sets of data are drawn. They correspond to different values for the spread in momentum of the incoming positron beam.

expected feature is that the separation between carbon based events and hydrogen based events is less clear and starts to vanish with the reconstruction.

A notable observation is the spread in energy for small angles around 60°. As can be best seen from the red dataset, the energy is more spread out than for events in the central region. This is due to the fact that tracks at these angles have at most one turn in the drift chamber and rather few hits. Thus their energy resolution is lower with respect to events with longer tracks in the drift chamber. This effect can hardly be observed on the other side of the drift chamber due to the low number of positrons scattered in this direction.

Further, there appears to be a slightly lower number of events for the low beam spreads in the lower hydrogen-branch at around 90°. This is due to the fact, that tracks at these angles usually perform a very large number of turns in the DCH, thus resulting in more hits than the reconstruction algorithm can take. Thus the algorithm fails for some of these events resulting in a lower reconstructed event rate around these angles.

The obtained energy spectra are shown in Figure 5.5. Again, the left side shows the generated values at GEM4 level whereas the right side shows the results of the reconstruction algorithms. The clear separation of carbon based and hydrogen based events for low beam spread is replaced by a small dip in the energy spectrum just above 51 MeV. The second dip below 50 MeV is due to the strong correlation between energy and polar angle for hydrogen based events. This energy corresponds to an emission angle of 90° where the reconstruction algorithms fail in some cases.

The main carbon based peak can be fitted with a Gaussian or the sum of two Gaussians as represented in the following equation

$$f(E) = N_c e^{-\frac{(E-\mu)^2}{2{\sigma_c}^2}} + N_t e^{-\frac{(E-\mu)^2}{2{\sigma_t}^2}} \tag{5.6}$$

where both of the two Gaussians share the same mean μ but core and tail have an individual constant $N_{c,t}$ and an individual standard deviation $\sigma_{c,t}$.

For the fit each set of data was additionally divided in two separate ranges. The centre holds all events with a polar angle between 70° and 110°. These events hit the drift chamber in its central region and usually perform a double-turn track. The edge holds the rest of the events that often perform only a single turn track. The results of each fit are shown in table 5.1.

As one would already expect from Figure 5.4, the central part performs better yielding an increased resolution with respect to all the events of the same dataset. The result obtained for no beam spread hint for an energy resolution of (74.4 ± 1.1) keV in the central region of the detector

Beam Spread (keV/c)	Region	μ (MeV)	N_c ($\times 10^3$)	N_t ($\times 10^3$)	σ_c (keV)	σ_t (keV)
0	all	51.83	5.46(5)	1.33(5)	95.8(10)	237(4)
0	centre	51.79	2.98(5)	0.39(5)	74.4(11)	160(6)
0	edge	51.86	3.03(4)	1.01(5)	100.4(16)	243(4)
200	all	51.83	3.04(4)	0.34(5)	232(2)	421(13)
200	centre	51.78	1.281(10)	-	223.4(10)	-
200	edge	51.86	1.82(5)	0.32(5)	235(3)	414(14)
400	all	51.83	1.951(9)	-	436.3(15)	-
400	centre	51.78	0.699(5)	-	408(2)	-
400	edge	51.86	1.262(7)	-	447(2)	-

Table 5.1: Energy resolutions extracted from the energy spectra for different beam spreads. For some cases the sum of two Gaussians for core and tail are used whereas in other cases the core Gaussian already offers rather good results. The data is divided into two regions: the central part of the detector with a polar angle between 70° and 110° and the edge of the detector outside this range. Note that this implies that the edge region mainly contains events from the DS side. This explains the slightly lower average μ for the central region as these events lose more energy in the Mott scattering process.

for double-turn tracks and for an energy resolution of (100.4 ± 1.6) keV at the edge of the detector for single turn tracks. This difference is explained by the number of hits available to extract the positron variables.

One can observe further, that there is less contribution of the Gaussian describing the tail in the central region. A rough estimate for the dataset without any beam spread shows, that there are almost 80 % of the events in the central region in the core Gaussian. For the edge of the detector, there are roughly the same amount of events in the core Gaussian as are in the tail Gaussian.

This can be explained by a dependence of the energy resolution on the polar angle Θ. This can be seen from Figure 5.4. One can clearly see, that the data for no beam spread in red has a rapidly changing width in energy for Θ below 60° and is more or less constant between 70° and 110°. Thus for the central range, the assumption of a single core Gaussian matches well with the reality and needs only a small correction. However on the edge, many more different spreads contribute to the distribution. Thus the assumption of a single core Gaussian needs a large correction hence a large contribution of the tail Gaussian.

At the level of higher beam spreads, the uncertainty in energy due to the beam spread increases and becomes dominant over the uncertainties due to the reconstruction. As a result, the small differences in the resolution of the reconstructed energy vanish with respect to the beam spread and the spectrum can be fitted with a single Gaussian. A beam spread of 400 keV/c dominates completely over the deviations in resolutions for different Θ and thus for these sets of data, all spectra can be fitted with a single Gaussian.

Another interesting observation can be made by looking at the fitted means of the distribution in Table 5.1. The obtained values for the central regime are slightly below the obtained value for the entire set and the values obtained for the edge are slightly above these values. This effect is very small yet still significant. This is due to the fact, that the edge mainly contains DS events. These get scattered at a rather small angle ($\Theta < 70°$) compared to the ones in the central region ($70° < \Theta < 110°$). Due to the larger angle, the positrons detected in the central region transfer slightly more energy to the carbon nuclei when scattered on the target and thus have slightly lower momentum in the CDCH.

In order to extract only the detector response, one can calculate the difference between the true energy of the positron as obtained in the generation process and the reconstructed value obtained by the analysing algorithms. With this method it is possible to access not only the resolution in energy but the resolutions in the polar angle Θ and the azimuthal angle Φ as well. This is only possible for MC simulations where the values can be extracted directly from the generation process. For a real experiment, these values are not accessible.

In order to confirm the above statement, the deviation between reconstructed energy and generated energy has been plotted against the generated polar angle. The results are shown in Figure 5.6. The plots confirm the expectation from above that the resolution depends on the angle Θ. In addi-

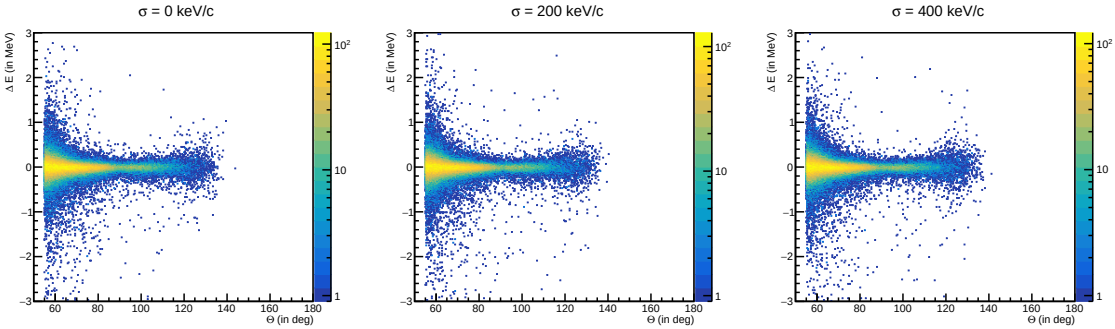

Figure 5.6: The difference between reconstructed energy and generated energy vs the generated polar angle Θ. Three different assumptions on the beam spread σ are presented.

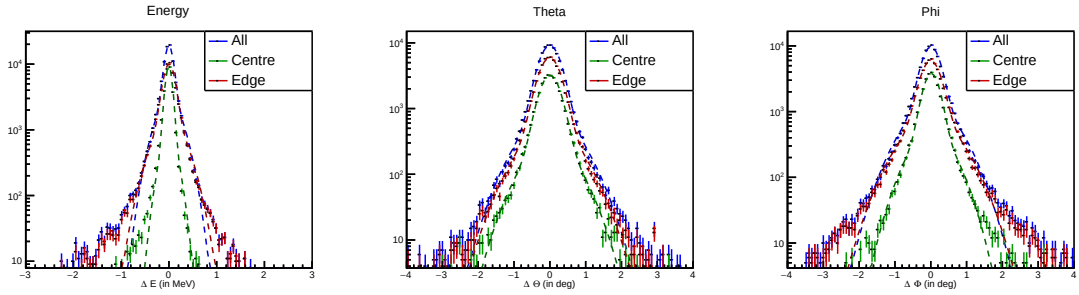

Figure 5.7: Distributions of the reconstruction errors for the positron variables energy, polar angle and azimuthal angle. Due to their similarity, only the results for a beam spread of 200 keV/c are shown. They are split in two regimes. The central part covers polar angles $70° < \Theta < 110°$. Other values are considered to hit the edge of the drift chamber. Each of the curves is fitted with the sum of two Gaussians as given in Equation 5.6. The results are shown in table 5.2

tion it becomes apparent that the obtained distribution widens up again for polar angles $\Theta > 110°$. This is due to the symmetry of the CDCH. However, the US region is much less populated than the DS region due to the asymmetry of the Mott cross-section.

One can further notice, that there is no visible impact of the beam spread on the final distribution. For that, only the differences between generated and reconstructed values for the dataset with a beam spread of 200 keV/c are plotted in Figure 5.7. They are fitted with the sum of two Gaussians as described by equation 5.6 and the results of the fit are gathered in Table 5.2.

Like already observed in previous plots, it is confirmed once more that the energy resolution is better in the central region of the CDCH compared to its outer region. This trend however does not apply to the polar angle Θ where the resolution appears to be far less dependent of the region. The same applies to the azimuthal angle Φ.

The resolutions for the energy stay in the same order of magnitude as in the previous Table 5.1. However, the obtained resolution in the central region and the overall resolution are clearly better than what was obtained from the energy spectra with no beam momentum spread. On the other hand, the resolution at the edge of the CDCH does not change on a significant level.

This can be explained through the relation between incoming and outgoing momentum in the Mott scattering process as described with Equation 5.1. The momentum of the outgoing positron depends on the scattering angle Θ_s which corresponds to the polar angle Θ up to the beam divergence.

Due to the recoil on the carbon nuclei, the momentum of the generated positrons differ in the central range significantly more than in the range between 55° and 70° contributing most to the edge region. As a result, the energy resolution for the central region extracted from the energy spectra is affected by this initial momentum spread of roughly 40 keV/c. In the outer region, the energy resolution is much larger than the initial momentum spread of roughly 10 keV/c on the DS side.

The resolution of the polar angle Θ only differs slightly between the central region and the edge

Variable	Region	N_c ($\times 10^3$)	N_t ($\times 10^3$)	σ_c	σ_t
Energy	all	16.88 ± 0.11	2.57 ± 0.08	(82.4 ± 0.7) keV	(250 ± 3) keV
Energy	centre	8.82 ± 0.09	0.64 ± 0.06	(65.5 ± 0.7) keV	(170 ± 5) keV
Energy	edge	8.84 ± 0.07	1.28 ± 0.07	(108.2 ± 1.3) keV	(306 ± 6) keV
Theta	all	8.37 ± 0.05	0.69 ± 0.04	$(0.270 \pm 0.002)^\circ$	$(0.711 \pm 0.012)^\circ$
Theta	centre	2.92 ± 0.03	0.26 ± 0.02	$(0.259 \pm 0.003)^\circ$	$(0.65 \pm 0.02)^\circ$
Theta	edge	5.43 ± 0.04	0.46 ± 0.03	$(0.274 \pm 0.002)^\circ$	$(0.722 \pm 0.015)^\circ$
Phi	all	8.55 ± 0.05	1.11 ± 0.04	$(0.232 \pm 0.002)^\circ$	$(0.670 \pm 0.009)^\circ$
Phi	centre	3.34 ± 0.04	0.43 ± 0.03	$(0.205 \pm 0.003)^\circ$	$(0.554 \pm 0.013)^\circ$
Phi	edge	5.22 ± 0.04	0.70 ± 0.03	$(0.249 \pm 0.002)^\circ$	$(0.722 \pm 0.012)^\circ$

Table 5.2: Resolutions for the positron variables energy, polar angle and azimuthal angle for a beam spread of 200 keV/c. The centre is defined by polar angles $70^\circ < \Theta < 110^\circ$, the edge contains the rest of the events in the outer regions of the DCH. Especially for the energy resolution, a clear difference between central and outer region can be observed whereas the angular resolutions appear more stable.

of the CDCH. This implies that a good reconstruction of the polar angle is possible even with a lower number of hits.

For the azimuthal angle Φ, there is a clear difference between the centre and the edge of the CDCH. This is due to the fact, that the extraction of the angular positron variables requires an extrapolation of the track to the target. The changes in Θ are not affected by the curvature of the track in the same extend as the changes in Φ. As can be seen in figure 5.8 an overestimation in the track's radius and thus an overestimation in the positron momentum will lead to an underestimation in the azimuthal angle.

For the entire dataset obtained at a beam spread of 200 keV/c, a resolution in the polar angle of $\sigma_\Theta = (0.270 \pm 0.002)^\circ$ is obtained. This corresponds to a value of (4.71 ± 0.03) mrad. For the azimuthal angle a resolution of $\sigma_\Phi = (0.232 \pm 0.002)^\circ$ corresponding to (4.05 ± 0.03) mrad was obtained.

5.2.3 The Double-Turn Track Method

A more elegant way to extract the resolution of the positron variables momentum, polar angle and azimuthal angle for the CDCH is to consider tracks with at least two fully reconstructed and matched turns in the CDCH. Such a double-turn track can be separated into two parts called the first turn and the second turn. Each of the turns is fitted individually and separate values for the positron variables are extracted.

As both turns are obtained from the same positron track, they should yield the same values. Their differences relate to the uncertainties of the estimated positron variable and thus to the resolution in said positron variable. This method is unaffected by the momentum spread of the incoming beam and the detailed scattering process. In contrast to the method above, comparing reconstructed values to the MC truth values, the double-turn method does only rely on the available information in a track and thus can be used on real data.

For the CDCH, the double-turn analysis is performed while merging the partial tracks obtained from CDCH clusters to the complete track of the positron. The following steps are performed:

1. Find all pairs of matching partial tracks. Look for the pair that matches closest to the target on the inside of the CDCH. The first partial track of this pair is the last of the first turn, the second partial track is the first of the second turn.

2. Based on the found pairs of matching partial tracks, determine the order in which these have to be combined to form the complete track.

3. Combine the partial tracks up to the last of the first turn to get the complete first turn. Combine the rest of the tracks to form the second turn.

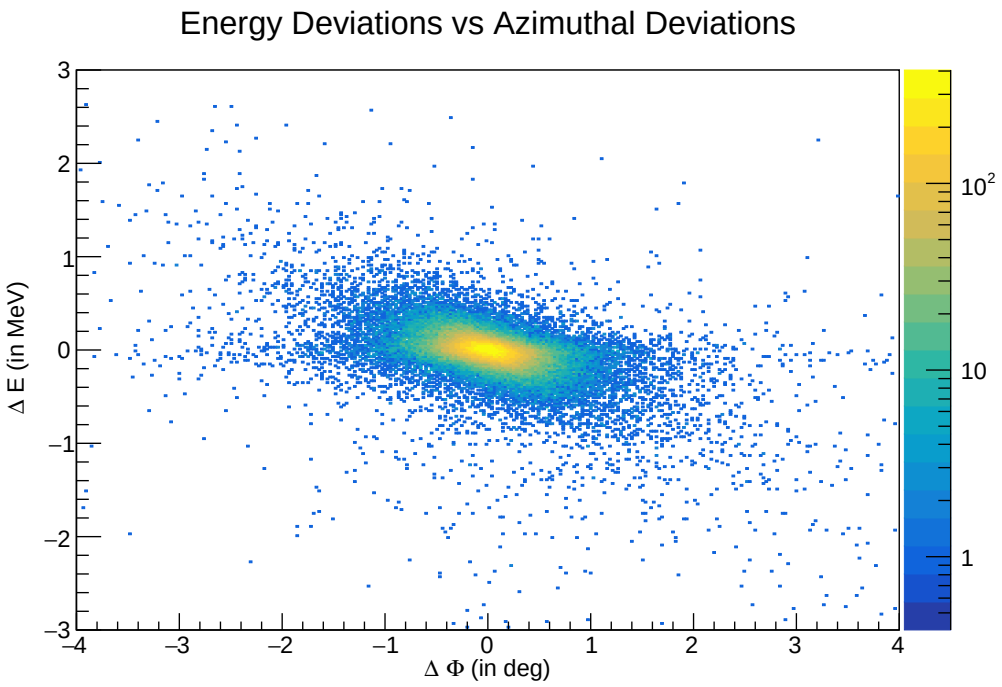

Figure 5.8: Estimated deviations in energy plotted against the estimated deviations in the azimuthal angle. The correlation factor of approximately -0.5 suggests that an overestimation in energy comes along with an underestimation in the azimuth and vice versa.

4. Fit both turns separately. Extract for each of the two turns the positron variables of interest (namely: momentum, polar angle and azimuth angle). Save this information together with the information about the two turns for further analysis.

5. Combine the first and the second turn together. Fit the final track again to get the final result for that track.

Note that with this algorithm, every partial track not belonging to the first turn is considered as part of the second turn. This implies that despite the name the second turn may consist of more than just a single turn and usually contains one and a half turns for a useful track. Further it may only contain half a turn due to the details of the algorithms. These tracks are flagged to contain insufficient information for the double-turn analysis.

This method is not only restricted to Mott events but may be used on Michel events as well as any positron track with two turns in the CDCH is eligible. The simulation results obtained from Mott, signal and Michel events are shown in Figure 5.9. They are fitted with the sum of two Gaussians as given by the following equation:

$$f(x) = N_c e^{-\frac{(x-\mu_c)^2}{2\sigma_c^2}} + N_t e^{-\frac{(x-\mu_t)^2}{2\sigma_t^2}} \tag{5.7}$$

In this equation, the x stands for the positron variable of choice - either momentum p, polar angle Θ or azimuth angle Φ. Further, it is separated between a core Gaussian denoted by a subscript $_c$ for the peak and a tail Gaussian denoted by a subscript $_t$ to fit the wider part of the distribution. Note that the two Gaussians don't share any parameters in this function in contrast to Equation 5.6 used earlier. The results of the fits are shown in Table 5.3.

The histograms obtained and displayed in figure 5.9 are normalised to the same area to get comparable results. The most important feature to notice is that the results for Mott events in orange are really close to the results for signal events in green for all of the positron variables considered. Opposed to this, the unfiltered Michel events in violet differ clearly. Even after selecting only Michel events with an energy close to the kinetic endpoint, the difference does not vanish completely. These observations are confirmed by looking at the obtained fit results in Table 5.3. The consistency between Mott and signal events and their discrepancy with Michel events state

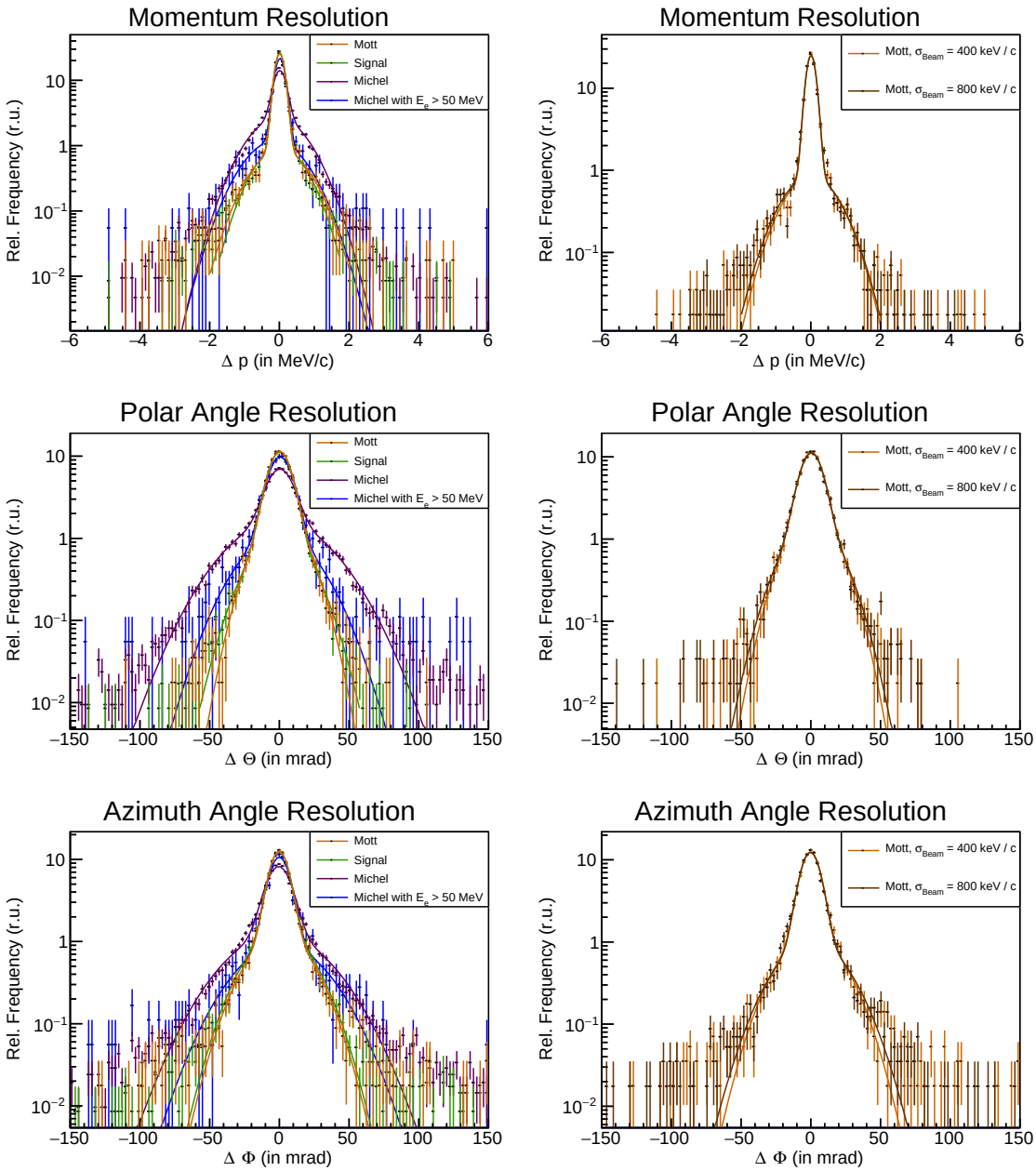

Figure 5.9: The distributions of the differences obtained by the double-turn analysis. On the left side, the obtained results based on Mott events (orange) are compared to MEG signal events (green) and to Michel events (violet/blue). On the right side, the obtained distributions are shown for Mott events assuming different initial beam spread in momentum. Each dataset is fitted with the sum of two Gaussians. The results obtained by this fit are listed in Table 5.3

Event Type	Variable	N_c	N_t	σ_c	σ_t
Mott 400 keV/c	p	24.7 ± 0.5	0.84 ± 0.07	(128 ± 2) keV/c	(684 ± 28) keV/c
	Θ	9.7 ± 0.3	1.7 ± 0.3	(7.1 ± 0.2) mrad	(15.5 ± 0.7) mrad
	Φ	11.3 ± 0.3	1.15 ± 0.14	(6.3 ± 0.2) mrad	(19.5 ± 0.9) mrad
Mott 800 keV/c	p	24.1 ± 0.5	0.83 ± 0.06	(130 ± 2) keV/c	(713 ± 29) keV/c
	Θ	9.7 ± 0.3	1.4 ± 0.3	(7.2 ± 0.2) mrad	(17.1 ± 1.0) mrad
	Φ	11.3 ± 0.2	1.0 ± 0.2	(6.4 ± 0.2) mrad	(21.5 ± 1.5) mrad
Signal	p	25.0 ± 0.4	0.91 ± 0.07	(127 ± 2) keV/c	(618 ± 24) keV/c
	Θ	10.1 ± 0.2	1.03 ± 0.13	(7.52 ± 0.13) mrad	(18.5 ± 0.7) mrad
	Φ	11.1 ± 0.2	1.25 ± 0.10	(6.21 ± 0.11) mrad	(20.0 ± 0.6) mrad
Michel	p	11.6 ± 0.2	2.60 ± 0.08	(164 ± 3) keV/c	(711 ± 10) keV/c
	Θ	5.41 ± 0.09	1.57 ± 0.05	(8.6 ± 0.2) mrad	(30.7 ± 0.4) mrad
	Φ	7.00 ± 0.10	1.21 ± 0.05	(8.11 ± 0.14) mrad	(30.4 ± 0.6) mrad
Michel $E_e > 50$ MeV	p	20.6 ± 0.8	1.17 ± 0.14	(136 ± 5) keV/c	(732 ± 44) keV/c
	Θ	8.8 ± 0.4	1.0 ± 0.2	(7.8 ± 0.4) mrad	(24 ± 2) mrad
	Φ	9.7 ± 0.4	0.9 ± 0.2	(6.8 ± 0.4) mrad	(27 ± 3) mrad

Table 5.3: The obtained results from fitting the histograms in Figure 5.9. For each event type the standard deviation and the constant of the two Gaussians is shown for the positron variables momentum (p), polar angle (Θ) and azimuth angle (Φ).

that Mott events are better at mimicking a signal event. Thus Mott events are given preference if it comes to predicting the behaviour of signal positrons.

Further the results displayed for Mott events show that a somewhat pessimistic assumption of an initial beam spread of 400 keV yields a statistically equal outcome to a very pessimistic model of 800 keV/c. This leads to the conclusion that the double-turn method is in fact independent of the momentum spread of the incoming beam and is a good way to extract the intrinsic resolution in the positron variables in the CDCH. Yet considering the fact that Michel events with a wider distribution in positron momentum show clear deviations from the values obtained for signal positrons, one should still keep an eye on the momentum spread of the beam and keep it as low as reasonably possible. Otherwise, the benefit from the quasi monochromatic beam is lost as the resolution probably changes for different energies.

By comparing the results obtained from Mott in the previous analysis shown in Table 5.2 clear discrepancies between the obtained standard deviations can be observed. This is due to the fact that in the previous analysis, the reconstructed value is compared to the true value used in the simulation. Thus only one of the values is affected by the limited positron variable resolution inside the CDCH. In the double-turn analysis two reconstructed values are compared, both of them are subjected to uncertainties based on the CDCH itself and on the reconstruction. In addition, the fit results are based on just parts of the full track and thus access only a fraction of the total information. When fitting the full track, more information can be used in the fit and thus a lower uncertainty in the positron variables is predicted.

Both effects lead to a worsening of the observed standard deviation with the double-turn analysis compared to the actual resolution in the positron variables in the CDCH. If only the first effect were present, it could be corrected for easily by applying a factor $\sqrt{2}$ that compensates for the accumulation of the two uncorrelated uncertainties. Including the second effect is harder and not done here, as the measured CDCH response in the final configuration will only be measured later this year during the engineering run.

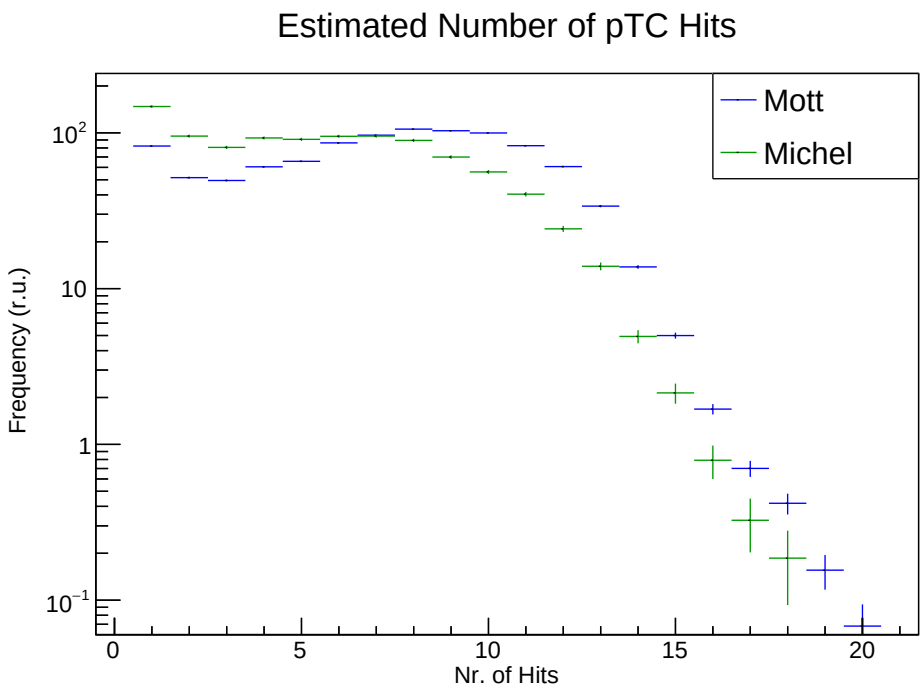

Figure 5.10: Estimated number of hits in the pTC for Mott and Michel events. Mott events are expected to have the same properties as a $\mu \to e\gamma$ signal positron, Michel events are the most dominant background in the spectrometer.

5.3 Characterisation of the Pixelated Timing Counter for MEG II with Mott Simulations

The geometry of the newly designed pixelated timing counter allows to benefit from Mott scattered positrons in unique ways. While the first part aims to get an understanding of the behaviour of the pixelated timing counter (pTC), the third subsection about the double-cluster method describes a new calibration method. The underlying method is similar to the double-turn analysis for the drift chamber and fully benefits of the pixelated nature of the timing counter.

5.3.1 Expected Number of Hits

The pixelated timing counter (pTC) is the second part of the MEG II positron spectrometer. It is needed as the CDCH may have a good resolution in the position of the hits and thus in positron energy and direction but not in the time at which the positron arrived. Thus the time of the positron is measured with the pTC specifically designed for this purpose. Again, the number of expected hits for a good signal cluster is of great interest as it allows to reject background events with too few hits.

The expected number of hits is shown in Figure 5.10 for Mott and Michel events. Note that the positrons from Mott scattering have very similar properties as the signal positrons from the $\mu \to e\gamma$ decay. The positrons from Michel decay are the most dominant background in the positron spectrometer. Unlike the CDCH case, there is no clear separation between a good reconstructed cluster and an insufficient one. However, there is a small dip around 3 hits. This is used as a cut criterion for further studies on the MC data.

Further Mott and thus signal events have a larger number of pTC hits compared to background Michel events. This is due to the fact, that Mott events are just at the kinematic endpoint of the Michel spectrum. Thus a Mott positron has more energy and thus a larger radius than the average Michel positron. As the TC is constructed just to be on the outermost part of the spectrometer and thus of the track, this larger radius implies a longer path through the pTC and thus more pixels are crossed and potentially fired.

This pre-study does only consider the clusters matched in the pTC. Thus only the hits per cluster are recorded and not the total number of pTC hits per track. A track potentially can cross the TC twice or in rare cases even three times.

5.3.2 Reconstructed Positron Hit Time

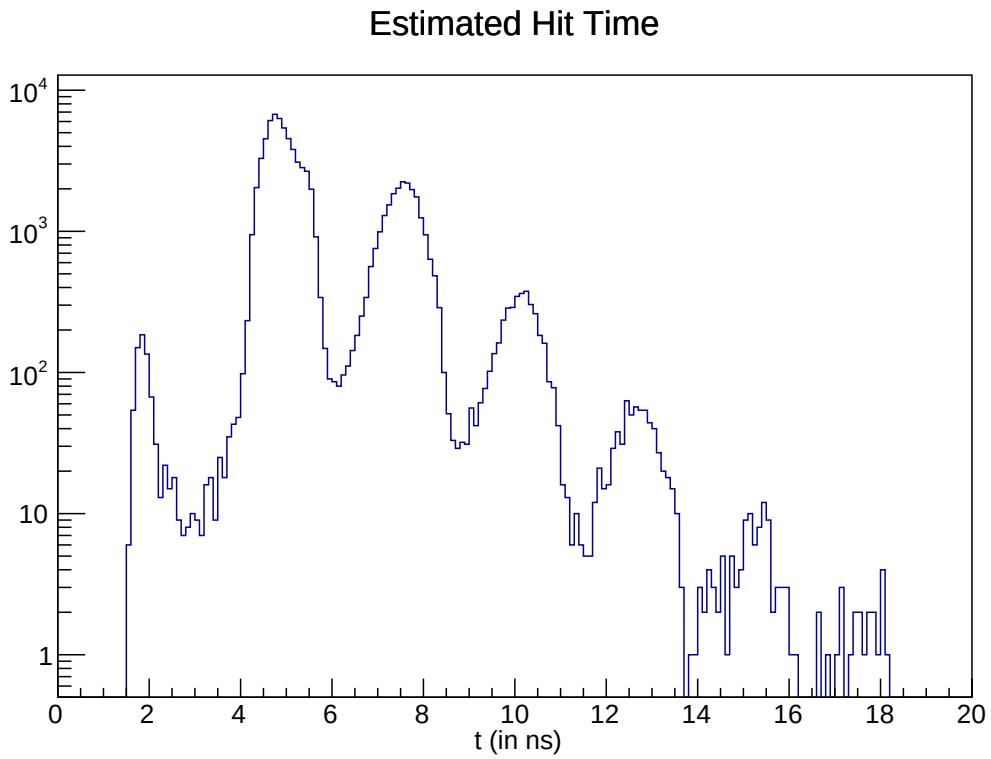

Figure 5.11: Estimated hit time of the clusters. These values are not yet corrected for the position of the cluster. The peaks for different amounts of turns in the spectrometer can be clearly distinguished. The first peak at 2 ns corresponds to half a turn from the centre directly to the TC. The second peak around 5 ns corresponds to one and a half turns etc.

For each of the clusters, the hit time is estimated as part of the analysing process. This time corresponds to the time it takes the positron to propagate from the target to the fired pTC cluster. The obtained results are shown in Figure 5.11. One can clearly distinguish individual peaks corresponding to a different number of turns before the pTC cluster was fired.

The first peak just below 2 ns marks the most direct way possible to get to the pTC. It corresponds to only a half turn in the spectrometer and a hit at the closest point to the target in the pTC. Its population is comparably low as only positrons with a limited point of scattering on the target and in the very right angle of emission can hit the pTC after just half a turn.

The second peak around 5 ns corresponds to one and a half turns through the spectrometer before the cluster was fired. This is the most populated state. For each further peak following after, the corresponding track contains an additional turn just before triggering the cluster. The separation of the peaks allows to approximate that it takes roughly $2 - 3$ ns for a complete turn. This corresponds to the expectation for a particle travelling near the speed of light along a track of the typical curvature expected for MEG II.

A further observation about the second peak is that it appears to have a bump just about half a nanosecond later. It can be explained by a small discrepancy between different locations in the TC. This is the first hint to a strong dependence of the estimated hit time on the position of said hit.

The detailed behaviour of the reconstructed hit time in dependence of the position z along the beam axis is shown in Figure 5.12. As above one can clearly separate between clusters fired after

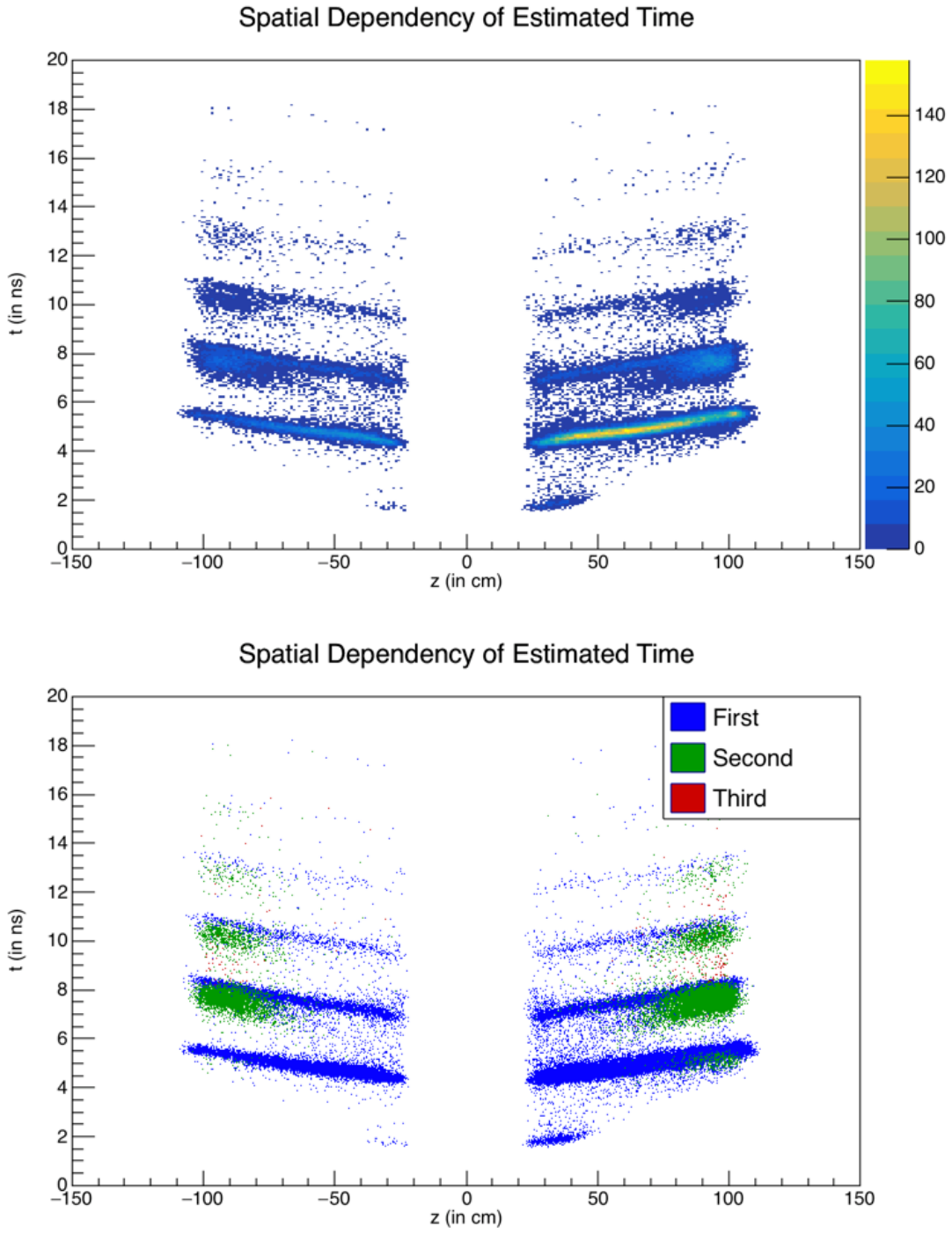

Figure 5.12: Estimated time plotted versus the position of the first hit in the cluster along the beam axis. Positive z-Values represent DS, negative Values stand for the US. The target is placed at $z = 0\,\text{cm}$. With increasing distance from the target, the cluster is fired later as the positron needs to propagate a longer distance. Further, one can clearly distinguish the numbers of turns a track took before firing a cluster, starting from half a turn on the bottom. From the lower plot it becomes visible that the second cluster of a track appears just a little earlier than a first cluster of a track with similar properties and with a larger uncertainty in time.

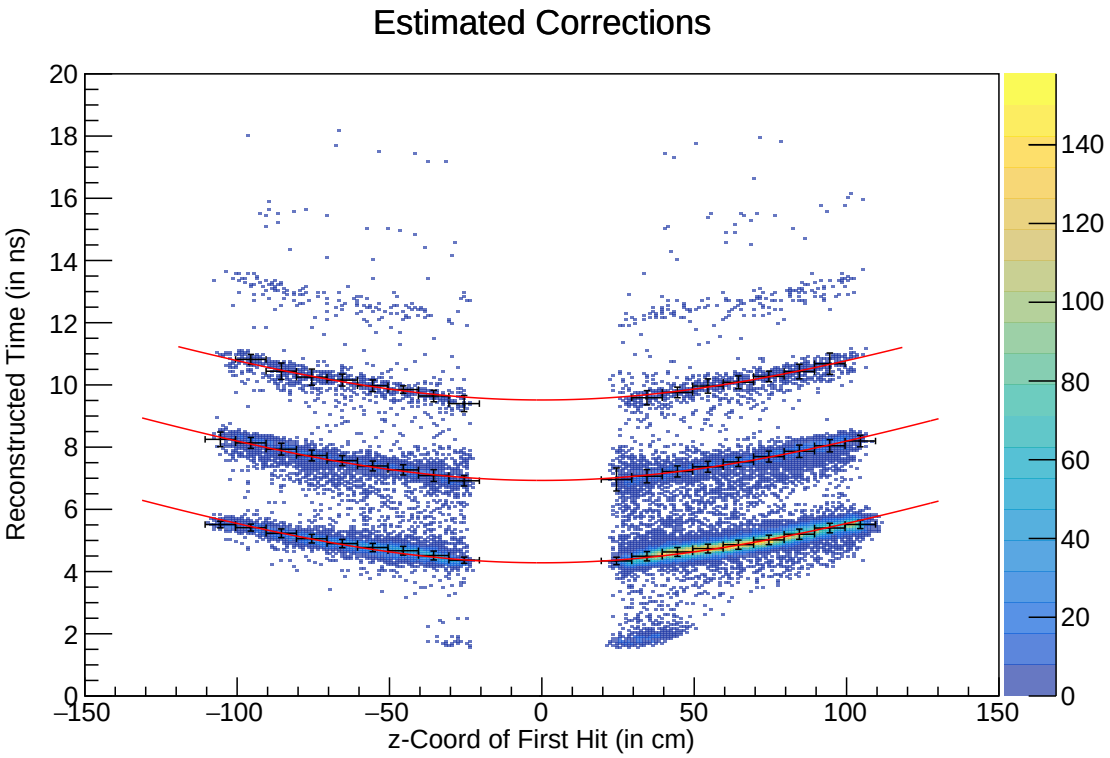

Figure 5.13: By fitting the time spectra for segments with individual Gaussians, the mean value and standard deviation is estimated for local positions (black). The lowest one is fitted with the formula 5.8 and then shifted by a constant factor to match the other ones. The corrections at any location are then estimated as the difference between the minimum value of the curve and the local value of the curve.

half a turn, one and a half turns etc. Each accumulation shows an increased time with an increased distance from the centre. This comes naturally as with an increased distance from the centre, the path from the vertex to the pixel increases as well. The longer the path is, the longer the positron takes to travel to that pixel as all of them are in the highly relativistic regime.

Another interesting feature is highlighted in the second plot. The recorded clusters have been sorted according to their number on the track. The first fired by a positron is marked in blue. Some tracks hit the TC once more after an additional turn. These second clusters on a track are colored in green. They appear towards the outside of the detector and appear just a little earlier than the first hits at the same location (in blue).

To explain this effect, one needs to consider the happenings during the first fired cluster. As can be seen in Figure 5.10, a cluster consists of 5 to 12 or even more hits. On average, each hit is linked to an energy deposit of around 1 MeV. Accumulated this results in an energy deposit of 5 MeV to 12 MeV. This corresponds to 10 % to 20 % of the total energy of the highly relativistic positron.

Thus, by passing through the TC, the positron loses 10 % to 20 % of its total momentum yet remains highly relativistic. Assuming a constant magnetic field leads to a reduction of the radius of the trajectory by the same factor. As the velocity of the positron hardly changes but the path length for the following turn is reduced, the next full turn is completed faster by roughly 10 % to 20 % with respect to an unaltered turn. This matches roughly with the observation in Figure 5.12. Furthermore, this serves as explanation for the larger spread of the second clusters.

On a really rare occasion, there is even a third cluster fired by the same positron track. These are marked in red in the lower plot. They appear only in the outermost area of the TC as at least two clusters have to appear further inside. They are even further spread out in time as these tracks already passed twice through the TC and thus a larger spread is introduced.

In order to estimate the timing resolution of the TC, it is best to rely only on the first hit cluster

Uncorrected

	μ_1 in ns	σ_1 in ns	μ_2 in ns	σ_2 in ns	μ_3 in ns	σ_3 in ns	μ_4 in ns	σ_4 in ns
First	4.906(2)	0.3407(11)	7.506(5)	0.444(3)	10.106(11)	0.440(7)	12.71(3)	0.46(2)
Second	5.048(11)	0.222(9)	7.527(4)	0.335(3)	10.095(10)	0.342(7)	12.63(3)	0.38(3)

Corrected

	μ_1 in ns	σ_1 in ns	μ_2 in ns	σ_2 in ns	μ_3 in ns	σ_3 in ns	μ_4 in ns	σ_4 in ns
First	4.2963(6)	0.1481(5)	6.939(2)	0.186(2)	9.484(7)	0.237(7)	12.05(2)	0.23(2)
Second	3.929(12)	0.241(9)	6.466(3)	0.314(3)	9.051(8)	0.312(7)	11.58(2)	0.30(2)

Table 5.4: Time resolutions of the timing counter extracted from the fits shown in Figure 5.14. The upper two rows contain the results for the uncorrected data displayed in the upper diagram and the lower rows show the results obtained after the correction has been applied.

marked in blue as they have the least intrinsic uncertainties. Further, as there is a clear dependency between the time a cluster is fired and the position of that cluster, a correction based on the first hit clusters can be calculated and applied to get an overall time resolution for the timing counter.

For this purpose, the TC was split into several slices of 10 cm thickness and the time spectra has been fitted with three individual Gaussians in the range from 4 ns to 11.5 ns. The obtained values are plotted in black in Figure 5.13. The width of the slice is assumed as error in the horizontal direction and the standard deviation of the fitted Gaussian as the error in vertical direction.

The graph obtained for the lowest peak corresponding to one and a half turns is first fitted with a function modelling the time required for a helical trajectory. It is given by the formula

$$t(z) = \frac{1}{v}\sqrt{l_p^2 + z^2} \tag{5.8}$$

where v stands for the speed of the positron and l_p stands for the length of the track perpendicular to the beam axis. The values obtained by the fit are $v = (29.7 \pm 1.4)\,\mathrm{cm/ns}$ and $l_p = (129 \pm 8)\,\mathrm{cm}$. These values match perfectly with the expectations.

Although the same assumption matches the other graphs as well, those results are without meaning as the bending radius increases as the track propagates through the detector. For these, an additional constant shift is assumed on top of Equation 5.8 for the additional turn. This has the advantage that the correction can be calculated only from the position along the beam line (z-coordinate) and does not require a separate treatment for the individual turns. The final functions fitted to each of the graphs are shown in Figure 5.13.

By applying the spatial corrections to the time spectra, one obtains the new, corrected spectra in Figure 5.14. Note that the spectra have been drawn individually for the first and the second registered cluster. The first thing to observe is that the blue peaks representing the first cluster are clearly narrower than one would estimate without the corrections.

Further, the green peaks of second clusters are shifted to the left and did not get narrower on a similar scale. This is due to the fact that the green clusters appear only at a larger distance from the centre. This implies on the one hand that large corrections are subtracted shifting them to the left. On the other hand, their lower spread along the beam axis leads to small differences in the corrections and thus the effect cannot be as visible as for the blue clusters.

The four most dominant peaks between 3 ns and 14 ns are fitted with the sum of four Gaussians. The fits themselves are shown in Figure 5.14 and their results are listed in Table 5.4. The most notable result was a time resolution of $(148.1 \pm 0.5)\,\mathrm{ps}$ for the most dominant peak at 4 ns. This peak represents roughly two thirds of all events in the pTC.

Over all the peaks fitted for the first recorded clusters the time resolution is improved by roughly a factor of two. For the second cluster, the obtained values get slightly reduced yet not significantly as their spread is not determined by the spatial deviations of the TC. Whereas in the uncorrected case the time resolution of the second cluster was better, the first cluster offers a better resolution in time once the corrections are applied.

From the mean values of the different peaks, one can see that the peaks are separated by approximately 2.5 ns. This value holds for both - the first and the second recorded clusters and thus implies that this is the time needed for a theoretical full turn perpendicular to the beam axis. A real full turn needs slightly longer as it propagates along the z-Axis as well.

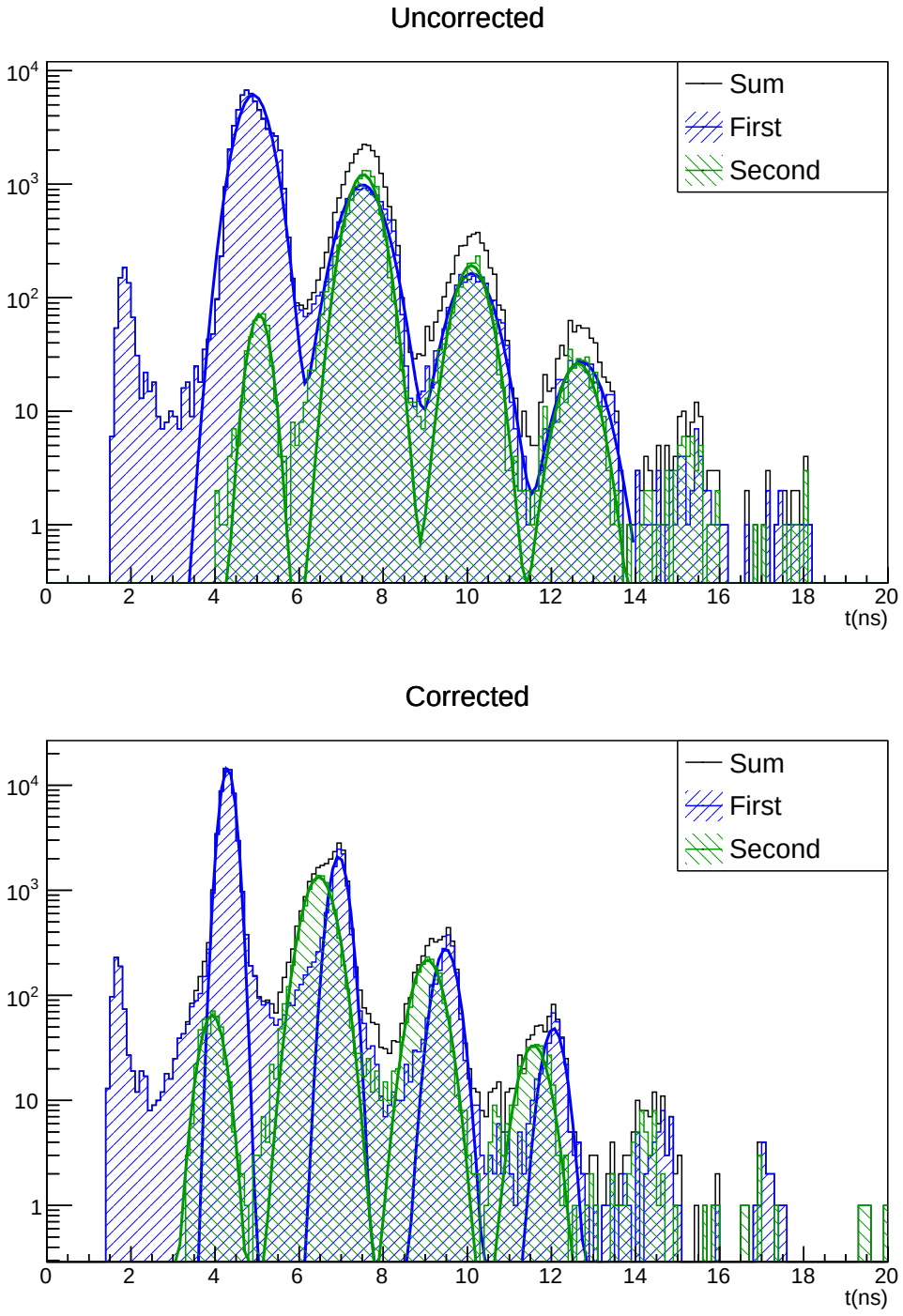

Figure 5.14: The extracted hit time before and after the corrections are applied. The clusters are separated into first (blue) and second (green) cluster along the track. The four most dominant peaks are fitted with a Gaussian. The results can be found in Table 5.4. After the corrections are applied, a resolution of (148.1 ± 0.5) ps can be extracted for the most dominant peak (two thirds of the events).

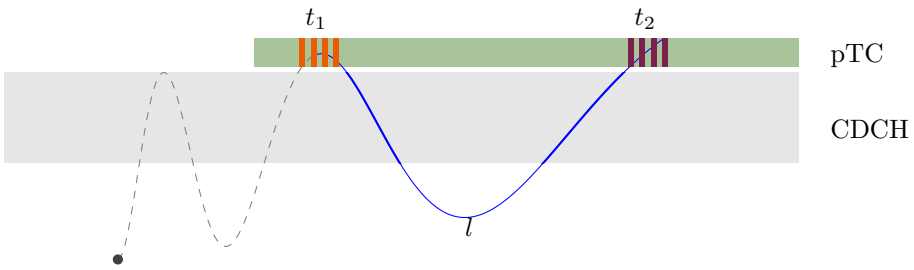

Figure 5.15: Basic principle of the double-cluster method. A track with two pTC clusters is chosen. The timing information (t_1, t_2) is extracted from both and their difference compared to the expected time of flight $t_{\text{tof}} = l/c$ between the clusters.

5.3.3 The Double-Cluster Track Method

Based on the same idea as for the double-turn track method for the drift chamber described above in Section 5.2.3, the double-cluster track method can be used to gain insight on the intrinsic time resolution of the timing counter (pTC). Instead of two matching partial tracks (turns), one is looking for two pTC clusters that are connected by a track and thus origin from the same positron.

The basic principle is depicted in Figure 5.15. For both clusters the hit times (t_1, t_2) are extracted. In the ideal case the difference $\Delta t = t_2 - t_1$ between the two times should be equal to the time of flight t_{tof} between the two clusters. Any deviation is then due to uncertainties in the reconstruction of the variables.

For this reason a proper way to estimate the time of flight has to be developed. Therefore the track information obtained by the CDCH is used. All wire hits associated to the track between the two clusters are considered and fitted with a helix. Despite the fact, that the magnetic field is inhomogeneous, this approximation fits well as can be seen in Figure 5.16.

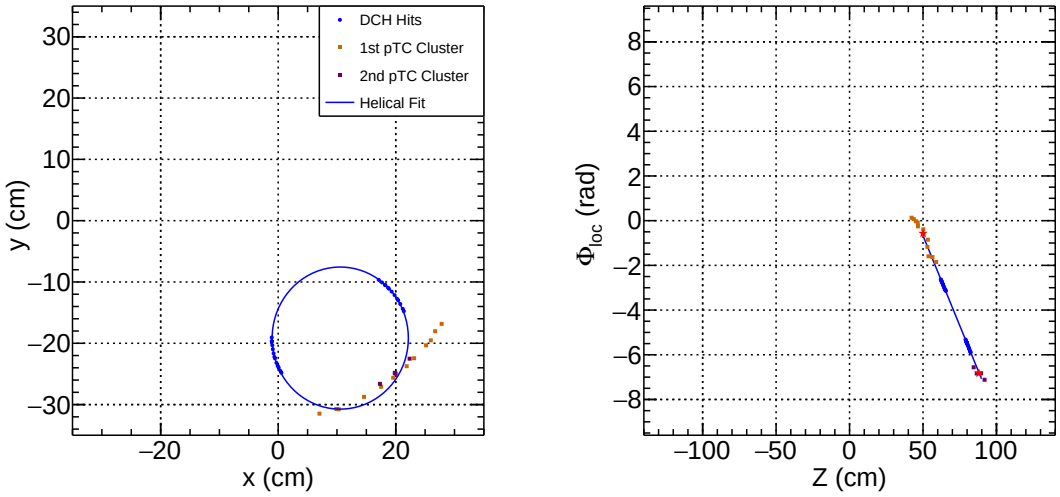

Figure 5.16: Helical approximation of the track. The left figure shows the xy plane perpendicular to the beam axis. In this perspective, the helix is seen as a circle that describes the drift chamber data points (blue) rather well. The track moves in clockwise direction and connects to the first cluster (orange) at around ($x = 10\,\text{cm}$, $y = -30\,\text{cm}$) and to the second cluster at around ($x = 23\,\text{cm}$, $y = -23\,\text{cm}$). The right figure shows the same data points in the z, Φ_{loc} frame. The z-Axis points along the beam axis and the axis of the helix. The angle Φ_{loc} is measured with respect to the axis of the helix corresponding to the center of the circle depicted in the left figure. In this frame all data points line up on a straight line described by the helix.

The blue points in Figure 5.16 represent the data points obtained from the CDCH. They are first fitted with a circle in the xy plane as depicted on the left side. This matches the data from the drift chamber rather well. Based on this circle, a new reference frame in cylindrical coordinates with its origin in the circle's centre is considered. This frame is later used for the figure on the right, where the CDCH data is now fitted with a straight line.

The data points obtained from the pTC deviate in the xy plane for two reasons. First, the pTC data has no radial information associated apart from the tile's position. Second, the positron looses energy on its way through the timing counter and the radius is decreased. For the clockwise track in Figure 5.16 the second reason explains the hits in the first cluster (orange) far off the fitted track and the first reason explains the different curvature observed.

As can be seen on the right side, there is hardly any discrepancy observed neither in the longitudinal z-direction nor in the local angular Φ_{loc} direction. The data points obtained from the pTC align rather well with the line defined by the CDCH data. The respective centres are used to estimate the cluster's position in terms of z and Φ_{loc}.

The path length l of the track between the clusters is now calculated based on the differences of Δz and $\Delta\Phi_{\text{loc}}$ obtained by the clusters themselves and the radius r of the circle obtained by the drift chamber data as

$$l = \sqrt{(r\Delta\Phi_{\text{loc}})^2 + (\Delta z)^2}. \tag{5.9}$$

Although the positron looses some of its energy in the pTC, it remains highly relativistic and its speed can be approximated by the speed of light. Even assuming that the positron's energy drops down to 20 MeV, this approximation yields an error of around 1 ps for reasonable track lengths. A similar deviation is obtained by an error in the estimated path length in the sub-millimetre range. This yields

$$t_{\text{tof}} = \frac{l}{c} = \frac{1}{c}\sqrt{(r\Delta\Phi_{\text{loc}})^2 + (\Delta z)^2} \tag{5.10}$$

for the time of flight.

Comparing the time difference between the two pTC clusters to the calculated time of flight yields information about the intrinsic positron time resolution of the detector. The obtained distributions are shown in Figure 5.17 for Mott, Michel and signal events. Each distribution has an equal number of initial events.

As only positrons emitted under a certain angle are able to fire two separate clusters in the pTC, there are more entries in the distribution for signal events compared to Mott. In addition positrons of lower energies may not be able to fire two clusters due to their smaller bending radius. This explains the clearly lower amount of Michel events compared to the other two kinds.

Each distribution is fitted by the sum of two Gaussians to take care of the tails on both sides. The fit results are given in the lower part of Figure 5.17. The results obtained for signal and Mott events are very well consistent with each other. A standard deviation of around 50 ps is suggested for each of the two. Michel events seem to be slightly off, yet their low statistics denies a conclusive result.

Assuming that the deviations between time of flight and cluster time difference originate mainly from the time difference, one concludes that the intrinsic positron time resolution of the pTC is around or below 40 ps for the abundant cluster types. This agrees very well with the results obtained by other methods [89].

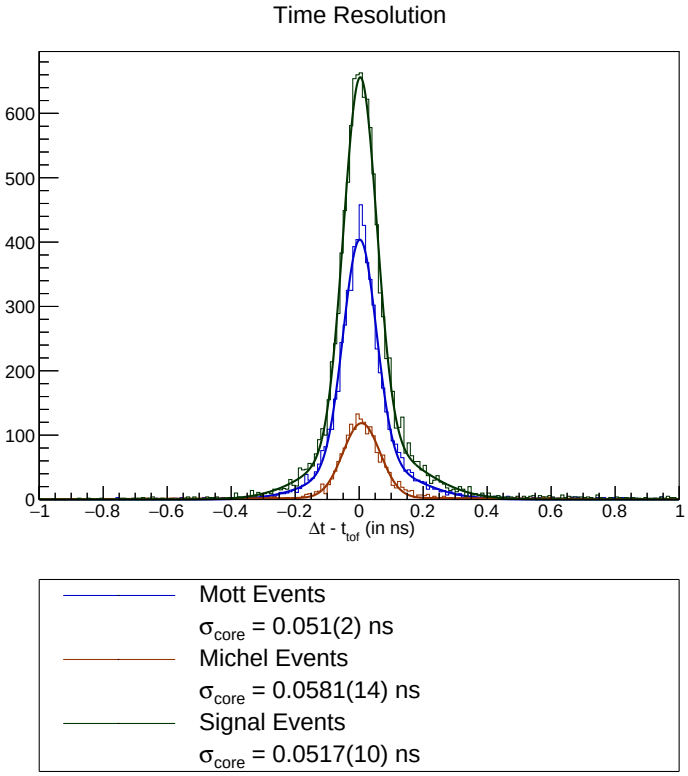

Figure 5.17: Obtained deviations of the difference between the times obtained by the cluster from the obtained time of flight.

Chapter 6

Calibration of the Radiative Decay Counter

This chapter contains simulations for what was considered a possible new calibration method of the downstream Radiative Decay Counter (RDC) based on a positron beam. It was later abandoned as the benefits do not justify the efforts.

6.1 Simulation of a Low Momentum Positron Beam for RDC

In order for the RDC to work properly, two calibrations are needed. First there is a need to calibrate the matching between plastic scintillators for the timing and the LYSO crystals for the energy deposit. Second, the LYSO crystals need to be calibrated amongst each other to determine the total energy deposit in all crystals together. Only once both calibrations are performed, one can effectively detect low energy positrons coinciding in time with a XEC signal and thus reject it as RMD event.

The use of a positron beam of low momentum around 28 MeV offers the possibility to do both calibrations simultaneously. In addition it offers the advantage of providing positrons in the same energy regime as the expected positrons from RMD that just did not make it to the CDCH. For this purpose, the standard muon beam needs to be switched to positrons and adjusted in such a way that the entire crystal gets illuminated.

Different beam configurations have been tested and the distribution of RDC hits has been analysed. The configuration refers to the beam properties at the centre of COBRA. The spatial distributions for the four most promising settings are shown in Figure 6.1. For each configuration the same amount of MC events was generated yet not all of the events resulted in a hit on the RDC.

For the first setting displayed on the top left with COBRA switched on and a beam width of 7 mm most of the positrons hit in the central region of the RDC despite the comparably large divergence. This effect is due to the fact that the distance between the COBRA centre and the RDC is just a multiple of the z-distance of a turn for the most divergent positrons. Thus these positrons start to fly away from the beam axis yet due to the magnetic field, they get curved back to the z-Axis and end up hitting the RDC in the central region.

By increasing the width of the incoming beam (top right), the events get distributed better over the entire detector. Yet still the outermost regions get considerably fewer hits. They get significantly more hits if one switches the magnetic field off and stays within a beam width of 7 mm as displayed on the bottom left. Due to the large divergence a majority of the events miss the RDC as the positron tracks don't get curved back to the z-Axis due to the missing magnetic field. The rest of the hits are distributed more or less uniformly over the RDC.

The best results are obtained by switching COBRA off and aiming for a low beam width (7 mm) and a common beam spread of 30 mrad as displayed on the bottom right. As the positron tracks don't get curved back, this small divergence is enough to cover the entire RDC. Yet due to the lower divergence, significantly more tracks hit the RDC. This leads to an increase in the event rate for all of the crystals, but especially for the ones in the centre. For further evaluations, only this setting is considered.

For each of the LYSO crystals the simulated energy deposit is estimated. The obtained spectrum is fitted with a gauss like function with extended tails as given by the equation

$$f(E) = \begin{cases} Ne^{-\frac{1}{2}\frac{(E-\mu)^2}{(\sigma_1+(E-\mu)\sigma_2+(E-\mu)^2\sigma_3)^2}} & E \leq \mu \\ Ne^{-\frac{1}{2}\frac{(E-\mu)^2}{(\sigma_1+(E-\mu)\sigma_2)^2}} & E > \mu \end{cases} \tag{6.1}$$

with the fitting parameters for the peak height N, the mean μ and the standard-deviation-like parameters σ_1, σ_2 and σ_3. For a selected set of crystals the spectra are shown in Figure 6.2 and the results of the corresponding fit are listed in Table 6.1.

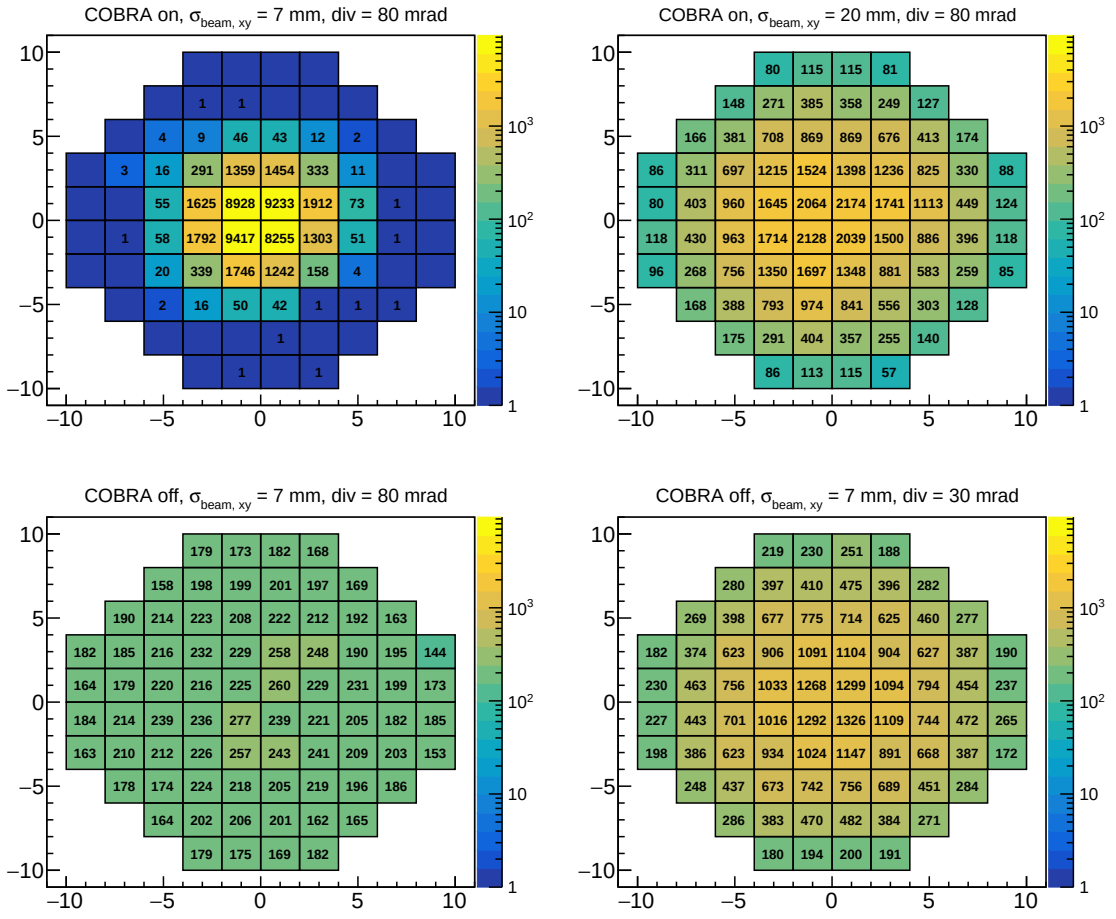

Figure 6.1: The hit distribution on the RDC for different beam configurations at the COBRA centre.

Comparing the obtained results from the different crystals, one can see that the high energy part of the different spectra is rather independent of the crystals position. The only large difference observed is the number of recorded hits as the beam positrons are more likely to hit the centre. The differences in the fitted means μ are well within the expectations based on their estimated uncertainties. Thus this method would suit well to check the calibrations of the crystals amongst each other for the expected positron energy.

One potential concern is the radiation damage done to the RDC by pointing a low momentum positron beam directly at it. However, the amount of positrons needed for this calibration is low compared to the amount of expected Michel positrons collected during the main physics run or the positrons scattered at very low angle from the Mott calibration of the MEG II spectrometer. Thus the damage due to this calibration method should not exceed the already expected radiation damage.

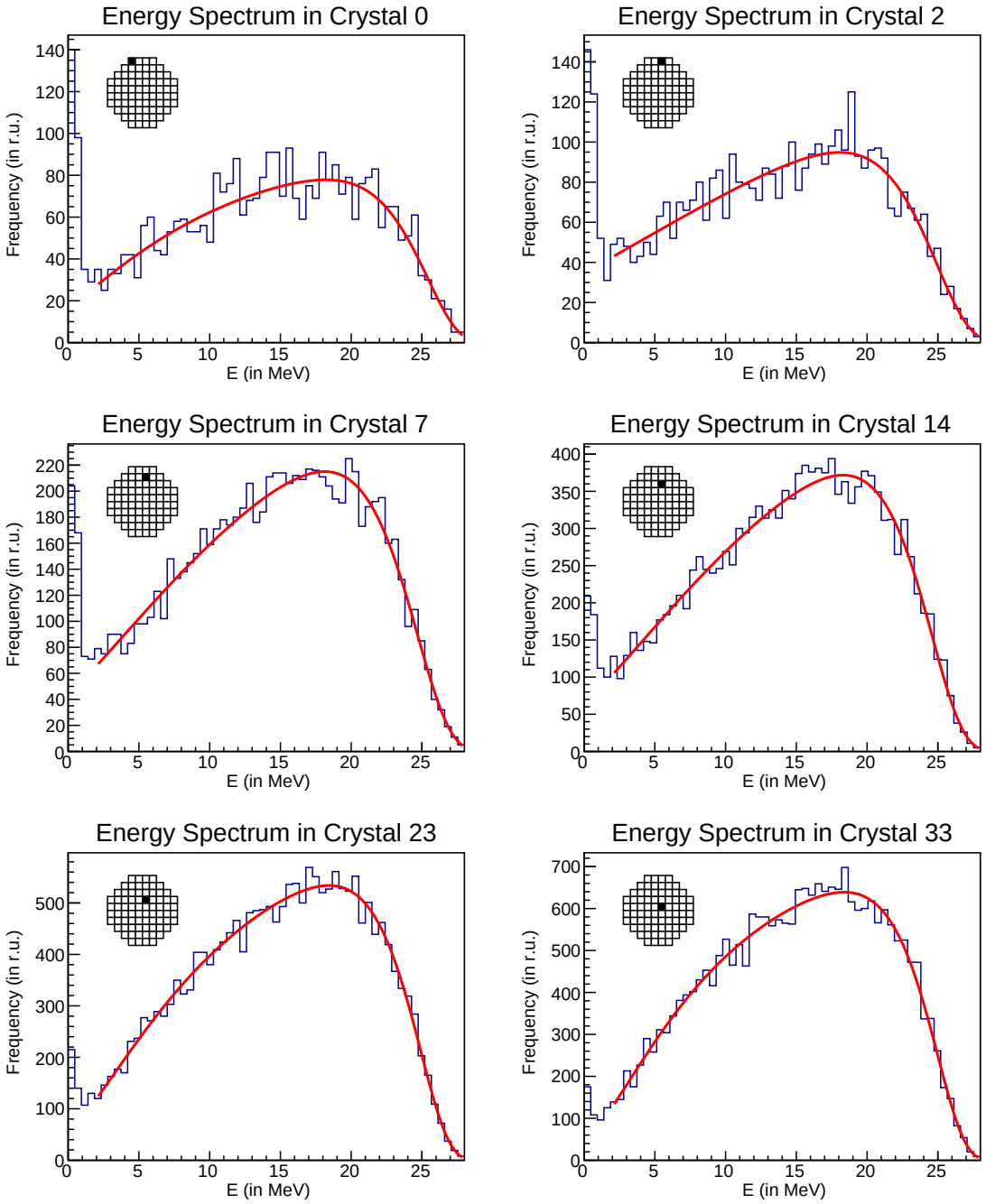

Figure 6.2: The energy deposit in different crystals. Only events have been selected where said crystal was the first to be hit by the incoming particle.

Crystal	Number of Hits	μ MeV	σ_1 MeV	σ_2	σ_3 1/MeV
0	3519	18.2 ± 0.4	9.5 ± 0.8	-0.58 ± 0.10	-0.030 ± 0.010
2	4190	18.1 ± 0.3	8.5 ± 0.8	-0.48 ± 0.08	-0.014 ± 0.009
7	8638	18.1 ± 0.2	8.0 ± 0.4	-0.46 ± 0.04	-0.019 ± 0.004
14	14377	18.30 ± 0.14	7.8 ± 0.3	-0.48 ± 0.03	-0.020 ± 0.003
23	20606	18.44 ± 0.13	8.4 ± 0.2	-0.56 ± 0.03	-0.030 ± 0.003
33	24639	18.38 ± 0.12	8.8 ± 0.2	-0.60 ± 0.03	-0.035 ± 0.003

Table 6.1: The obtained parameters from fitting the spectra of different crystals shown in Figure 6.2.

Chapter 7

Upgrade of the CEX Auxiliary Detector

In this chapter, new scintillating materials for future calorimeters are studied extensively. The simulations are used to decide on a first prototype to be used as upgraded CEX auxiliary detector. Moreover, the benefits of larger crystals are considered with the idea to use them in calorimeters of future high precision experiments. The most important results were published in [90, 91, 92].

As described in Section 3.2.7.2, an auxiliary detector is used for the charge exchange (CEX) calibration. Its main purpose is to assert time coincidence and back to back geometry of two γs from a π^0 decay and thus select photons at the kinematic endpoints at 55 MeV and 83 MeV.

From this point of view, it is not mandatory to use an auxiliary detector with ultra-precise time resolution and supreme energy resolution, yet it offers the opportunity to test new materials and technologies that may soon become viable candidates for future experiments.

Two very promising materials on the market are BrilLanCe (cerium doped lanthanum bromide, $LaBr_3$(Ce)) and LYSO (Lutetium Yttrium OxyorthoSilicate, $Lu_{2(1-x)}Y_{2x}SiO_5$(Ce)). Their main features are listed in Table 7.1.

Cerium doped lanthanum bromide stands out due to its ultra-high light yield (1.65 $\times$ NaI(Tl)) and a by an order of magnitude faster decay time compared to NaI(Tl). With these properties $LaBr_3$(Ce) performs well at low energies $\mathcal{O}$(1 MeV), limited by the size of the available crystals.

Due to recent developments, larger crystals up to a diameter of 8.9 cm and a length of 20.3 cm may be produced commercially. A calorimeter built from such a large crystal is an eligible candidate for the detection of γs at higher energies $\mathcal{O}$(50 MeV). This corresponds to the signal energy of current cLFV experiments. Thus $LaBr_3$(Ce) may be a suitable candidate for future experiments in this sector.

LYSO on the other hand exhibits a very high density comparable to BGO and thus features short radiation length and Molière radius. Despite the fact that its LY is only roughly 70 % of NaI and the decay time roughly three times longer compared to $LaBr_3$(Ce), its density makes LYSO a possible candidate - especially considering that the available crystal size is one of the limiting factors.

These already exciting features can be improved even further by coupling the crystals to state of the art Multi-Pixel Photon Counters (MPPCs). Due to their small thickness of a few mm, a double-readout is possible: A custom MPPC array is placed on the front side and one on the back side of the crystal. This configuration improves the detection efficiency of the scintillation photons with minimal impact on the energy loss while passing through the front readout. Independent of the chosen crystal a lot of light will be generated. To keep saturation effects at a minimum, the smallest available pixel size for the MPPCs is considered.

In addition, the granularity due to the MPPCs allows some geometrical reconstruction of the event. This allows to identify and remove events close to the crystal's lateral surface where energy leakage is common and thus the resolution worse. On the other hand, the number of Data AcQuisition (DAQ) channels has to stay within a reasonable amount. A trade-off between number of DAQ channels and granularity is made by choosing MPPCs with an active area of 6 mm $\times$ 6 mm.

Material	Density ρ (g/cm^3)	Light Yield LY (ph/keV)	Decay Time τ (ns)	Radiation Length X_0 (cm)
$LaBr_3(Ce)$	5.08 [1]	63 [1]	16 [1]	2.1 [2]
LYSO	7.1 [3]	29 [3]	41 [3]	1.21 [4]
LXe	2.95 [5]	40 [6]	45 [6]	2.9 [5]
NaI(Tl)	3.67	38	245	2.59
BGO	7.13	9	300	1.12

Table 7.1: Properties of commonly used scintillators. The information was taken from Review of Particle Physics ([93]) unless specified otherwise:
[1] Manufacturer's Datasheet [94] [2] Private Communication [95] [3] Manufacturer's Datasheet [96]
[4] Geant4 based estimate [5] PDG Online [97] [6] MEG II values for XEC

MPPC	Size (mm^2)	Active Area (mm^2)	Number of Pixels	Fill Factor (%)	PDE (%)
Hamamatsu S13360-6025PE	7.35×6.85	6.0×6.0	57 600	47	25
sensL MicroFJ-60035TSV	6.13×6.13	6.07×6.07	22 292	75	38 to 50

Table 7.2: Comparison of the SiPMs. Data is taken from corresponding data sheets [98, 99].

For further studies, two different MPPC candidates by different manufacturers are considered. The first candidate is the type S13360-6025PE manufactured by Hamamatsu [98]. It features 57 600 pixels with a total size of 25 µm × 25 µm each.

The second candidate is the type MicroFJ-60035TSV by sensL [99]. It features a lower number of pixels (22 292) with an active size of 35 µm × 35 µm each. However, it has a significantly increased fill factor and a smaller support structure enhancing the overall coverage and photodetection efficiency (PDE). An extensive comparison is given in Table 7.2.

The simulations are based on the GEANT4 libraries [87] with dedicated code to take care of the SiPM's responses. For each pixel, the dead time and the quantum efficiency is considered. Dark current and crosstalk are not implemented. For each side, the SiPM that detected the most photons is selected. For this SiPM and its neighbours, the waveform is generated and stored separately for analysis.

Unless stated otherwise a photon of 55 MeV hitting the centre of the crystal is simulated. Further SiPMs based on the type S13360-6025PE manufactured by Hamamatsu are implemented if not stated otherwise. The histograms representing the number of detected photons are fitted by a tailed Gaussian function given by

$$f(x|N,\mu,\sigma_1,\sigma_2,\sigma_3) = \begin{cases} N\exp\left(-\frac{(x-\mu)^2}{2(\sigma_1)^2}\right) & \text{if } x > \mu \\ N\exp\left(-\frac{(x-\mu)^2}{2(\sigma_1+\sigma_2(x-\mu)+\sigma_3(x-\mu)^2)^2}\right) & \text{if } x < \mu \end{cases} \tag{7.1}$$

using five parameters for fitting. This function looks like an ordinary Gaussian from the upper side ($x > \mu$) and has a tail on the other side. The resolutions quoted always refer to the ratio given by σ_1/μ.

In a first step, the effect of the double-readout is investigated. Therefore, a lanthanum bromide crystal with a diameter of 8.89 cm and a length of 20.32 cm is considered. Separate runs were performed for a back-only, a front-only and a double readout scheme. The results are shown in Figure 7.2.

On the left side in Figure 7.2a the total amount of energy deposited in the crystal is shown. These numbers are directly extracted from the simulation. Independently of the readout scheme,no difference could be observed. This confirms the hypothesis on a simulation level, that SiPMs on the front face don't have any significant effect in terms of energy loss.

When considering the total number of detected photons, the advantage of the SiPMs in the front-readout scheme becomes clear. Using only a readout on the front face, the number of detected photons increase and the resolution changes from (7.76 ± 0.15) % (back-readout) to (5.63 ± 0.12) %

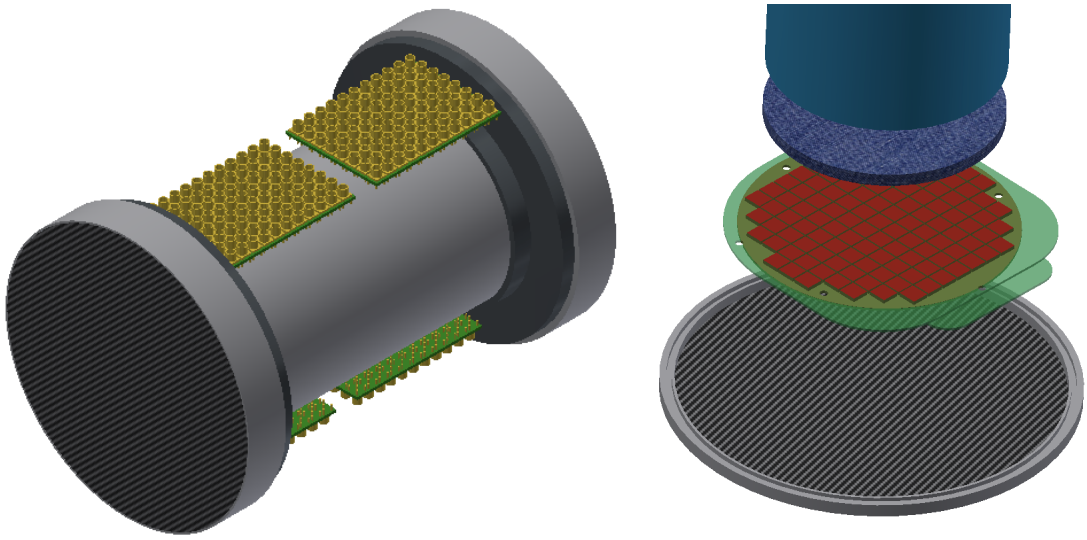

(a) total view (b) readout view

Figure 7.1: Constructional drawing of the Prototype. Published in [90]. The crystal is coated with aluminum on the lateral sides and sealed with quartz windows on the faces. MPPCs (in red) are attached to each of the faces as seen on the right. The support structure (green) contains all the electrical connections needed for the SiPMs. To seal the entire prototype, carbon fibre structures are placed on each face.

(front-readout). A resolution of $(2.25 \pm 0.07)\,\%$ is estimated for a double-readout scheme as shown by the green line in Figure 7.2b. Based on these preliminary results, only double readouts are considered for all the following configurations.

7.1 Expected Energy Resolution

This section presents the first set of studies of LYSO and BrilLanCe crystals including the obtained energy deposit and number of collected photons. The expected energy resolution is extracted from the number of photons collected in each configuration.

The energy deposit and number of detected photons were estimated based on MC simulations for several different geometrical configurations. For lanthanum bromide crystals of different radii ranging from 4.45 cm to 7.62 cm, the results are shown in Figure 7.3.

For the currently available size with radius 4.45 cm and length 20.32 cm, significant leakage effects occur as seen on the left side (Figure 7.3a). This is not surprising as the crystal radius (4.45 cm) is just about twice the Molière radius ($R_M \approx 2.3\,\text{cm}$) [95]. As a result, leakage effects are limiting the achievable energy resolution to roughly $(2.36 \pm 0.08)\,\%$ as estimated by the number of detected photons.

By increasing the radius of the crystal, the performance in terms of energy deposit is clearly increased. As a result, the resolution improves to $(1.23 \pm 0.04)\,\%$ for a crystal of radius $R = 6.35\,\text{cm}$ and to $(0.96 \pm 0.03)\,\%$ for a crystal of radius $R = 7.62\,\text{cm}$. Later radius corresponds to roughly three times the Molière radius of lanthanum bromide. Unfortunately, crystals of that size are not yet available.

Further an increase in crystal length from 20.32 cm to 22.86 cm has been studied for crystals with a radius of 7.62 cm. The results are shown in Figure 7.3 as well. There is no significant difference observable neither in terms of energy deposit nor in terms of collected photons. This is expected as the crystals are already roughly ten times longer than the radiation length ($X_0 \approx 2.13\,\text{cm}$).

As the currently available size of the crystal is a limiting factor to the resolution achievable with the prototypes, LYSO becomes an eligible candidate due to the higher density and thus shorter radiation length ($X_0 = 1.21\,\text{cm}$). As can be seen in Figure 7.4, the available LYSO crystal

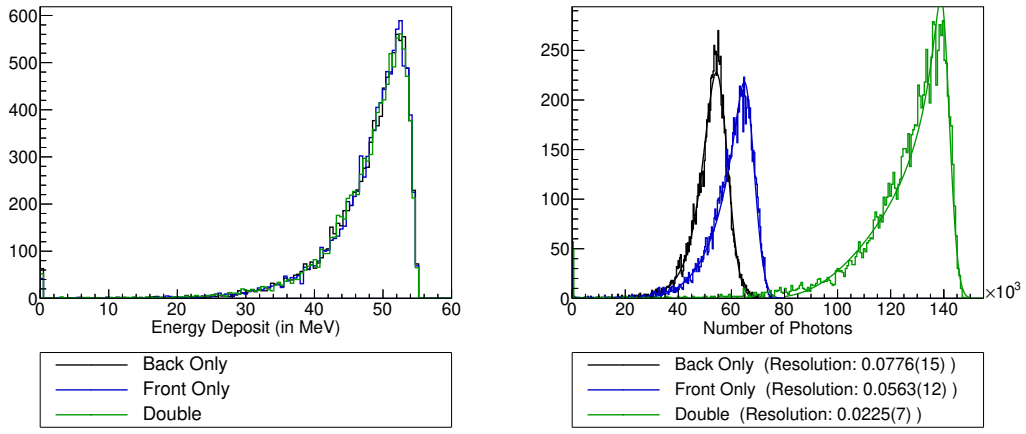

(a) Energy Deposit: unaffected

(b) Number of Photons: affected

Figure 7.2: Different readout schemes based on S13360-6025PE Type MPPC for a $LaBr_3(Ce)$ crystal (8.89 cm diameter, 20.32 cm length). Back Only refers to a SiPM readout on the back and the front face closed with a thin layer of aluminium. Front only to the situation with a SiPM readout on the front and an aluminium layer on the back. Double is characterised by a SiPM readout on both sides.

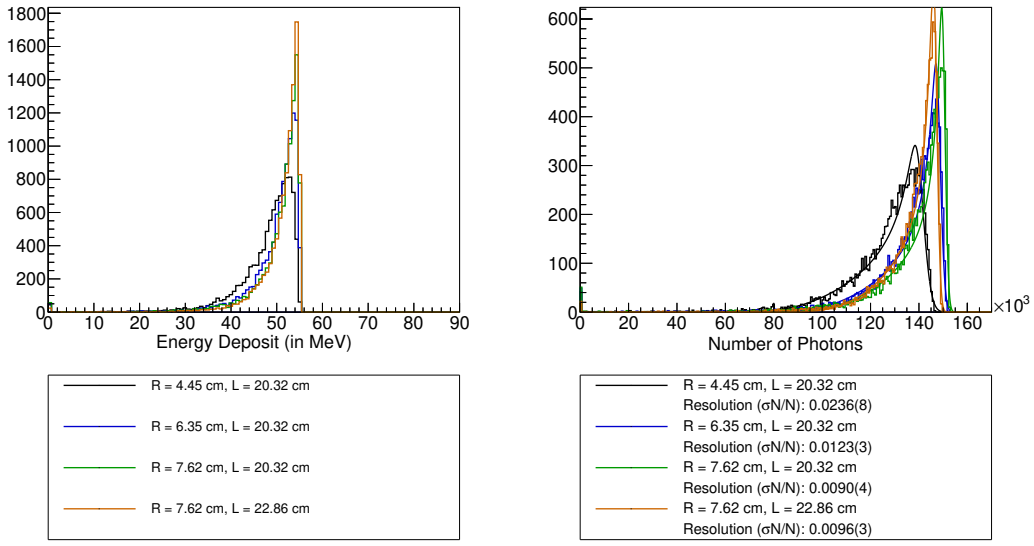

(a) Energy Deposit

(b) Number of Photons

Figure 7.3: Energy deposit and number of detected photons for Cerium doped Lanthanum Bromide crystals of different sizes. The currently available size is ($R = 4.45\,\text{cm}, L = 20.32\,\text{cm}$). The larger crystals are of hypothetical nature to investigate the change of performance.

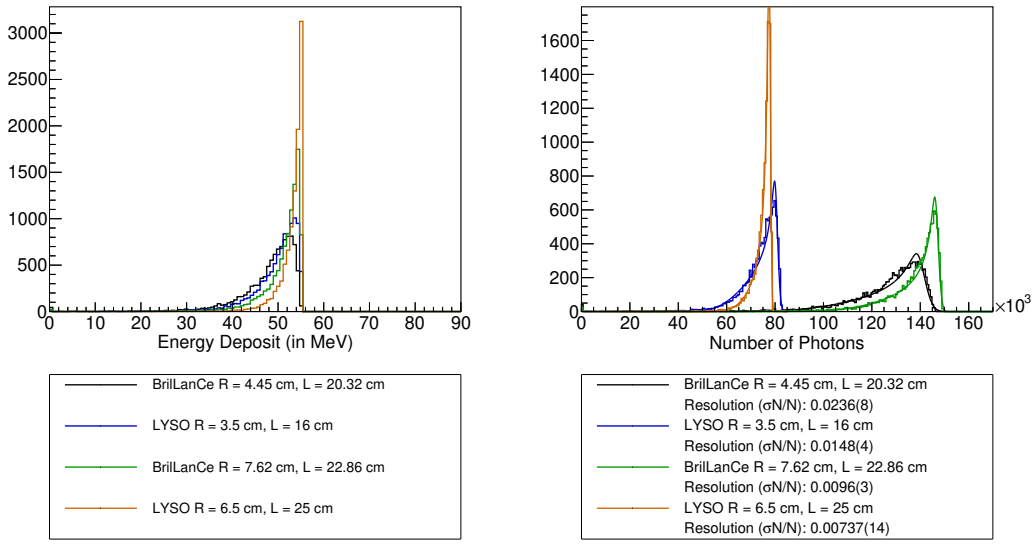

(a) Energy Deposit

(b) Number of Photons

Figure 7.4: Comparing the available BrilLanCe crystal ($R = 4.45\,\text{cm}$, $L = 20.32\,\text{cm}$) to the available LYSO crystal ($R = 3.5\,\text{cm}$, $L = 16\,\text{cm}$) as well as larger crystals of both materials.

($R = 3.5\,\text{cm}$, $L = 16\,\text{cm}$) performs better in terms of energy deposit compared to the largest available $LaBr_3(Ce)$ crystal despite the smaller size of the LYSO crystal.

This has a direct impact on the resolution obtainable when considering the number of detected photons. Although cerium doped lanthanum bromide has roughly twice the light yield of LYSO and provides thus better photon statistics, the resolution of a $LaBr_3(Ce)$ crystal is limited by the energy leakage.

Thus the simulations suggest that the available LYSO crystal ($R = 3.5\,\text{cm}$, $L = 16\,\text{cm}$) performs better in terms of energy resolution than the available $LaBr_3(Ce)$ crystal ($R = 4.45\,\text{cm}$, $L = 20.32\,\text{cm}$). A resolution ($\sigma E/E$) of 1.5 % is obtained for the LYSO crystal whereas a resolution of 2.4 % is estimated for a slightly larger $LaBr_3(Ce)$ crystal. The detailed numbers and histograms are shown in Figure 7.4b.

In a further set of studies, the two SiPM candidates were investigated. The S13360-6025PE Type manufactured by Hamamatsu offers 57 600 Pixels of smaller sizes compared to the MicroFJ-60035TSV type with less than half the pixel number. Yet the candidate manufactured by sensL (MicroFJ-60035TSV) offers a significantly increased PDE and a smaller support structure. Thus the active area of the SiPMs in the readout arrays covers a larger fraction of the total area. This suggests that the sensL SiPM (MicroFJ-60035TSV) will collect more photons yet is more susceptible to saturation effects due to the larger pixels.

These expectations are clearly confirmed when considering the results obtained with a $LaBr_3(Ce)$ crystal as shown in Figure 7.5 on the left side. Although the sensL candidate collects roughly twice as many photons, there is hardly any difference in terms of resolution. This effect can be attributed to saturation effects in connection with the ultra-high LY (63 ph/keV) of the lanthanum bromide crystal.

As the LYSO has roughly just half the LY (27 ph/keV) of lanthanum bromide, the total number of detected photons decreases for both candidates as shown in Figure 7.5 on the right side. As expected the sensL candidate (MicroFJ-60035TSV) collects significantly more photons than the other candidate (S13360-6025PE) manufactured by Hamamatsu. However, the use of the sensL candidate yields a slightly better resolution ($\sigma N/N \approx (1.28 \pm 0.05)\,\%$) compared to the Hamamatsu candidate ($\sigma N/N \approx (1.48 \pm 0.04)\,\%$).

A possible explanation for this behaviour are again saturation effects that mainly affect the sensL type SiPM (MicroFJ-60035TSV) due to the larger pixel size. Using LYSO instead of $LaBr_3(Ce)$ results in less photons and consequently less photons lost in the SiPM due to saturation effects. By

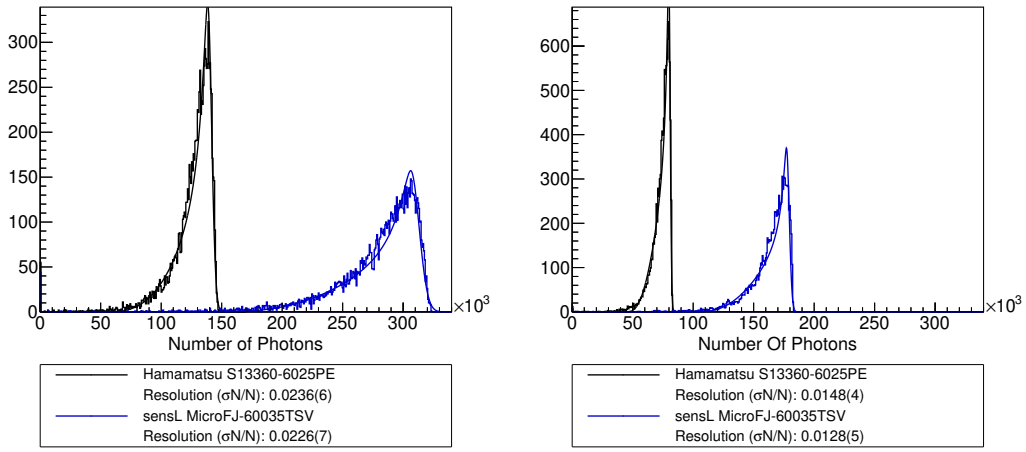

(a) $LaBr_3(Ce)$ (b) LYSO

Figure 7.5: The number of collected photons for the two SiPM candidates. The candidate S13360-6025PE manufactured by Hamamatsu offers 57 600 Pixels and a PDE of 25 %. The candidate MicroFJ-60035TSV manufactures by sensL has less than half the pixels yet offers significantly increased fill factor and total coverage.

reducing the saturation effects the scales are tilted towards the sensL SiPM (MicroFJ-60035TSV) as they provide a better PDE and the increased photon statistics improve the resolution.

7.2 Expected Timing Resolution

This section treats the expected time resolution for different crystals. In order to extract a time, the waveform for a selected few SiPMs is simulated and various sets of different time extraction algorithms are compared.

Apart from the energy resolution, the timing resolution is one of the key features for a detector to be used for cLFV searches, especially when the signal is characterised by a time coincidence of two or more particles.

For the prototype, several different time reconstruction algorithms have been tested. With each of the algorithms the detection time of an event has been recorded for the front readout array and the back readout array.

The “First Photon” algorithm considers the time, at which the first photon in any of the SiPMs on the readout array is detected. The time is directly extracted from the MC simulation and thus is not accessible in an experimental setup. It is introduced as reference.

The “Constant Fraction” (C.F.) method considers the waveform recorded in the SiPM with the highest amplitude on the readout array. The time at which the waveform crosses a threshold of 15 % of its maximum is taken. Any information from further SiPMs is neglected.

The “Average of C.F.” method applies a C.F. algorithm to the waveform with highest amplitude and to all waveforms recorded by neighbouring SiPMs. The obtained values are then weighted according to the amplitude of the corresponding waveform and averaged.

The “C.F. on Sum of Waveforms” method sums the waveform with the highest amplitude and all waveforms recorded by neighbouring SiPMs for each readout array up. The time is extracted by finding the point, where the sum of waveforms passes a threshold of 15 % of its maximal value.

The “First of C.F.” method applies a C.F. algorithm to the waveform with the highest amplitude and to all waveforms recorded by neighbouring SiPMs. The values are compared amongst each readout array and the minimum for each is taken.

By assuming that the initial high-energy photon travels at the speed of light in vacuum and the scintillation photons at the speed of light in the given medium in one dimension the time t_0 at

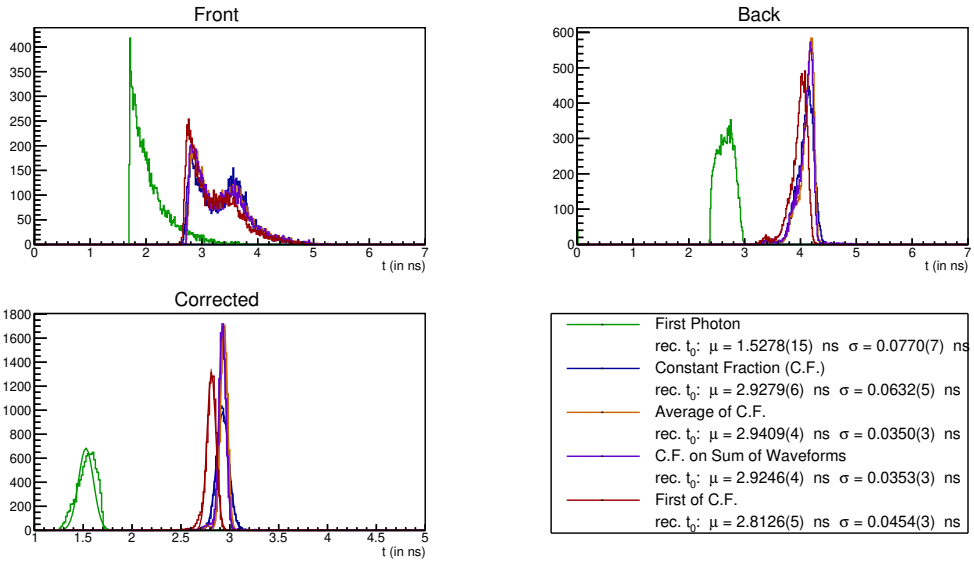

Figure 7.6: Different time extraction algorithms under comparison. The first photon algorithm is based on the arrival time of the first photon on each side. The constant fraction refers to the time at which the waveform passes 15 % of the maximal amplitude in the SiPM with the most photons. The average of C.F. is computed as the weighted average over the available waveforms. For the C.F. on sum on waveforms, the available waveforms were first summed up and then the C.F. method was applied to this sum. First of C.F. refers to the first time of any C.F. result.

which the original photon passes the front face of the crystal can be calculated using the formula

$$t_0 = \frac{(n-1)t_f + (n+1)t_b - \frac{L}{c}(n^2+n)}{2n} \tag{7.2}$$

where n stands for the refractive index (1.9 for $LaBr_3(Ce)$ [94], 1.81 for LYSO [96]) of the crystal, L stands for the crystal's length, $c = 29.98\,\frac{\text{cm}}{\text{ns}}$ for the speed of light in vacuum and t_f (t_b) for the reconstructed event time on the front (back) readout array.

This formula was applied to each of the time reconstruction algorithms. The results are displayed in Figure 7.6. The detection time t_f on the front readout array is represented in the top left. The detection time t_b is drawn on the top right. The estimated entrance time t_0 is shown on the bottom left for each of the algorithms.

For each of the readout arrays, the "First Photon" method provides values lower than the C.F. based methods. This is not further astonishing as this one triggers on the first arrival whereas the C.F. based methods are waiting until the waveform is built up and thus trigger on the arrival of the bulk of optical photons.

The time reconstructed on the front using any of the C.F. methods features an additional peak at around 3.5 ns, caused by events deeper inside the crystal. Due to reflections on the lateral sides of the cylinder, the waveform with the highest amplitude is dominated by photons that are reflected off the walls and thus travelled a longer distance compared to the direct path.

For the back readout array a similar feature can be observed. For the C.F. based reconstruction methods there is a small, barely visible peak around 3.5 ns. It has its origin in events close to the back of the crystal and thus direct photons are dominant in the most intense waveform. These events are rare as most of the photons interact closer to the front face and thus the reflected photons are dominant resulting in the main peak around 4 ns.

When applying the theory based Formula 7.2, the distributions obtained feature a peak that can be fitted with an ordinary Gaussian function. The obtained standard deviations provide an estimate of the timing resolution associated with the corresponding algorithm. The obtained resolutions are displayed on the bottom right of Figure 7.6.

Clear variations between the different methods can be observed. The "First Photon" method provides the earliest t_0 for the reason as mentioned above. The obtained value is closest to the

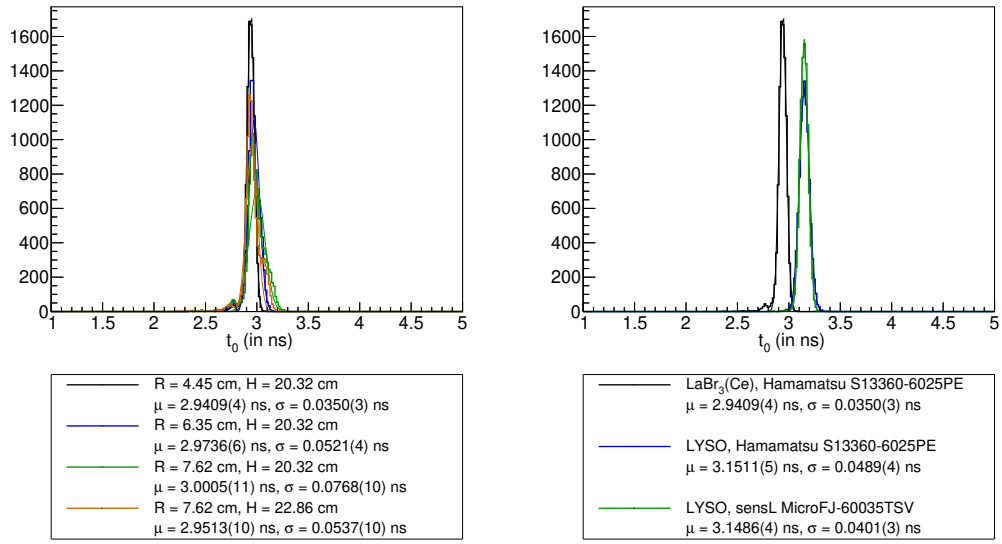

(a) Size of $LaBr_3(Ce)$

(b) Available Crystals

Figure 7.7: Reconstructed entrance time t_0 and timing resolutions based on the "Average of C.F." method. On the left side the results for different sizes of a $LaBr_3(Ce)$ crystal are shown. On the right side the expectations for the available crystals ($R = 4.45\,\text{cm}$, $L = 20.32\,\text{cm}$ for $LaBr_3(Ce)$, $R = 3.5\,\text{cm}$, $L = 16\,\text{cm}$ for LYSO) are displayed. All distributions are fitted with a Gaussian and the obtained mean μ and standard deviation σ are provided in the legends.

MC truth value yet is highly susceptible to statistical fluctuations of the single photons. Thus it provides the worst resolution.

The methods based on a C.F. method perform better in terms of resolution yet are biased for the reason mentioned above. This effect can easily be taken care off by calibrations. Considering the argument of the statistical fluctuations again it is not astonishing, that the "Average of C.F." and the "C.F. on Sum of Waveforms" provide the best resolution as they include all the available information in the final estimate of the time.

For simplicity, only the "Average of C.F." method is considered in the further studies. The results obtained are displayed in Figure 7.7. Each of the distributions is fitted by a Gaussian and the obtained mean μ and standard deviation σ are given in the legend.

On the left side (Figure 7.7a) the results obtained for $LaBr_3(Ce)$ crystals of different sizes are displayed. The chosen sizes correspond to the sizes already considered for the energy resolution studies in the previous section. For the currently available crystal coupled to Hamamatsu S13360-6025PE type SiPMs a time resolution of 35 ps is suggested by the simulation.

By increasing the radius to 6.35 cm respectively 7.62 cm the timing resolution is worsened to 52 ps respectively (77 ± 1) ps. By increasing the length of a crystal with 7.62 cm radius, the time resolution is improved to (54 ± 1) ps. This effect can be possibly explained by the additional transverse distance that is covered by optical photons reflected off the wall. This distance is not included in the theoretical model used to obtain the Formula 7.2 and its impact increases the longer it gets compared to the longitudinal distance along the cylinders axis.

On the right side (Figure 7.7b) the obtained timing distributions for the available $LaBr_3(Ce)$ crystal ($R = 4.45\,\text{cm}$, $L = 20.32\,\text{cm}$) and the LYSO crystal ($R = 3.5\,\text{cm}$, $L = 16\,\text{cm}$) coupled to the S13360-6025 type SiPM manufactured by Hamamatsu are shown. In addition the distribution obtained for the LYSO crystal coupled to MicroFJ-60035TSV SiPMs by sensL is displayed.

For the LYSO coupled to the Hamamatsu SiPM a timing resolution of 49 ps is estimated. Two effects lead to this worse behaviour compared to $LaBr_3(Ce)$. For lanthanum bromide the decay time is quoted to be 16 ns whereas LYSO is by a factor 2.5 slower with a decay time of 41 ns and thus the waveform for LYSO is more stretched out. Further LYSO has only half the light yield of $LaBr_3(Ce)$. This implies that the rising edge of the waveform is defined by less photons when using

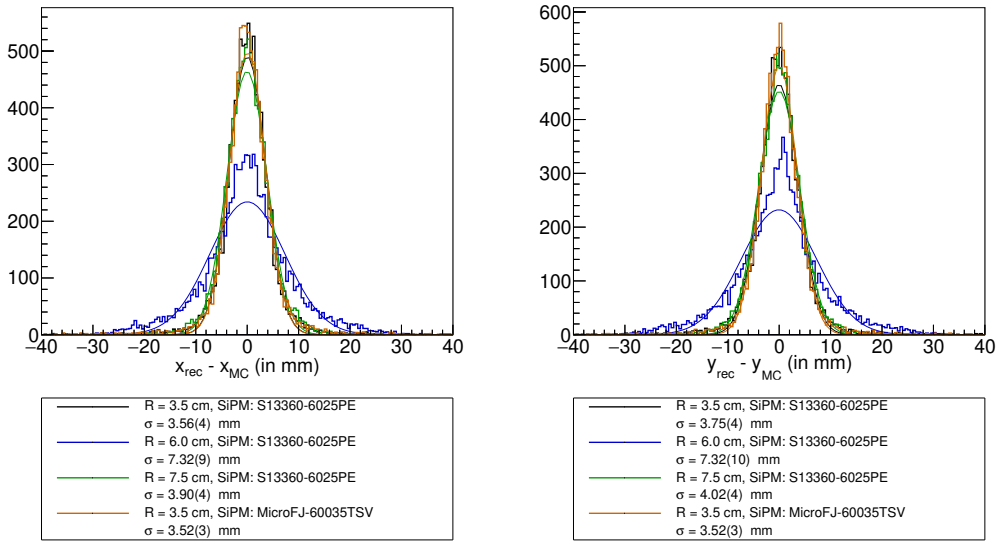

(a) x-Reconstruction (b) y-Reconstruction

Figure 7.8: The spatial resolutions in terms of x and y for different crystal sizes. Note that only LYSO crystals of $L = 16\,\text{cm}$ length are investigated.

a LYSO crystal and consequently more susceptible to statistical fluctuations.

By coupling the LYSO to the sensL SiPMs (MicroFJ-60035TSV) instead of the Hamamatsu ones (S13360-6025PE), the timing resolution can be increased to 40 ps. This is due to the better coverage and PDE that results in improved photon statistics. As can be seen in Figure 7.5 the photon statistics from LYSO coupled to the sensL SiPM is comparable to the one obtained with $LaBr_3(Ce)$ and the Hamamatsu SiPM. Nonetheless the available lanthanum bromide crystal performs better due to the faster decay time.

7.3 Expected Spatial Resolution

This section deals with the three dimensional reconstruction of the first point of interaction inside the scintillating crystal. It explains the reconstruction algorithms as well as the expected resolutions that are obtainable by using them.

So far all simulated photons were incident along the crystals axis on the centre of the front face. In reality, the photons are spread out all over the crystal's front. Therefore the question arises how to reconstruct the position of the first interaction point and what the spatial resolution with a given crystal and reconstruction algorithm is.

For this purpose a set of simulations was conducted for different geometrical configurations where the entire front face of the crystal was illuminated by 55 MeV photons. All photons were generated in one spot 60 cm away from the crystal's centre. They were assigned some divergence to achieve illumination of the entire crystal front.

For the reconstruction the formula

$$x_{\text{rec}} = a\bar{x}_{\text{f}} + b\bar{x}_{\text{b}} + c \tag{7.3}$$

has been used where $\bar{x}_{\text{f}}$ stands for the mean of the x positions of the SiPMs weighted by the number of photons collected on the front readout array and $\bar{x}_{\text{b}}$ stands for the mean on the back readout array. The parameters a, b and c are estimated by an individual fit method comparing x_{rec} to x_{MC} for each crystal geometry in use. The same method has been used for the y direction.

To extract a resolution of this method, the reconstructed values are compared to the MC truth values. The obtained results are shown in Figure 7.8. One can see immediately, that distributions obtained for the x-reconstruction correspond pretty well to the ones obtained for the y-reconstruction. This was to be expected as the cylindrical crystal is symmetric under rotation

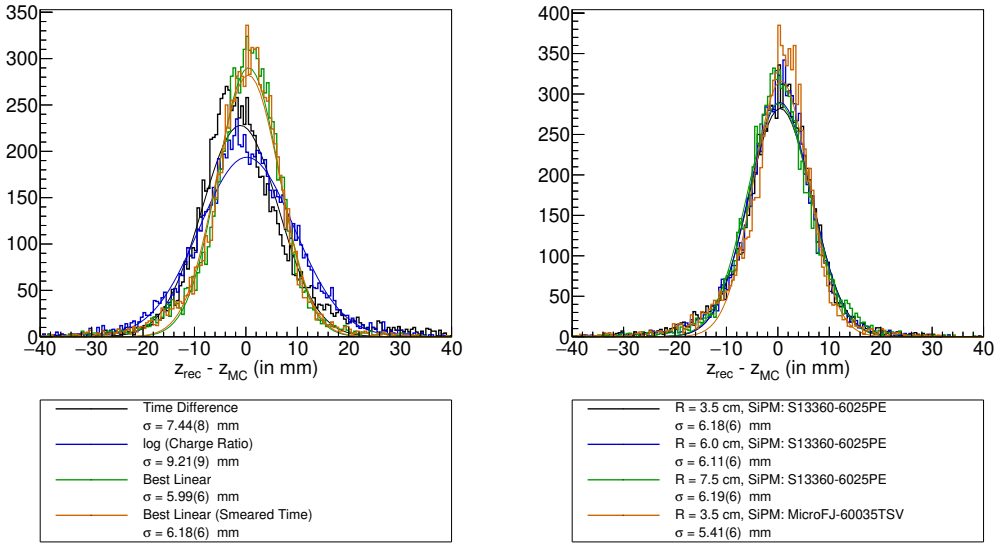

(a) z-Reconstruction Methods

(b) z-Reconstruction Performances

Figure 7.9: The difference between the reconstructed z position and the MC truth values are shown. On the left side, the results for different reconstruction methods are displayed for a LYSO crystal of 3.5 cm radius and 16 cm length coupled to S13360-6025PE SiPMs. The methods are described in the text. On the right side different radii and SiPM types are compared.

around the z-axis. Only the readout array has some asymmetry as it is impossible to optimise coverage using a rotational symmetric arrangement of the SiPMs.

Further there is no need of fitting to see that the histogram associated with a LYSO crystal of 6 cm radius is much wider than the others. The reason for that is the assumption of linear contributions of the means on the front and back readout array to the reconstructions as shown in Formula 7.3. This does not quite match the truth here. The remaining residues contribute significantly to the width of the distribution.

A Gaussian curve has been fitted to all distributions. The standard deviations are given in the legend. A discrepancy between fit and data can be seen by bare eye for the crystal of 6 cm radius. Nonetheless, a resolution of (7.3 ± 0.1) mm is suggested for this crystal and method.

The other distributions are described rather well with a Gaussian function. For a LYSO crystal with a radius of 3.5 cm a resolution of 3.6 mm in x and 3.8 mm in y is observed for the Hamamatsu S13360-6025PE SiPM and a resolution of 3.5 mm in both directions for the sensL MicroFJ-60035TSV SiPM. For a crystal of 7.5 cm radius coupled to Hamamatsu manufactured SiPMs provide 3.9 mm resolution in x direction and 4.0 mm in y direction.

Although it is not required for the geometrical cut the z-component of the position may be crucial for other purposes and thus is reconstructed. The z-coordinate of the event affects the time difference detected between the readouts and the number of photons collected by each SiPM array. Thus both quantities provide useful information that can be used for the reconstruction of the z-position.

The method easiest to understand and most straight forward to implement is based on the time difference between front and back readout. The further away the event happens the longer the photons take to arrive at the SiPMs. As a consequence, the z-coordinate should be a linear function of the time difference. The reconstruction uses the formula

$$z_{\mathrm{rec}} = a(t_{\mathrm{f}} - t_{\mathrm{b}}) + b \tag{7.4}$$

where a and b are parameters determined by the fit method provided by the ROOT framework [100] and $t_{\mathrm{f,b}}$ stand for the estimated time for the front respectively back readout. This method is represented by the black histogram in Figure 7.9a for a LYSO crystal of a radius of 3.5 cm and a length of 16 cm.

Another method is based on the charge only. Observations with scintillating fibres [101] suggest a strong, linear correlation between the z-coordinate and the logarithm of the charge ratio between the two readouts. The corresponding reconstruction uses the formula

$$z_{\mathrm{rec}} = a \ln\left(\frac{N_{\mathrm{f}}}{N_{\mathrm{b}}}\right) + b \tag{7.5}$$

where again the parameters a and b are estimated by ROOT's built in fit method and $N_{\mathrm{f,b}}$ stand for the number of collected photons on the respective readout. The results are shown by the blue histogram in Figure 7.9a. It can be seen that the resolution is worse compared to the previous method relying on the time difference.

A more advanced method combines the information obtained from the time with the information obtained from the charge. As seen in the previous section, there are some deviations from the 1D model of light propagation. The subsequent time reconstruction on the back side triggers on photons reflected from the walls and not on the direct light. As a result the simple assumption of the linear dependence on the time difference may need adjustment. As a consequence, the following formula has been used for the reconstruction

$$z_{\mathrm{rec}} = a t_{\mathrm{f}} + b t_{\mathrm{b}} + c \ln(N_{\mathrm{f}}) + d \ln(N_{\mathrm{b}}) + e \tag{7.6}$$

where the five parameters a, b, c, d and e are estimated based on an individual fitting algorithm. The results are referred to as "Best Linear" and represented as green histogram in Figure 7.9a.

This method has a massive drawback though. It accesses the times $t_{\mathrm{f,b}}$ directly which cannot be repeated in the real experiment as the true time of the initial γ is unknown. In the experiment one has to do with the relative time between auxiliary detector and the main LXe calorimeter. This will introduce an additional uncertainty based on the 50 ps resolution of the XEC. It was taken care of by smearing the obtained times accordingly. The results are represented in Figure 7.9a as orange histogram and referred to as "Best Linear (Smeared Time)" in the legend.

In Figure 7.9b the performance of this method for the different geometrical configurations already used above are shown. Hardly any differences can be seen in the distributions for crystals of different radii coupled to Hamamatsu S13360-6025PE type SiPMs. Fitting provides statistically equal results between 6.1 mm and 6.2 mm for the standard deviation. The individual values are given in the legend. A slightly better resolution is obtained for the LYSO crystal coupled to the MicroFJ-60035TSV SiPM manufactured by sensL. Here a z-resolution of around 5.4 mm is obtained.

7.4 Geometrical Cut

For events close to the lateral regions of the scintillating crystal, the estimated resolutions are worse, spoiling the overall performance. This section explores the potential use of geometrical cuts to reject the most lateral events and to improve the resolutions of the photon variables for the remaining events.

Another point to be addressed are the energy and time resolutions achievable once the photons are spread out. In a first step, a set of simulations has been done using a LYSO crystal of 3.5 cm radius and 16 cm length. Different divergences were chosen, such that all photons hit within a circular area given by the radius r_b around the crystals centre on the front face. The obtained results for energy and time resolution are represented in Figure 7.10.

The first thing to notice is the drastic decrease in detection efficiency when the entire front face of the crystal is illuminated. This can be seen from the orange histogram in Figure 7.10a where the lowest bin with no detected photons is the most populated. Divergent photons that enter the crystal close to the edge need to pass a drastically reduced amount of material before leaving the crystal through its lateral side. Due to the shorter distance in the LYSO the probability of an interaction is reduced and so is the detection efficiency for these events. Nonetheless these undetectable events make up less than 8 % of the total amount. This suggests a detection efficiency of above 90 % in this case.

To extract the resolutions the data of the detected number of photons is fitted with a tailed Gaussian as given by Equation 7.1 and the obtained distribution of the entrance time t_0 is fitted with an ordinary Gaussian function. As the radius where the incident photons can hit the crystal increases the extracted resolution decreases. This effect becomes more significant as the outermost

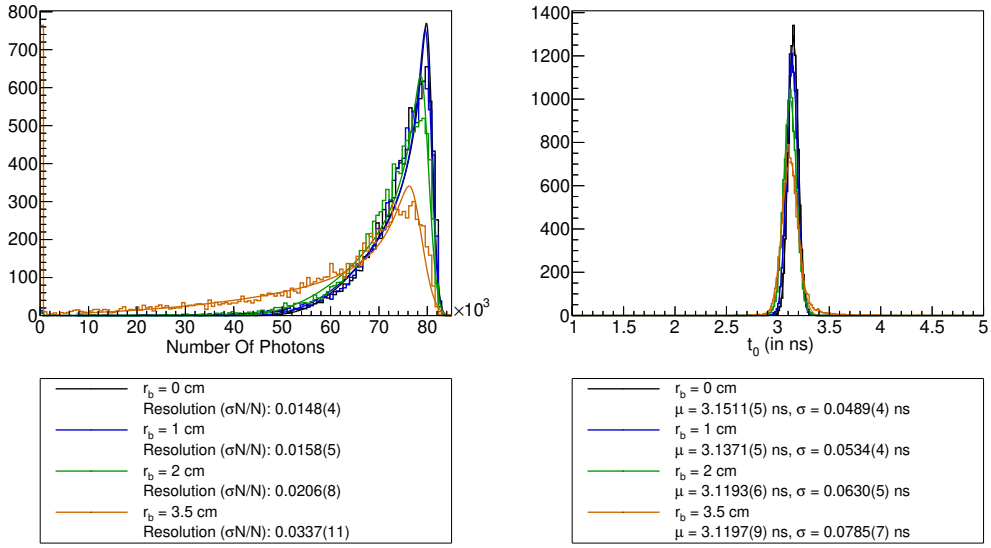

(a) Number of Photons (b) Timing

Figure 7.10: The effect of a spread out distribution of photons incident on a LYSO crystal of the available size $R = 3.5\,\text{cm}$, $L = 16\,\text{cm}$. Both energy and time resolutions start to worsen once the incident photons start to hit near the edge of the cylindrical crystal.

events approach the edge of the crystal and get closer than the Molière radius of $R_M \approx 2.1\,\text{cm}$ of LYSO.

A possible way to tackle this issue on the hardware level is to place a lead collimator in front of the assembled detector prototype. Incident photons that would hit the outer parts of the crystal's front face are absorbed in the collimator instead. As a consequence the detection rate gets reduced. This affects the CEX calibration of the LXe calorimeter adversely as the auxiliary detector serves the primary purpose of asserting time coincidence and back to back geometry of the two photons emitted by the π^0 decay.

A more sophisticated approach is to take advantage of the granularity of the readout arrays. All events get recorded for the CEX calibration purpose. In a second step for the prototype characterisation a selection is applied on the software level to select only events that are well contained and don't spoil the resolution due to leakage effects.

On the one hand it is possible to reconstruct the position (x, y, z) of the event using the methods described in the previous section and then select only events at a certain distance from the edge. For obvious reasons, this requires the determination of the reconstruction parameters needed for the x and y direction first. In total seven parameters have to be fixed (three for x reconstruction, three for y reconstruction and one for the radial cut). The advantages are that the position is reconstructed in parallel respectively the cut is implemented easily if the position is already reconstructed.

On the other hand it is possible to discriminate directly on the patterns observed in the readouts. They differ significantly depending on the position of the first conversion. Two of the possible pattern styles are shown in Figure 7.11. The upper image (Figure 7.11a) shows a typical pattern for an event in the central region of the crystal. Most of the photons are collected in the central region of the SiPM array on the front readout and on the back readout.

The lower image (Figure 7.11b) shows the pattern for an event in the outer region of the crystal. Most of the photons stay in the outer region of the SiPM arrays and illuminate parts of a ring. The distribution is reminiscent of the illuminated shape on the bottom of a pan when the sun shines diagonally into it. As a matter of fact, both shapes have their origin in the same phenomena: reflection of light on a curved surface. In cases where the event happens very close to the front readout, there is but one bright spot and the pattern is only observable on the back readout.

The easiest possible way to distinguish them is by the radial distribution of the photons. Central events (Figure 7.11a) have their photons distributed uniformly or with a tail towards higher radii.

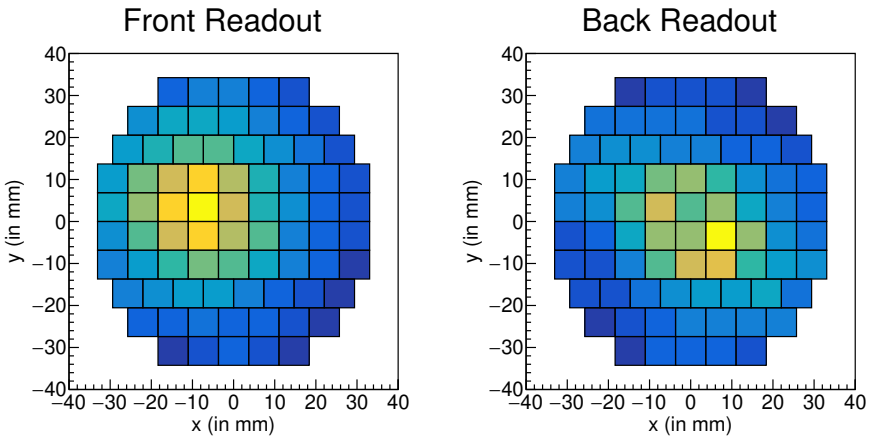

(a) Hit in Central Region: $(x, y) = (-10\,\text{mm}, 3\,\text{mm})$

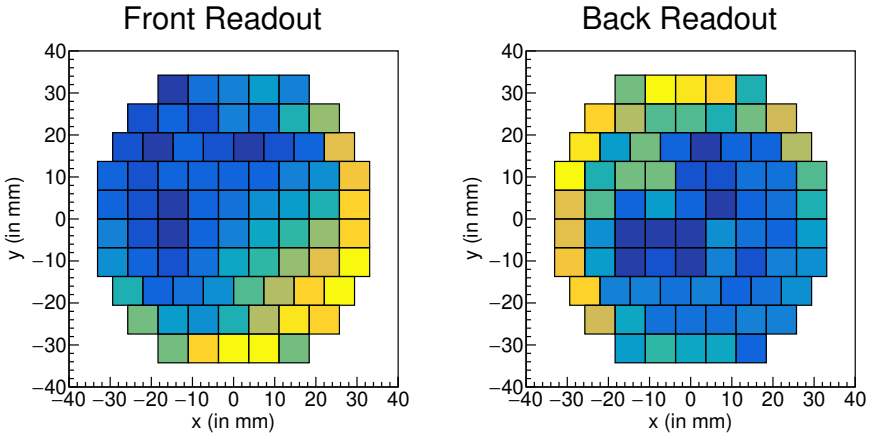

(b) Hit in Outer Region: $(x, y) = (23\,\text{mm}, -21\,\text{mm})$

Figure 7.11: The spatial distribution of the detected photons on the readout arrays. Each square represents one SiPM. Yellow coloured SiPMs collected the most photons in the given array and event. Blue coloured SiPMs collected the least. The scales are not comparable.

Events from the outer part (Figure 7.11b) have most of their photons at larger radii with clearly observable tails towards lower radii. This has an immediate impact on the distribution's skewness.

The transition however is somewhat continuous and thus the cut has to be carefully selected to find a good trade-off between cutting away events with an adverse effect and not cutting good events. The cut on the radial skewness has to be adjusted for each crystal geometry. This method requires only one parameter for the cut to be estimated.

For two of the considered setups the result of the geometrical cut is displayed: For the case of a LYSO crystal of 3.5 cm radius and 16 cm length coupled to S13360-6025 SiPMs manufactured by Hamamatsu the obtained distributions are shown in Figure 7.12. For the case of a LYSO crystal of 7.5 cm radius coupled to the same SiPM type are shown in Figure 7.13.

For both setups a cut based on the reconstructed radius is shown in green, a cut based on the skewness is shown in blue and a cut based on the MC truth value of the radius is shown in orange. On the left side, the radial distribution of the cut events is displayed: Events passing the cut are displayed in solid colour while events failing the cut are displayed in the hashed histogram. They sum up to the black curve. On the right side the distribution of the collected photons is displayed for the events passing the cut (lighter hue), for the ones that fail the cut (darker hue) and for all of them (black).

In addition to the two cuts discussed above, a cut based on the MC truth value is shown in orange on the bottom of each plot. This serves as reference and rough estimate of the resolutions obtainable with a collimator in front of the crystals front face. One can observe that the cuts based

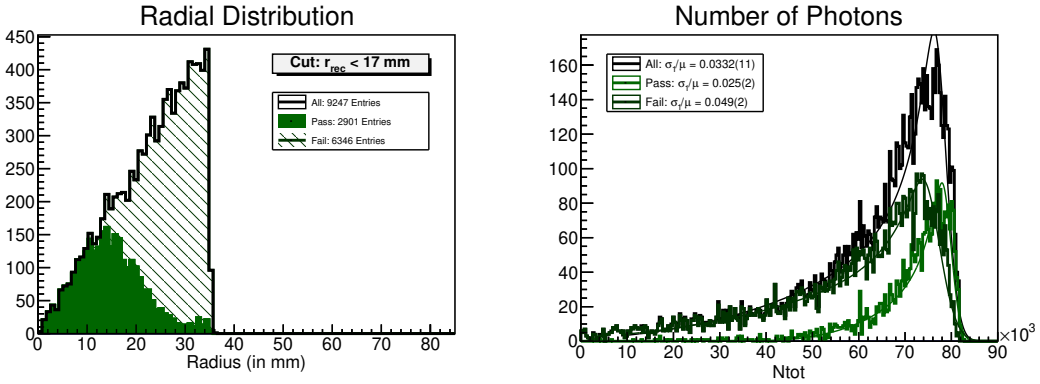

(a) Cut based on the reconstructed radius

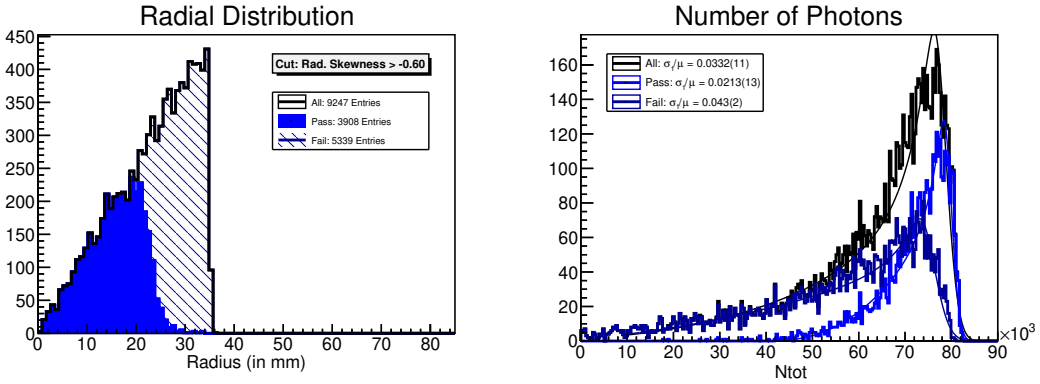

(b) Cut based on the skewness

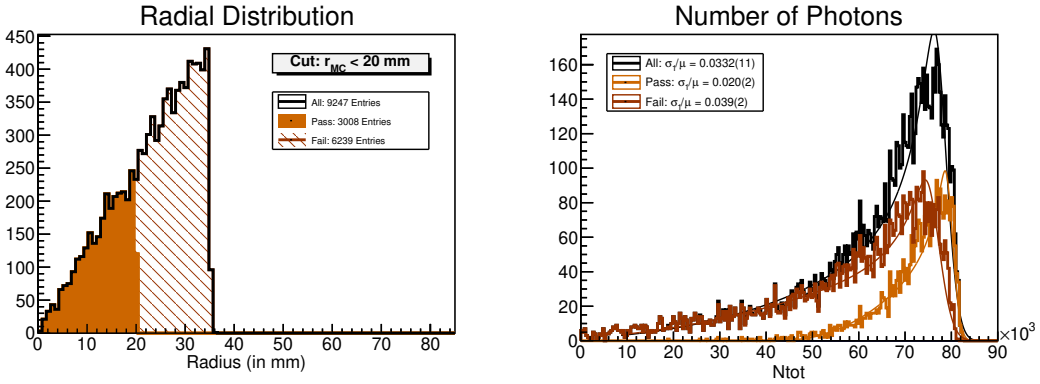

(c) Cut based on the MC truth radius

Figure 7.12: The effect of a geometrical cut shown for the available LYSO crystal ($R = 3.5\,\text{cm}$, $L = 16\,\text{cm}$) coupled to S13360-6025 SiPMs. On the left side, the radial distribution as obtained from MC truth values for events passing the cut is shown in the solid filled histogram. The ones failing the cut are represented by the hatched, stacked histogram. On the right side, the number of collected photons for both groups and the combination of the two is shown.

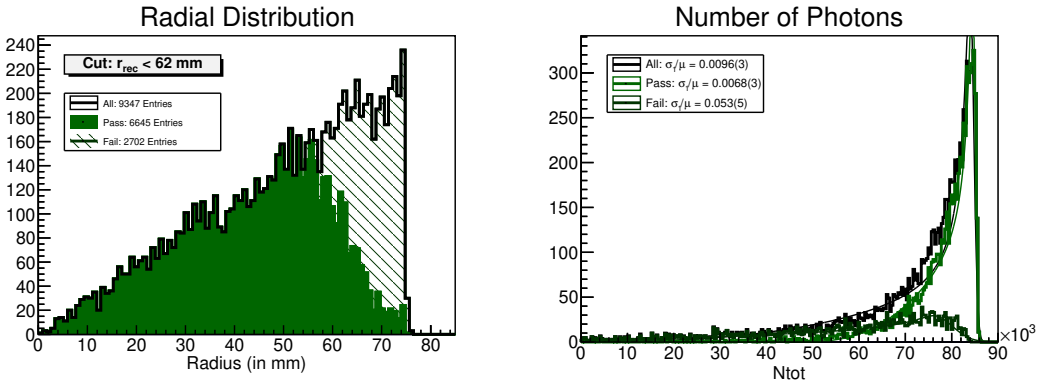

(a) Cut based on the reconstructed Radius

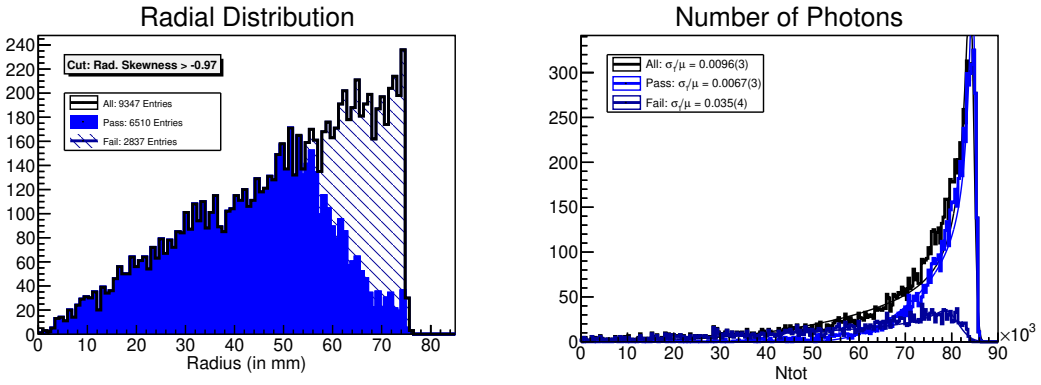

(b) Cut based on the skewness

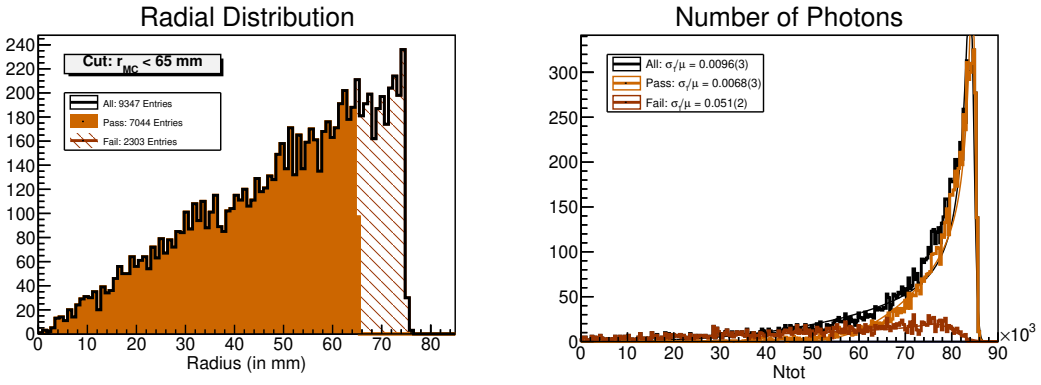

(c) Cut based on the MC truth Radius

Figure 7.13: The effect of a geometrical cut shown for a larger LYSO crystal ($R = 7.5\,\text{cm}$, $L = 16\,\text{cm}$) coupled to S13360-6025 SiPMs. The same plots are displayed as already shown in the previous one. It can be seen clearly, that again both cuts lead to the desired goal. One is able to remove the events close to the edge of the crystal. The efficiency of the cut increased drastically compared to the smaller, available crystal.

on the skewness or the reconstructed radius perform very similar to the cut on the MC truth values.

For the smaller crystal the aim is to recover the resolutions obtained with a reduced area of impact of 2 cm radius as discussed above in Figure 7.10. The results are displayed in Figure 7.12. An efficiency of roughly 30 % was estimated for all of the cuts. This corresponds to the fraction of events inside the desired sensitive area.

By fitting the obtained distributions for the number of detected photons with a tailed Gaussian function as given by Formula 7.1 one can estimate the resolution in terms of energy. The obtained resolution after applying a geometrical cut is around 2 %. This corresponds to the resolution obtained for an area of impact with the radius of 2 cm as shown above in Figure 7.10a.

Comparing the larger crystal of radius $R = 7.5$ cm to the available one, it can be seen immediately, that the solid coloured area increases. This is due to the fact that the efficiency of the detector increases as the fraction of the volume further away from the edge of the crystal increases. An efficiency of around 70 % is estimated.

Again both of the cuts lead to the desired result of removing the outermost events in the crystal which then leads to an improved resolution for the inner events. The events on the inside are now competitive with the resolutions already obtained for the point-like distribution of the incoming photons.

This suggest that once larger crystals are commercially available, it would become feasible to build a detector from either LYSO or $LaBr_3$(Ce) crystals coupled to SiPMs. Using a geometrical cut, one can get rid of events close to the edge where a lot of energy leakage has to be expected.

7.5 Waveform Simulations and Noise Effects

This section treats advanced waveform simulations for all channels. This includes the full data acquisition electronics. The effects on the previously mentioned reconstruction methods are discussed.

So far, the waveform was only considered for a selected few channels. Each photo-electron was assumed to produce an identical response and noises were neglected. However, all these factors are potential sources of uncertainties on the final resolutions. For these reasons, some more advanced simulations including the waveform generation for each channel were performed.

To generate the full waveform the following assumptions were made for the response to one photo-electron: The rising edge is described by a Gaussian shape with a rise time of 0.6 ns as standard deviation. The maximum is reached 1.8 ns after the photon hits. After the maximum, an exponential decay with a characteristic decay time of 2.8 ns is assumed. The total amplitude for one photon is given by 1.0 ± 0.1 r.u. where a Gaussian distribution of the amplitude is presumed.

To obtain the full waveform, the responses for all photo-electrons are summed up distributed in 1024 bins representing a 200 ns time window as given by the DRS chips on the WaveDREAM board [76]. In addition, some random noise is added to each of the bins. It is assumed to follow a Gaussian distribution with a standard deviation of 0.5 r.u. for the low noise scenario, 5 r.u for the medium noise scenario and 10 r.u. for a high noise scenario. The low noise scenario assumes ideal conditions. The medium scenario corresponds to a pessimistic assumption for the development of the electronics, recently proven too pessimistic. The high noise scenario corresponds to a highly exaggerated situation.

For each of the channels, the charge associated to the waveform is calculated as the integral over the whole time window, i.e. the sum over all bins of the waveform. The time for each waveform is estimated by the use of the constant fraction method using a threshold of 15 % of the total amplitude.

Note that this method may produce bad results in case of low signal and high noise conditions where the random noise easily exceeds the threshold. To counteract this issue, the sum of all waveforms on each face of the crystal is calculated. Then the constant fraction method is applied to this summed waveform yielding a time for the front side respectively for the back side.

To estimate the time resolution, the same formula as in the previous Section 7.2 is used.

$$t_0 = \frac{(n-1)t_f + (n+1)t_b - \frac{L}{c}(n^2+n)}{2n} \tag{7.7}$$

The only difference is how the times t_f and t_b in this equation are estimated. Now that all waveforms are available, the following algorithms are used and displayed in Figure 7.14.

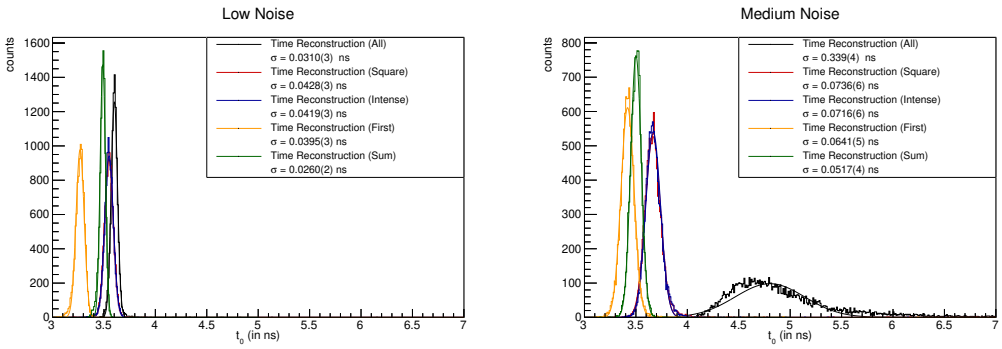

(a) Low Noise Scenario

(b) Medium Noise Scenario

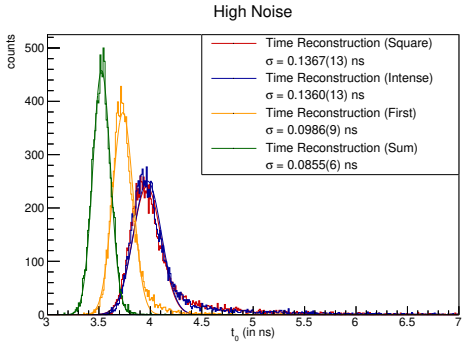

(c) High Noise Scenario

Figure 7.14: Comparison of different time algorithms under different noise conditions. All simulation data is obtained for the configuration of Hamamatsu S13360-6025PE SiPMs coupled to a LYSO crystal with $R = 3.5\,\text{cm}$, $L = 16\,\text{cm}$. Description of the individual algorithms is in the text.

The first option labeled "all" averages the obtained constant fraction times of all channels associated with one face. It uses the corresponding charges as weights. These results are represented in black colour in Figure 7.14. One can observe that this works rather well in the low noise high signal environment. However, as soon as the noise gets higher, this method ceases to work as can be seen from the medium noise scenario. This method is not used in the high noise scenario as it completely fails to produce results within reasonable bounds.

The second option labeled "square" is based on the previously used "Average of C.F." method described in Section 7.2. It finds the one channel with the most collected charge on each side and then averages the times over all channels inside a square centred on this channel. The results from this method are represented in red colour in Figure 7.14.

The third method labeled "intense" selects simply the ten channels on each side providing the most charge. For each side, the time is estimated as the weighted average of the constant fraction times weighted by the collected charge in said channel. The results are represented in blue colour. As can be seen from Figure 7.14, the "intense" and the "square" method perform almost identically. This can be explained by the fact, that the brightest spot on each face is a somewhat localised phenomena - as a consequence the channels selected for the two methods often correspond to each other.

Another attempt was made by using the ten channels which provide the earliest times. This method is labeled "first". Again the times obtained are averaged and weighted by the collected charge. Although this method looks rather promising on first sight, the problems start once larger crystals are trialed where the number of channels is increased drastically. As a similar amount of light now spreads over many more channels, the signal in at least some of the channels will be lowered. As soon as the noise level surpasses the constant fraction threshold, arbitrary times are obtained from this algorithm. This effect is not yet visible in the simulations for the available LYSO crystal as represented in Figure 7.14.

The most promising algorithm so far was the so called "sum" method. Here, the waveforms of

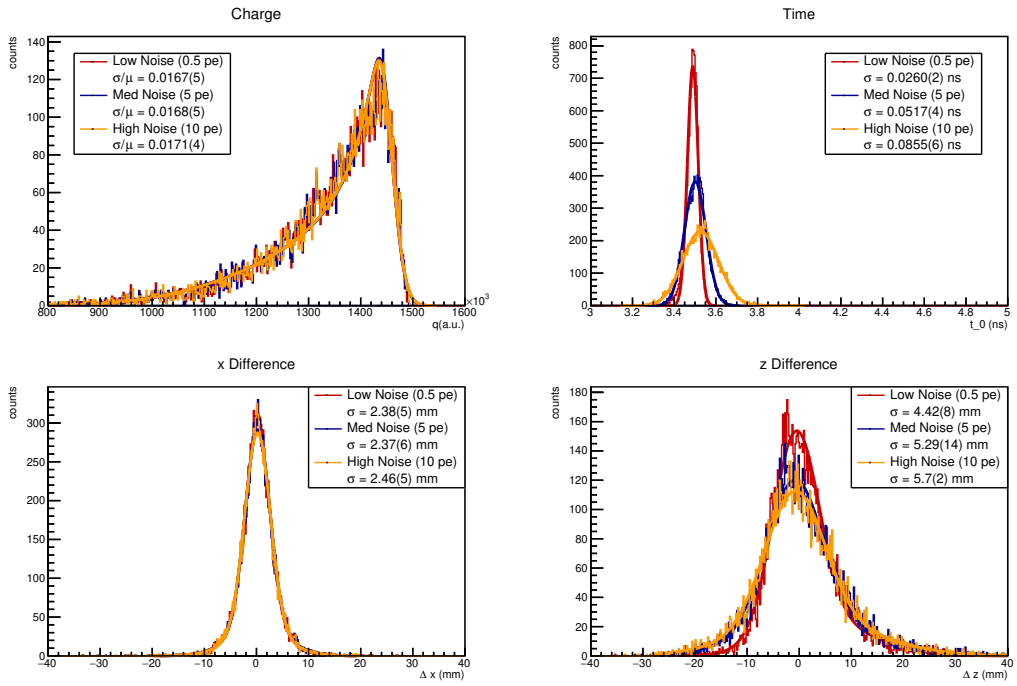

Figure 7.15: Effect of the noise on the reconstruction variables energy, time and position. Three different noise scenarios are considered as described in the text.

all channels get summed up to form a collective waveform for the front side and another one for the back side. The constant fraction method is then applied to these sums. The obtained results are represented in green in Figure 7.14.

It is observable that the "sum" method is more resistant to noise compared to the other methods in this section. Based on these results it was decided to continue only with the sum method. Any further reference to time refers to this method.

In a second step, the effect of the noise on the reconstructed variables energy, time and position was investigated. For this purpose it is assumed, that the energy is proportional to the total charge collected. The time is estimated in the way mentioned above and the positions are estimated based on the algorithms mentioned in the previous Section 7.3.

The most important results are represented in Figure 7.15 where a LYSO crystal with $R = 3.5\,\mathrm{cm}$, $L = 16\,\mathrm{cm}$ coupled to Hamamatsu SiPMs (S13360-6025PE) is considered. One can observe that the charge distribution for this configuration is unaffected by an increased noise level. The same basically holds true for the x difference between MC truth and reconstructed value.

This appears reasonable as the signals are rather high compared to the amount of noise expected. Furthermore, the reconstruction of charge and x position relies on the integrated charges only, making them somewhat more resilient to the Gaussian distributed noise. This is due to the fact, that the effect of the noise scales with the square root of the number of bins used in the integration while the charge is estimated as the sum over all channels.

On the other hand the noise has significant impact on the time reconstruction. The time estimate as used in the current algorithm relies basically on three bins of the summed waveforms: The bin with the highest amplitude defines the threshold and the two bins at the crossing are used to extract the time. Now that the constant fraction method includes the calculation of differences between the values of these bins, the relative uncertainties get increased. This eventually results in the large effect observed in the top left histograms in Figure 7.15.

Furthermore an effect of the noise on the reconstructed z position is observed as well. This originates from the fact that the reconstruction of the z position adapted from Equation 7.6

$$z_{\mathrm{rec}} = a t_{\mathrm{f}} + b t_{\mathrm{b}} + c \ln(Q_{\mathrm{f}}) + d \ln(Q_{\mathrm{b}}) + e \tag{7.8}$$

relies on the reconstructed times t_i and the reconstructed charges Q_i. In this equation, the reconstructed times are affected by the noise, the charges are not.

Noise	a	b	c	d	e
low	104	27	53	−57	−512
medium	9	−9	−265	254	131
high	0.5	−0.2	−307	296	134

Table 7.3: Parameters for z reconstruction obtained from the first 20 % of the data for the available LYSO crystal ($L = 16\,\text{cm}$, $R = 3.5\,\text{cm}$) coupled to Hamamatsu SiPMs.

By opening the box, one finds values similar to the ones given in Table 7.3 for the parameters. These values are based on 20 % of the dataset obtained for the available LYSO crystal ($L = 16\,\text{cm}$, $R = 3.5\,\text{cm}$ coupled to Hamamatsu SiPMs. Fluctuations of $\mathcal{O}(1)$ are observed by selecting a different set of equal size. Larger fluctuations appear for smaller sets.

Despite the fluctuations, the tendency is clearly observable: As soon as the noise increases, the parameters a and b associated with the times are decreased while the parameters c and d associated with the charges are increased. This implies that in the case of high noise, the reconstruction relies more on the reconstruction of the noise-insensitive charges and less on the noise-sensitive times.

7.6 Light Yield Studies

This section includes studies of hypothetically modified light yields. These are ultimately used to assess the potential benefits of the higher light yield of BrilLanCe.

As mentioned before in Table 7.1, BrilLanCe convinces by its high light yield and fast decay time. LYSO on the other hand features a high density, short radiation length and smaller Molière radius and thus better energy containment. To determine which of these characteristics is more beneficial to the final resolution, alternative values for the LYSO light yield were tested.

For each configuration, the obtained variable distributions were fitted with the corresponding function. This corresponds to a tailed Gaussian for the charge distribution and an ordinary Gaussian for position and time. For the position resolutions an additional Gaussian is used to fit the tails. These are in general rather small yet still enough to disturb a fit with just a single Gaussian.

The results obtained are displayed in Figure 7.16. The data was acquired for a LYSO crystal coupled to the sensL MicroFJ-60035TSV type SiPM. The generation and analysis of the waveform is included and the low noise scenario considered. For the available crystals, the radius is $R = 3.5\,\text{cm}$ and the length is $L = 16\,\text{cm}$. For the large one, the values are $R = 7.5\,\text{cm}$ and $L = 16\,\text{cm}$.

For the charge resolutions one can observe that it saturates at a light yield of around 30 ph/keV, probably even earlier. This corresponds to the real light yield of LYSO. Thus one can conclude that the charge resolution at energies $\mathcal{O}(50\,\text{MeV})$ does not significantly benefit from the higher light yield of lanthanum bromide and the light yield is not a limiting factor at this point. The results however confirm that the geometry itself is.

The observed behaviour for the time resolution shows a different picture. There is an obvious decrease of the uncertainties with an increased light yield. On the whole scale, the changes due to light yield exceed the geometrical factors clearly. Even when going from 30 ph/keV (LYSO) to 60 ph/keV (lanthanum bromide: 63 ph/keV) a significant increase of the time resolution is observable.

This suggests that the time resolution would in principle favour an increased light yield. The previous comparison between LYSO and $LaBr_3$(Ce) in Section 7.2 appears to support this. However, it has to be considered that the time reconstruction algorithm was adapted to the new situation where all waveforms are available. A comparison with the available and large crystal is given in Figure 7.17. A comparison with the previous results in Section 7.2 shows that mainly LYSO profits from the updated time reconstruction algorithm based on the sum of all waveforms. As a result, both materials provide a time resolution around 30 ps.

Considering this additional information, the scales could tilt to either side in terms of time resolution. Detailed simulations and probably dedicated time reconstruction algorithms are required to chose the better option if one is only interested in time resolution.

For the x-position resolution hardly any dependencies on the light yield are found as can be seen in Figure 7.16c. For the two datasets associated with a point-like beam distribution, the reconstruction parameters obtained form the spread distribution are used and then compared to

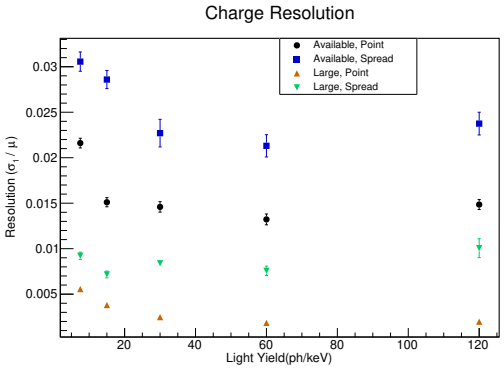

(a) Charge

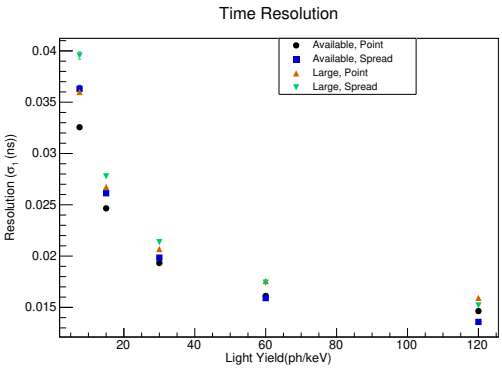

(b) Time

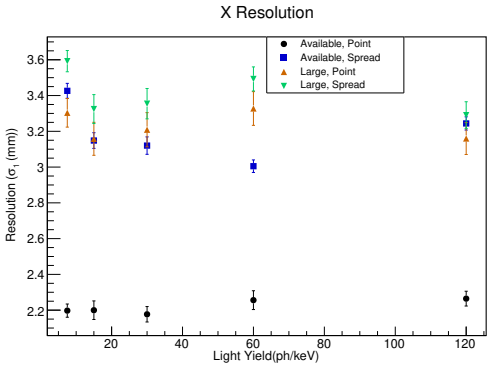

(c) x-Position

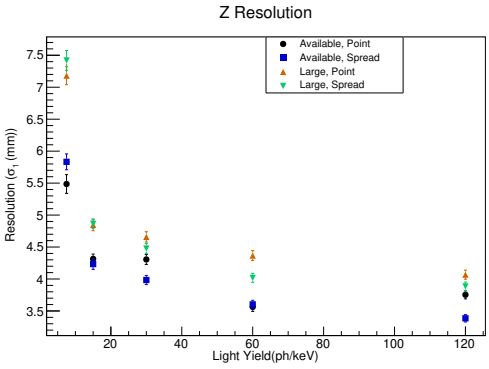

(d) z-Position

Figure 7.16: The effect of the light yield on the reconstructed variables. The resolutions for charge and x-position are already reaching their limits at the LYSO light yield. The z-position and time resolution increases when increasing the light yield. Error bars show uncertainties of the fit.

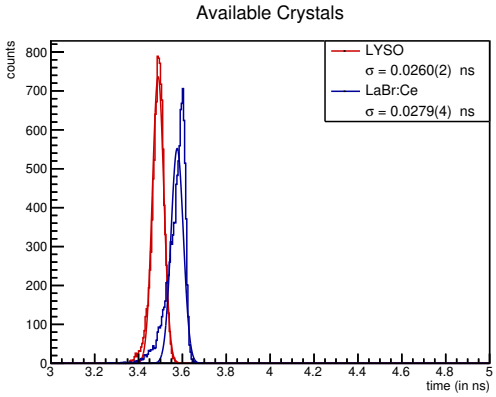

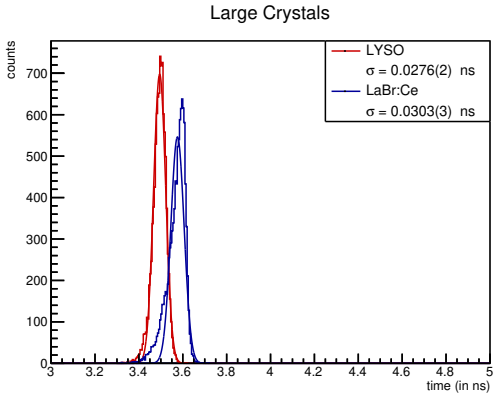

Figure 7.17: Time Resolution Comparison between LYSO and $LaBr_3(Ce)$. Both materials provide excellent resolutions. The updated time algorithm based on the sum of all waveforms on each side has been used.

the MC truth value. For each light yield and crystal size, individual parameters were estimated for the reconstruction.

For the training it was observed that these parameters are susceptible to the underlying data and vary from light yield to light yield. In theory, this should not happen as these are of pure geometrical nature and only the center of the charge distribution enters the reconstruction. The light yield however determines only the amount of photons created but not their distribution.

The reconstruction of the z-position follows a similar behaviour as the time resolution. This is not further astonishing as the z-position reconstruction relies on the observed times and the charges collected at each side. However, the improvement for light yields above 30 ph/keV is smaller compared to the time as the z-position uses the charges to some extend which are already stable.

In the end one can say that the resolutions in charge and x position are not limited by the light yield of LYSO. Some minor improvements can be achieved in terms of z-position. For the time resolution there are some improvements due to the light yield yet a direct comparison to cerium doped lanthanum bromide does not hold clear evidence for a better performance of $LaBr_3$(Ce). Depending on the concrete application either of the materials could be the one with slightly better timing resolution.

Concerning the MEG II experiment where good resolutions are mandatory to reject the background, as can be taken from the MEG II proposal [71], the accidental background rate R_{acc} can be estimated by the following simple formula:

$$R_{\text{acc}} \propto R_\mu^2 \cdot \Delta E_\gamma^2 \cdot \Delta P_e \cdot \Delta \Theta_{e\gamma}^2 \times \Delta t_{e\gamma} \tag{7.9}$$

Here the muon beam rate R_μ and the momentum resolution of the positron ΔP_e are of no further interest. The properties of a potential γ calorimeter would enter through the resolutions in the photon energy (ΔE_γ), in the relative angle between positron and photon ($\Delta \Theta_{e\gamma}$) and in the relative time ($\Delta t_{e\gamma}$).

This implies that the charge resolution enters through the energy resolution with a power of two, the (x, y) position resolutions enter through the relative angle with a power of two as well and the time resolution enters linearly. Thus in the case that a decision has to be made, a future calorimeter benefits more from improved charge and position resolutions rather than time resolution. With this in mind, LYSO provides currently the better option than lanthanum bromide.

Based on these results, the decision was taken to build a prototype using a LYSO crystal with a diameter of 7 cm and a length of 10 cm. The shorter length is chosen as the manufacturer EpicCrystal [102] could not guarantee a 16 cm long crystal without defects [103]. As the light yield and the PDE was found to be not the major limiting factor, the decision to go with the Hamamatsu S13360-6025PE SiPM was taken. While the constituents were already delivered, the assembly was not yet completed at the time this thesis was completed and thus no actual results can be presented.

7.7 The Ideal Situation

Assuming no further restrictions in terms of crystal size, this section deals with the expected performance of the scintillating materials for crystals that easily contain the whole shower. Therefore, crystals with a length corresponding to 15 *radiation lengths and a radius of* 10 *Molière radii are considered.*

The ultimate goal to be achieved is to build a calorimeter for future cLFV experiments. For this purpose, larger areas have to be covered with active material. This triggers the question on the performance of larger crystals. Therefore, LYSO and $LaBr_3$(Ce) crystals of $15X_0$ length and $10R_{\text{M}}$ radius are considered in the following. This corresponds to a LYSO crystal with $L = 17$ cm and $R = 20$ cm and to $L = 31.5$ cm and $R = 23$ cm for $LaBr_3$(Ce).

The results are displayed in Figure 7.18. Both materials provide excellent resolutions in terms of all the interesting variables. In an ultimate scenario with a hypothetical crystal size not yet available, the geometrical factors are not as limiting as for the smaller crystals. Therefore a better energy resolution can be obtained for BrilLanCe as it would be profiting from its better light yield.

This theory gets supported by the fact that the sensL SiPMs perform better than the Hamamatsu ones as sensL SiPMs provide a significantly higher PDE. Furthermore, one can see that the

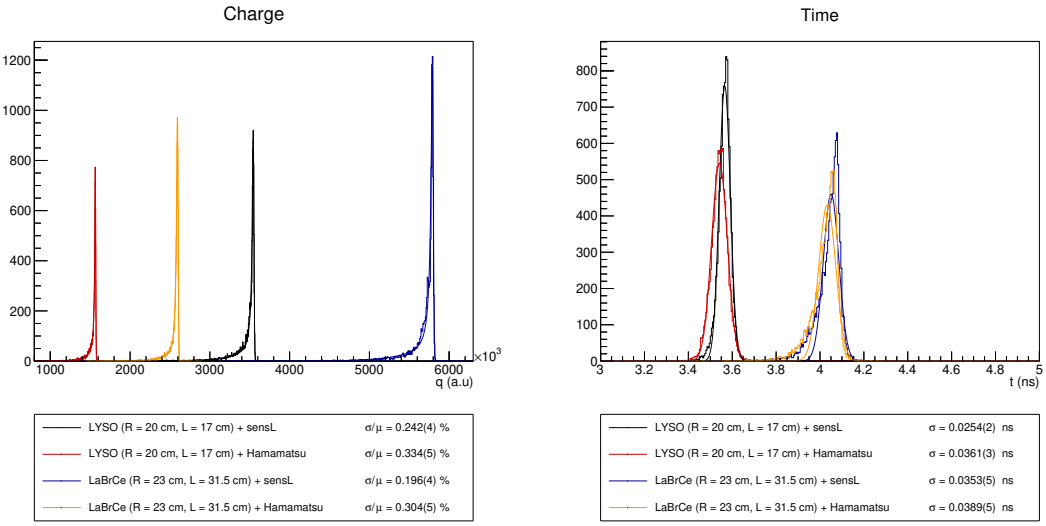

(a) Charge

(b) Time

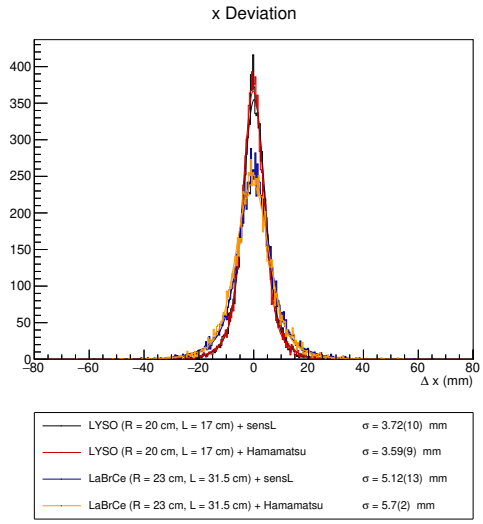

(c) x-Position

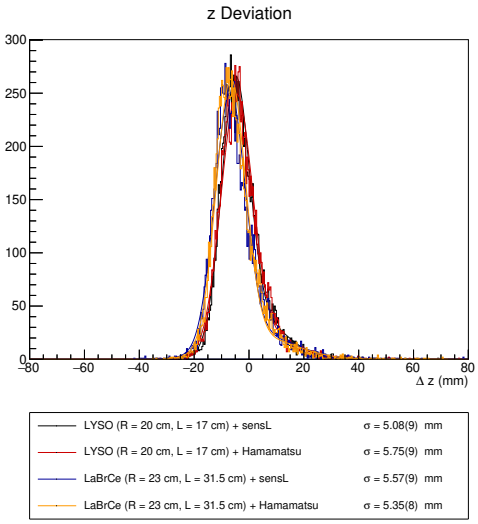

(d) z-Position

Figure 7.18: Resolutions obtained for crystals with $L = 15X_0$ and $R = 10R_{\mathrm{M}}$.

Configuration	Resolution σ_1/μ	Peak Position μ	$\sigma_1/\sqrt{\mu}$
LYSO + sensL	$(0.242 \pm 0.004)\,\%$	3.54×10^6	4.56 ± 0.08
LYSO + Hamamatsu	$(0.334 \pm 0.005)\,\%$	1.56×10^6	4.18 ± 0.07
$LaBr_3$(Ce) + sensL	$(0.196 \pm 0.004)\,\%$	5.79×10^6	4.72 ± 0.09
$LaBr_3$(Ce) + Hamamatsu	$(0.304 \pm 0.005)\,\%$	2.59×10^6	4.90 ± 0.08

Table 7.4: The products of resolution and peak position. If the resolutions obtained were limited by the light yield only, the values in the last column were constant. The variations are too large for the light yield to be the only limiting factor.

resolutions increase as the peak position in terms of collected charge increases - independently of the crystal considered in that specific configuration.

In the ideal case where the light yield is the only limiting factor, the resolution is determined by the photon statistics and thus follow an $N^{-\frac{1}{2}}$ dependency. As the charge is expected to be proportional to the number of photons, the value of $\sigma/\sqrt{\mu}$ should turn out constant if the light yield is the dominant limitation.

The obtained values displayed in Table 7.4 however exhibit quite some fluctuations amongst each other. A standard deviation of around 0.27 is observed between them. This is roughly 3.3 times the uncertainty in each value, suggesting that at least some of them are inconsistent with a constant value and the hypothesis that all the variations originate from the photon statistics only.

Looking at the time distribution in Figure 7.18b, one can observe on the one hand that the position of the distributions for LYSO and $LaBr_3$(Ce) are shifted by a constant offset. This offset comes from the theory based formula used for the time reconstruction and is of no significance as it will be taken care of by the time calibration in any detector.

Furthermore, the $LaBr_3$(Ce) distribution exhibits a tail towards lower values as already observed in earlier time distributions for this material. They are none the less fitted with the same function as the LYSO to get comparable values, keeping in mind that an advanced analysis algorithm may increase the time resolution for $LaBr_3$(Ce). Keeping this in mind, these two crystals provide similar resolutions for the time.

Considering the x position reconstruction, LYSO seems to perform better yielding resolutions below 4 mm. $LaBr_3$(Ce) on the other hand provides resolutions just above 5 mm. The first notion to explain this goes in the same direction as what has been seen in the previous chapter on the position reconstruction: Although a linear approximation is used, there are significant higher order terms that were neglected.

The residues are plotted in Figure 7.19. Although one can observe that some non-linear terms remain, they cannot explain the observed difference in resolution. In fact, the data for $LaBr_3$(Ce) provides a larger spread in the residues even when considering a specific value for the centre of the front charge distribution. The charge distribution obtained from the back behaves in a very similar fashion.

Thus the nature of this deviation in terms of x position resolutions remains unclear for the moment. Likely not due to the finite size of the shower as the Molière radii are closer together than the radiation lengths. If this were the true nature, a similar effect should be observable from the z deviations. These however do not show any preference in terms of scintillator material or sensors used - at least not in the studied configurations.

To sum up the ideal case, cerium doped lanthanum bromide provides better charge resolution in the studied configuration. LYSO however provides a better resolution in terms of position perpendicular to the impinging direction. The charge resolution directly determines the energy resolution ΔE_γ in Equation 7.9. The position resolution enters together with positron variable resolutions through the resolution $\Delta\Theta_{e\gamma}$ in the relative angle between them.

Both terms enter the background rate for the $\mu \to e\gamma$ search in quadratic form so it is too early to conclude which material performs better in the very end for MEG-type experiments. For other experiments however, one of the resolutions may easily outweigh the other. The Majoron search for example aims to find evidence for a decay $\mu \to e + X$ where X represents an yet unknown, undetectable particle. It's basic signature consists of a peak on top of the Michel energy spectrum. At this point, only the energy resolution is of importance as only the electron can be measured. Thus it is too early for a final conclusion about the material best suited.

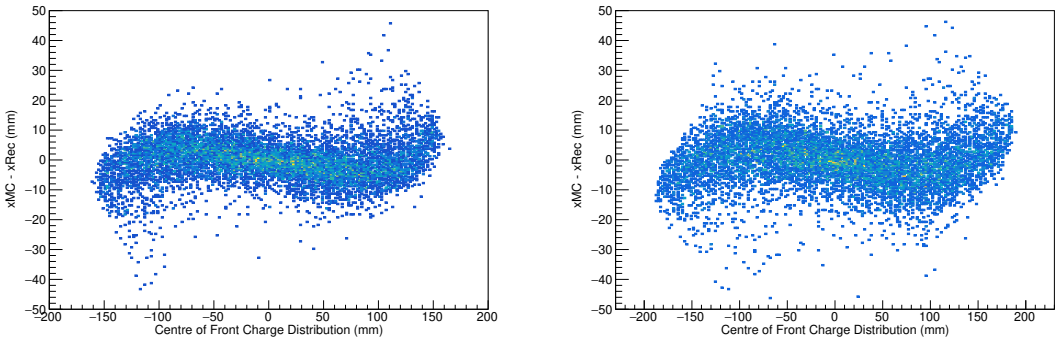

(a) LYSO ($L = 17\,\mathrm{cm}$, $R = 20\,\mathrm{cm}$)

(b) $LaBr_3(Ce)$ ($L = 31.5\,\mathrm{cm}$, $R = 23\,\mathrm{cm}$)

Figure 7.19: Deviations of the reconstructed x-Position from the position of first interaction in dependencies of the centre of the charge distribution on the front $\bar{x}_f$. Similar dependencies are observed for the back side.

Part III

The Search for New Physics with the MEG II Apparatus

Chapter 8

The Search for the Fifth Force

8.1 Description of the Large Chamber Setup

In order to perform the fifth force search with the MEG II apparatus, minor adaptations are required. First of all, a different target needs to be manufactured. While different approaches were considered, only the large chamber setup is presented here. This chamber replaces the lithium borate target used for calibrations and the corresponding insertion system.

An alternative approach to a carbon fibre chamber about the same size as the proton beam pipe is a much larger chamber of about 13 cm to 14 cm radius and 30 cm total length. This configuration is depicted in Figure 8.1. The carbon fibre structure is planned to have a width of about 200 µm. The target structure is mounted on an arm inside the chamber.

The inside volume is directly connected to the proton beam pipe from the Cockcroft-Walton (CW) accelerator and consequently evacuated. The outer radius of the construction allows for a minor separation from the inner Mylar foil of the CDCH. This gap is filled with air. The insertion system usually used in combination with the CW beam line is completely removed. This automatically forces any measurement with this setup to take place during the long maintenance shutdowns of the main accelerator at the beginning of each year yet reduces the amount of material for multiple-scattering of electrons and positrons between target and CDCH.

The target structure is mounted inside the large vacuum chamber. It is kept in position by an approximately 15 cm long arm at COBRA centre. The target itself consists of a thin layer of lithium oxide placed on a substrate foil. The substrate foil is supported by a frame with about 1 cm width and an inner radius of around 3 cm. The material for the substrate, the frame and the target arm are either copper or aluminium. Copper is favoured in terms of heat conductivity while aluminium is preferable in terms of avoiding multiple-scattering of particles.

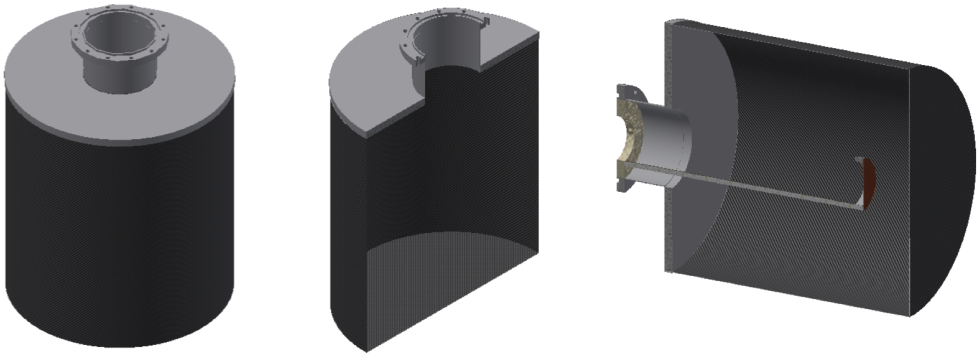

Figure 8.1: The Large Chamber setup. A carbon fibre chamber with a radius of about 14 cm and a length of 30 cm contains the Lithium oxide target. It is attached to an Aluminium ground plate, that serves as adapter to the proton beam line from the CW accelerator. Image provided by A. Papa [104].

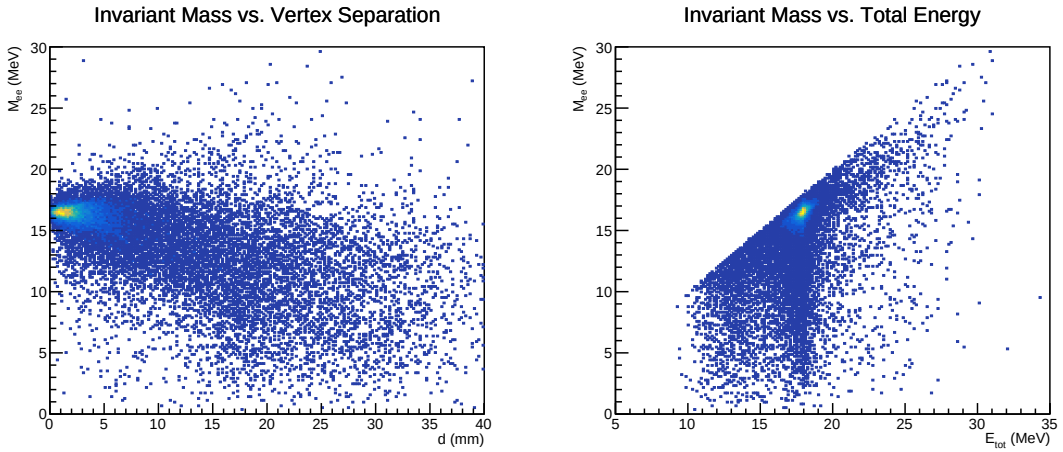

(a) Before cuts are applied

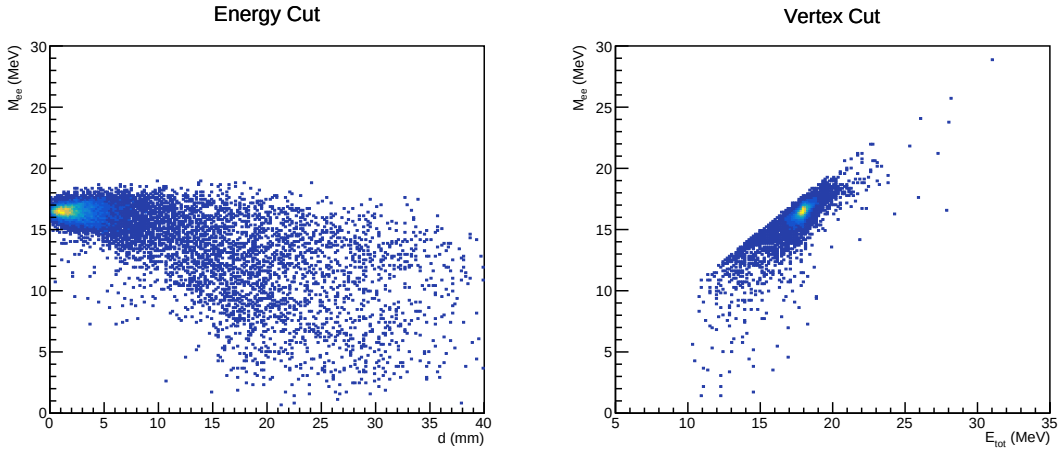

(b) Cuts applied

Figure 8.2: Invariant mass versus vertex separation d (left) and invariant mass versus total energy (right). The cuts applied are requesting that the total energy of the pair is within 1 MeV of the resonance energy (18.15 MeV) (left) respectively requesting that the two vertices are no further apart than 6 mm (right).

The details of the target geometry are worked out based on the simulations presented in the following sections. Apart from the different materials, the thickness of the lithium oxide target as well as the thickness of the support foil have to be determined. Moreover, the optimal orientation with respect to the MEG II detector has to be found.

8.2 Event Selection in Simulations

This section describes the criteria used to select the reconstructed electron-positron pairs to be used in the further analysis. Two cuts are used. The first one requests that the total energy of the pair corresponds to the total energy of the beryllium resonance. The second one requests that the tracks of the two particles intersect on the target plane.

The signal to be reconstructed consists of an electron-positron pair emitted from the decay of an X-Boson. Their invariant mass corresponds to the X-Boson mass expected to be around 16.7 MeV. A well reconstructed event consequently consists of an electron track and a positron track that originate from the same vertex. Additionally, the sum of their respective energies has to add up to the energy of 18.15 MeV of the excited beryllium resonance.

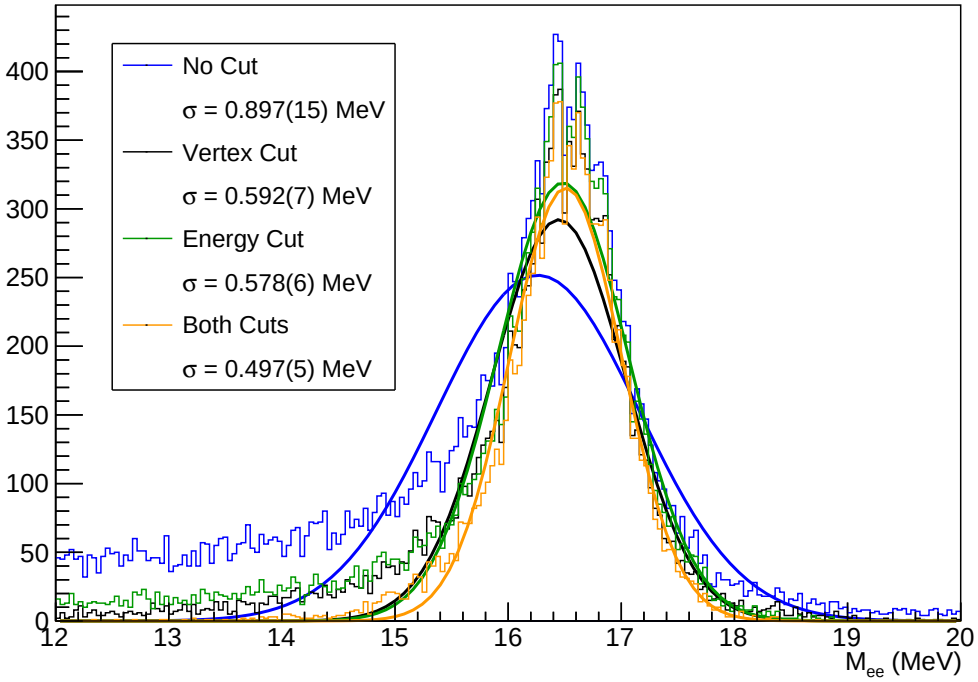

Figure 8.3: Invariant mass M_{ee} distribution for different cuts. "No Cut" refers to the minimal request of an electron and a positron track reconstructed with some reasonable energy. The "Vertex Cut" refers to the request that the intersections of the tracks with the target plane are closer than 6 mm. The "Energy Cut" enforces that the total reconstructed energy lies between 17.15 MeV and 19.15 MeV. "Both Cuts" refers to enforcing both conditions in the data selection.

From the pair production through the decay of the X-boson to the fully reconstructed event, several issues may occur: From the scattering of a particle to the wrong reconstruction of a track. such bad events contribute to the background and should be discarded. The most obvious and straight forward requirement for a good event is the reconstruction of an electron and a positron track with an energy suitable for a particle emitted in such a process.

Plotting the reconstructed invariant mass M_{ee} versus either the reconstructed total energy E_{tot} or the vertex separation d of the two reconstructed tracks yields Figure 8.2a. In both cases there is a clear peak representing well reconstructed events with the expected invariant mass (16.7 MeV) and a vanishing vertex separation or a total energy of 18.15 MeV respectively.

Figure 8.2b displays the same distributions again when requesting that the total energy is within 1 MeV of the resonance energy at 18.15 MeV for the left plot showing invariant mass versus vertex separation and that the vertex separation is below 6 mm for the right plot showing invariant mass versus total energy. It becomes obvious that the two cuts are complementary and allow for an efficient rejection of badly reconstructed events.

The effect on the reconstructed invariant mass distribution is displayed in Figure 8.3. Each distribution is fitted with a Gaussian, which allows for a crude and fast comparison neglecting detailed and specific assumptions about a single distribution. Through considering all events for which a positron and an electron track has been reconstructed with a reasonable energy each, the blue distribution (No Cut) is obtained. This distribution has significant tails, especially towards lower invariant masses.

Both cuts work to reduce the tails to some extent, yielding the black (Vertex Cut) curve, for demanding a vertex separation below 6 mm, or the green (Energy Cut) curve for demanding that the sum of the energies corresponds to the energy of the resonance. Applying both cuts simultaneously yields the orange distribution. This removes the tails on both sides almost completely while the peak is largely untouched. Very similar observations are made for all configurations simulated in this and further investigations.

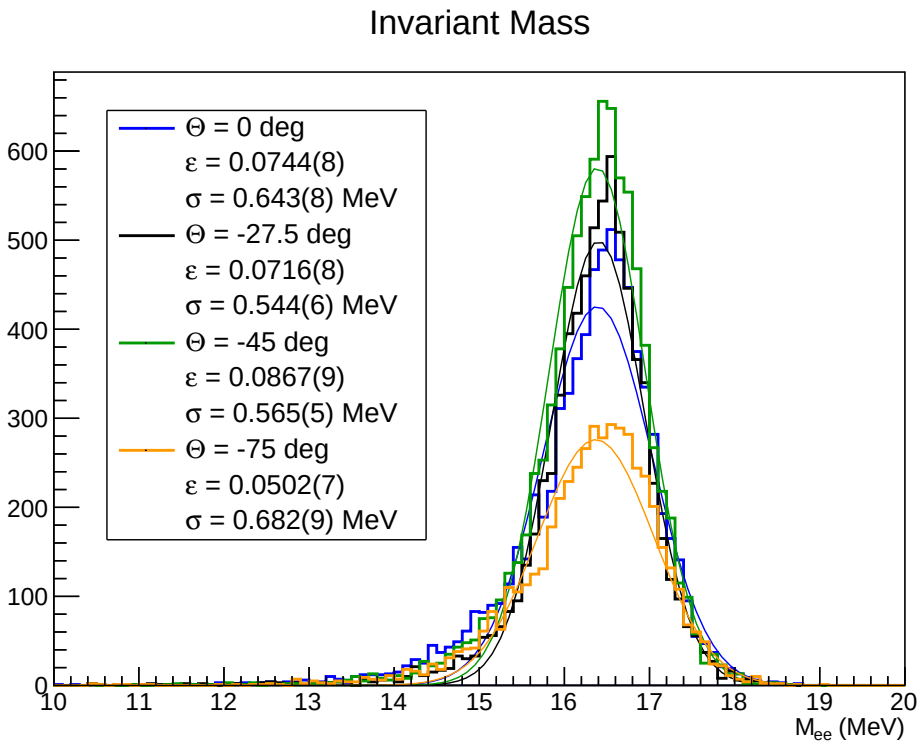

(a) Invariant Mass

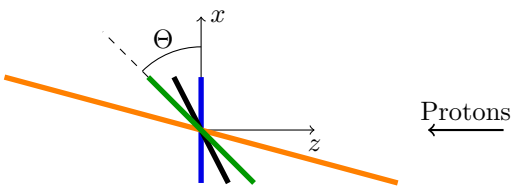

(b) Target Orientation

Figure 8.4: Invariant mass distributions for different slanting angles. The efficiency ε refers to the fraction of events that get fully reconstructed and thereafter pass all cuts. The standard deviation σ of the Gaussian fit is quoted here as expected resolution.

8.3 Evaluation of Different Target Orientations

In this section, the geometric orientation of the target is discussed. Two quantities are considered relevant for this. First there is the detection efficiency and second the expected invariant mass resolution near the expected X-boson resonance.

The target orientation offers two degrees of freedom. On the one hand, an appropriate slanting angle with respect to the beam axis (z-axis) has to be found. On the other hand, the slanted target can be rotated around the beam axis itself. For each orientation, an elliptical target configuration is chosen, such that the lithium oxide layer appears as a circle of 2 cm radius as seen along the proton beam. This implies that the eccentricity of the target increases the more slanted it is. The active part of the target is considered to be made of a 50 µm copper substrate with 100 µm of lithium oxide deposited on it.

The two parameters of interest are the efficiency and the resolution in terms of invariant mass. The efficiency accounts for the amount of events for which both, the electron and the positron, reach the drift chamber and get reconstructed in an acceptable manner. The resolutions indicate, how well the events can be reconstructed.

The obtained spectra for different target slanting angles are represented in Figure 8.4. The

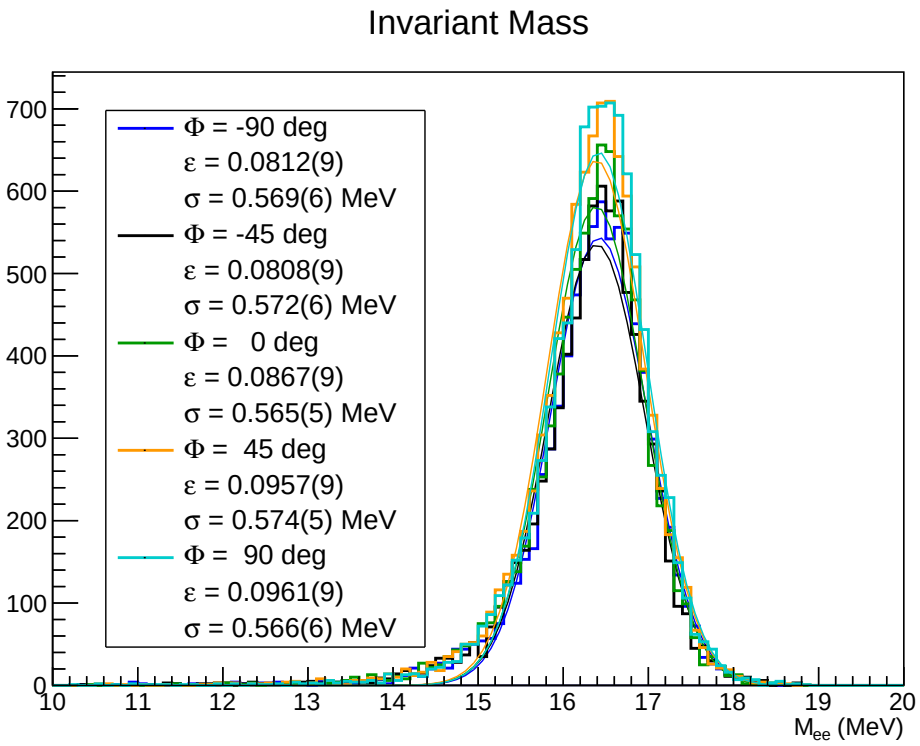

Figure 8.5: Distributions obtained for different target rotations. The rotation $-90°$ refers to a target where the irradiated side points upwards, $90°$ refers to a downward looking target. A rotation of $0°$ describes a target facing away from the liquid xenon detector. The other two cases refer to the intermediate situations. Efficiencies ε refer to the events passing all cuts and the standard deviations σ are taken from a Gaussian fit.

target is rotated around the Y-axis and the protons are going to be shot at the target from the positive z-axis as indicated in Figure 8.4b. The positive x-axis faces away from the liquid xenon detector used in the MEG II experiment.

The efficiencies ε are calculated as the fraction of events that get suitably reconstructed and pass all cuts. The resolutions σ are extracted as the standard deviations obtained from a simple Gaussian fit. The results suggest that a slanted target is preferred in terms of efficiency and resolution over a target aligned along the xy-plane. The situations worsens again if an angle too large is chosen. An angle between $27°$ and $45°$ appears to be most suitable. To simplify everything, a slanting angle of $45°$ is chosen henceforth.

The simulation results about the target rotation around the z-axis are shown in Figure 8.5. The target rotation Φ refers to the rotation with respect to the case considered in the slanting angle studies. The case $\Phi = -90°$ refers to the situation, where the surface irradiated from positive z-direction faces in upward direction. The case $\Phi = 0°$ corresponds to the case where it is facing away from the liquid xenon detector and the case $\Phi = 90°$ refers to a target facing downwards.

Based on these studies, hardly any effect in terms of invariant mass resolution is observed. The efficiencies however clearly prefer a target facing downwards. The most likely explanation for this behaviour is the fact, that on the upper part of the drift chamber, there are two sectors missing, i.e. not able to detect any tracks. Being unable to detect tracks facing that direction immediately worsens the detection efficiency and consequently the overall efficiency. Based on these results, the decision to go with a target slanted by $45°$ facing downwards is made. This configuration is considered henceforth.

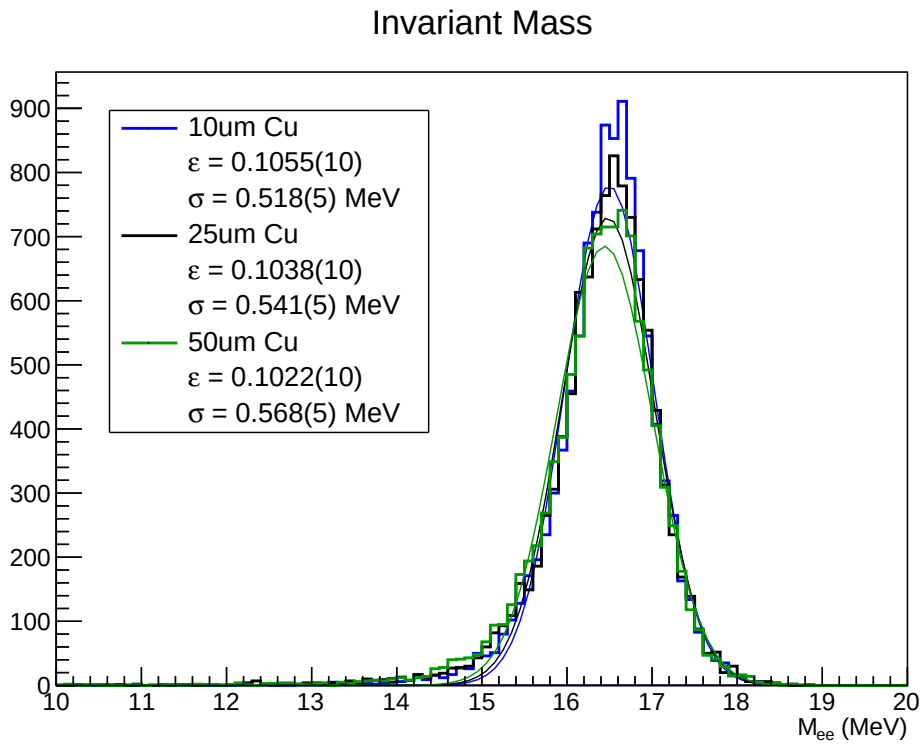

Figure 8.6: Distributions obtained for different copper substrate thicknesses. For all configurations, a 10 µm lithium oxide layer as active part is considered. Efficiencies ε and standard deviations σ are shown for each of them.

8.4 Selection of the Target Substrate

This section discusses the selection of the material to place the lithium oxide layer on. Aluminium for its lower density and copper for its better heat conductivity are considered.

With the fixed target orientation, a decision for a suitable substrate has to be made. For this purpose, different thicknesses of the substrate are considered. The simulations presented here evaluate the effect of the target thickness on the invariant mass resolution as well as the efficiency.

The impact on the mechanical aspects as well as the impact on the heat conductivity are dealt with in separate studies [105]. In a short summary, from these points of view, a thicker target support structure made of copper is clearly preferred. The lack of an efficient way to remove the heat produced by the proton beam on the target will result to stress in the target and eventually to its destruction.

From the reconstruction point of view, the very opposite is preferred. This can be seen from Figure 8.6, where the simulated results for a 10 µm Lithium Oxide deposited on a copper substrate of varying thickness is displayed. Both, reconstruction efficiency and achievable resolution in terms of the invariant mass, improve the thinner the target. Not depicted in this figure is the fact, that the simulations would prefer an aluminium substrate over one made of copper.

Comparing the limitations from the mechanical point of view to these results based on the particle physics simulation, a 25 µm copper substrate is chosen as the best option available. Moreover, a thin lithium oxide layer of around 10 µm is preferable from the reconstruction point of view. Dedicated simulations on the interaction of the incoming protons suggest that an even thinner target of about 5 µm thickness is desirable [105].

8.5 Estimation of the Runtime

This section describes the resampling process to obtain the expected distributions under the assumption of IPC background and an appropriate X-boson admixture. It further describes the fitting procedure of these distributions and the extraction of the significances. This is finally converted to an estimation of the run time needed to confirm or refute the existence of this new X-boson.

The data obtained from X-Boson and IPC simulations in the invariant mass M_{ee} range between 12 MeV and 20 MeV and with a relative angle Ψ_{ee} between the electron and the positron track above 90° is arranged in bins with a size of 400 keV in terms of invariant mass and 5° in terms of relative angle. These bin sizes are selected to be just below the expected resolutions.

Based on the known branching ratios and the detection efficiencies obtained from simulations, the chance that an observed event with an invariant mass M_{ee} between 12 MeV and 20 MeV with a relative angle above 90° is an X-Boson event is estimated to be around 4.6 %. This serves as the basis for the resampling techniques used to estimate the runtime required to observe an excess with at least 5σ significance.

For each number of events to be investigated, value pairs (M_{ee}, Ψ_{ee}) are picked randomly from the above mentioned distributions with the estimated probabilities. These values are evaluated using identical binning as described above. Three distributions are considered individually, namely the distribution of the invariant mass on its own, the distribution of the relative angle on its own and the correlated distribution of the two. The whole procedure is repeated 100 times for each number of events selected. One example of these distributions is shown in Figure 8.7. While the signal excesses are easy to spot in the 1D distributions, a closer look is needed to observe it around 17 MeV and just below 140° in the correlated distribution.

In order to fit the background, the signal window has been set to a range between 120° and 160° in terms of relative angle and between 15.2 MeV and 18 MeV in terms of invariant mass. Bins that include data in this range are excluded from the background fit. In this simple model, only one parameter is used to adjust the scale of the IPC distribution as obtained through the simulation to the obtained mixed distribution. The distributions for invariant mass, relative angle and the correlated distribution are fitted and evaluated individually. To fit this one parameter, a likelihood method based on Poisson likelihoods for each bin is used. In this specific case with just one scale parameter, this boils down to counting events in all background bins and determining the ratio.

The significance s of an excess is estimated based on the formula

$$s = \frac{N_{\text{signal}}}{\sqrt{N_{\text{total}}}} = \frac{\sum N_i - N_i^{\text{IPC}}}{\sqrt{\sum N_i}} = \frac{\sum R_i}{\sqrt{\sum N_i}} \tag{8.1}$$

where N_{total} refers to the total number of detected events, $N_{\text{signal}} = N_{\text{total}} - N^{\text{IPC}}$ refers to the suspected amount of signal events, corresponding to the total number of events minus the expected number of background events in the excess region. These numbers are obtained by summing the number N_i of events and the expected number N_i^{IPC} of IPC events in each bin over all bins of the excess. Note that the difference $N_i - N_i^{\text{IPC}}$ corresponds to the residual R_i estimated by the fit.

In the 1D distributions of the invariant mass of the pair respectively the relative angle between the electron and the positron, the most significant excess is searched, i.e. the set of neighbouring bins that maximises the value of the significance. An example is shown in the two bottom plots of Figure 8.8 where the blueish filled region marks the most significant excess observed. This is done for each of the distributions individually and independently for each of the 100 tries. The average in terms of significance is then quoted as the expected significance for a certain number of events.

For the 2D distributions, an additional 100 tries were undertaken at the highest number of events to be resampled. These are used to define the 2D region of bins for which the significance has to be estimated. For each of the individual runs, the region of the most significant excess is estimated. For each of these 100 additional tries, a separate region is obtained. The region to evaluate the significance in the analysis is then defined by the bins that appeared in at least 50 % of the tries to be contributing to the most significant excess.

This evaluation region is then applied to the same data as used for the analysis of the 1D distributions. An example is shown in Figure 8.9. On the left side, the resampled data is shown, binned into bins of 400 keV width in terms of invariant mass and 5° in terms of angle between the electron and the positron. On the right side, the residuals after subtracting the best background

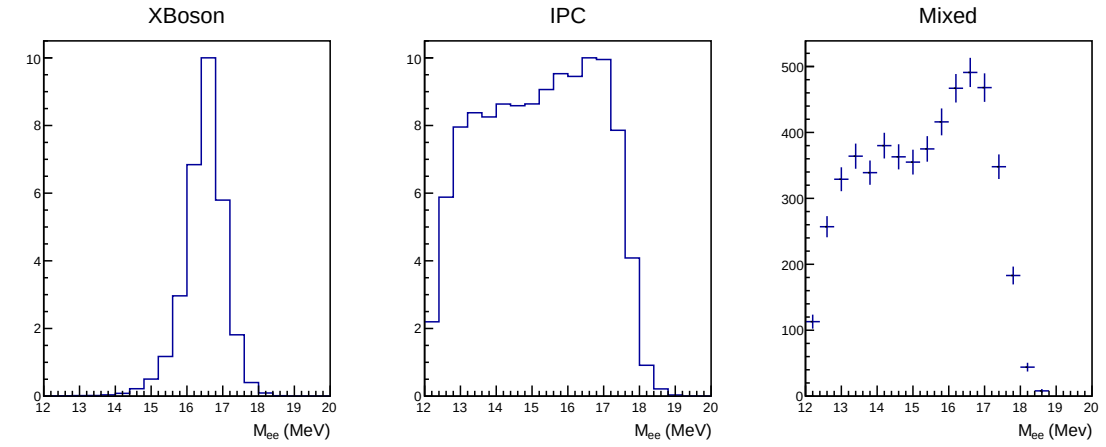

(a) Invariant Mass

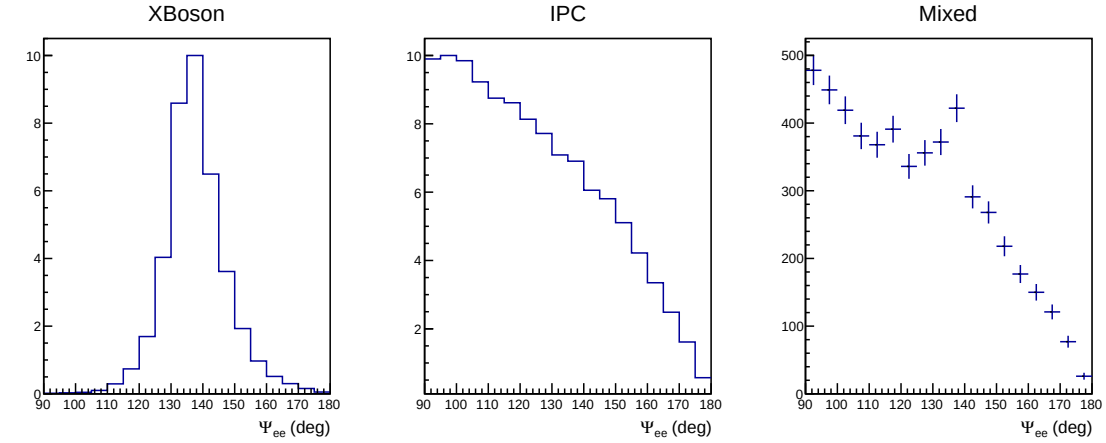

(b) Relative Angle

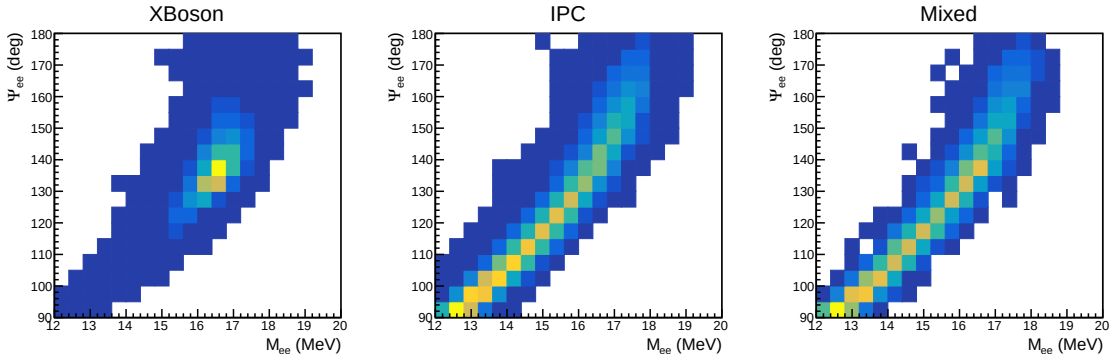

(c) Correlated

Figure 8.7: Distributions in the resampling process. An example using 5300 events is shown. The X-Boson and IPC distributions refer to the distributions obtained from the respective simulations and are independent of the number of events. The Mixed distributions are the product of the resampling. Poisson errors are shown.

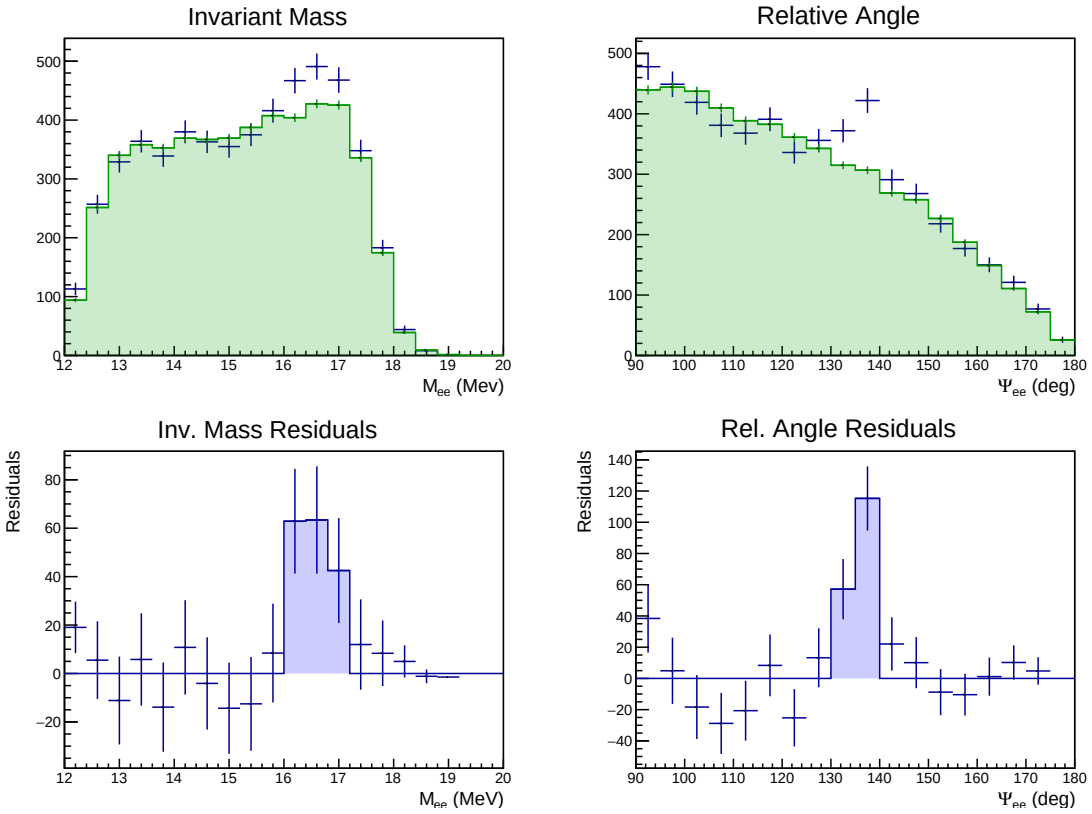

Figure 8.8: The resampled distribution obtained by mixing X-Boson and IPC events (blue) with the best background fit (green) for invariant mass and relative angle are shown on top. The residuals are shown on the bottom. The most significant excess is highlighted in blue.

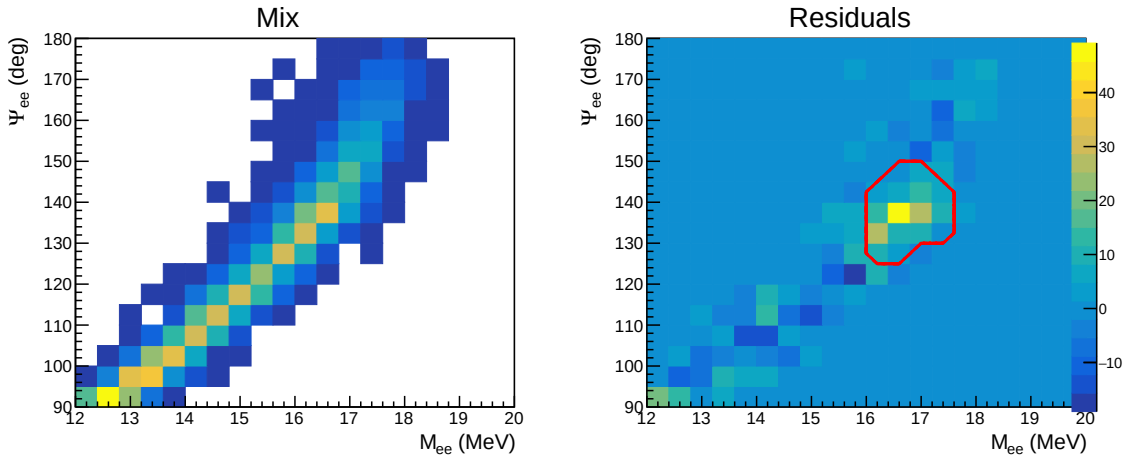

Figure 8.9: Distribution of the correlated data on the left side, residuals after subtracting the best background fit on the right side. The red contour marks the evaluation region used to extract the significance of the X-Boson signal.

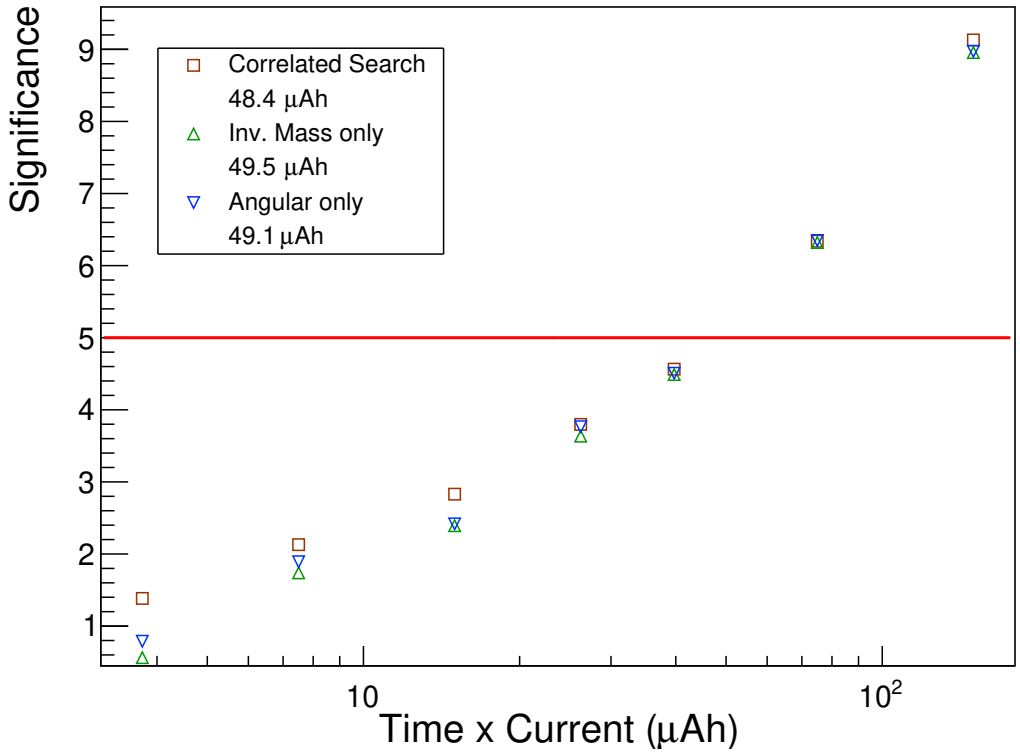

Figure 8.10: Expected significance of the X-Boson excess as function of the run time.

fit is shown. A clear excess can be seen around 17 MeV invariant mass and 140° relative angle, corresponding to the signature of the 4.6 % admixed X-Boson events. The red contour marks the evaluation region for the extraction of the significance.

Using the number of hypothetically reconstructed IPC-events used in the resampling process and the detection efficiency for these events, the total number of IPC events generated can be estimated and turned into a runtime approximation using an estimated rate for IPC events. The IPC rate is estimated by M. Meucci to be around 28.9 Hz when running the CW accelerator at a proton beam current of 1 µA [105]. Previous experiments with the same accelerator and very similar targets however showed, that the event rate appears to be by a factor 3 lower than expected for unknown reasons [106]. To be on the save side, an IPC rate of 10 Hz is assumed when turning event numbers into runtime estimates.

The look-elsewhere-effect is considered by turning the significance obtained from the 1D histograms into a probability to observe an excess as large as the one observed or larger at this given point. Based on this probability, the probability to observe at least one excess as large as this anywhere in the distribution is estimated and then turned back into a significance. No such step is taken for the correlated search, as the evaluation region was set beforehand based on different resampled datasets and it was just checked, if at that given position an excess can be found.

The significance in dependence of the run time is shown in Figure 8.10. Note that the run time is given in µA h, corresponding to a measurement time while running at a given proton beam current delivered by the local CW accelerator. Independent of the analysed distribution, the estimated measuring time is around 50 h while running the CW accelerator at 1 µA. This time refers to the measuring time of physics runs only and does not include calibration runs and time to set the experiment up.

Accounting for these tasks, the time estimate increases to a time of the order of a week or two. This is still much less than the three months maintenance scheduled for the high intensity proton accelerator facility at PSI in the beginning of 2022. Thus providing an independent measurement of the observed beryllium anomaly is feasible at the beginning of next year.

Chapter 9

The Search for the Majoron

9.1 Implementation of Theoretical Models

This section describes the input provided by the theorists, its implementation in the MEG II simulation code and the subsequent validation of the generator.

In order to estimate the potential of the MEG II apparatus for Majoron searches, proper theoretical models are required. For this reason, a close cooperation with the PSI theory group was formed. Eventually, they performed the calculations and provided tables for the fully differential cross-section for the Michel decay at Leading Order (LO), Next to Leading Order (NLO), Next to Next to Leading Order (NNLO) and NNLO plus leading logarithms (NNLOLL) as well as theoretical models for the positron spectrum of the $\mu \to eX$ decay under different m_X hypotheses [66].

These tables contain the functions $F(E)$ and $G(E)$ representing the isotropic respectively the anisotropic part of the probability density function proportional to

$$p(E, \cos\theta) \propto F(E) + PG(E)\cos\theta \tag{9.1}$$

where θ refers to the MEG II polar angle and $P = -0.85$ is the polarisation of the incoming muon beam [107].

The predicted energy spectra for Michel positrons are shown in Figure 9.1. Differences become most obvious towards the kinematic endpoint. While the difference between LO and NLO is clearly visible, it requires a closer look at the kinematic endpoint as shown on the right in Figure 9.1b to see the differences between NLO and the more precise predictions. This is the region of highest interest to search for low mass X candidates. As shown further below, fake signals can easily be generated if the theoretical predictions are insufficient in this region.

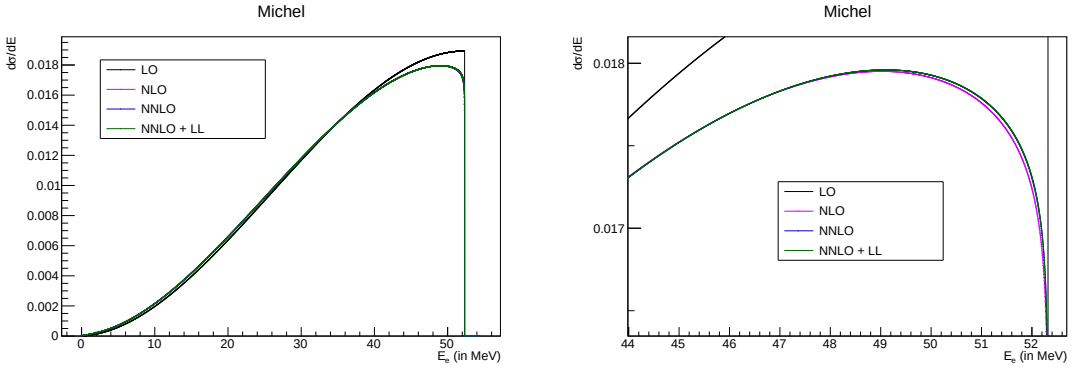

(a) Full Spectrum

(b) Zoom

Figure 9.1: Theoretical energy spectrum for Michel positrons. Predictions for Leading Order (LO), Next to Leading Order (NLO), Next to Next to Leading Order (NNLO) and NNLO plus leading logarithms (NNLOLL) are shown.

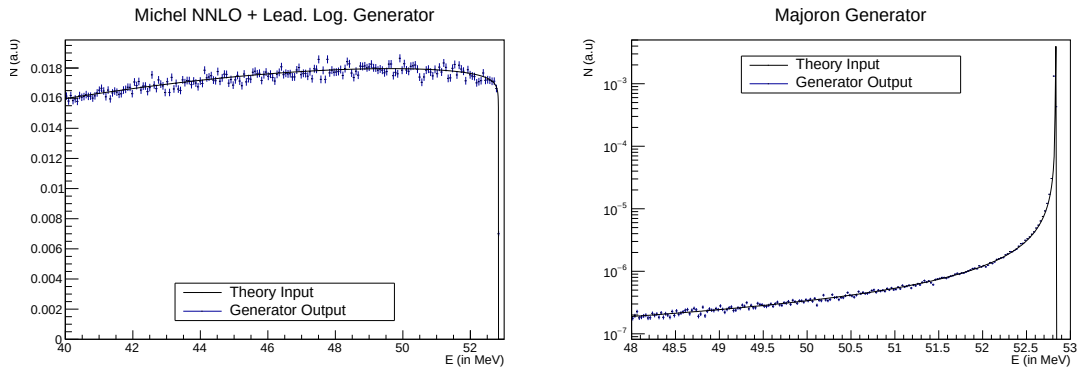

(a) Michel NNLOLL

(b) Majoron NLO

Figure 9.2: Theoretical energy distribution and distribution obtained from event generator.

The generator takes care of reading these functions from the corresponding file and taking appropriate adjustments for bin sizes as well as the desired energy and angular ranges the particles should be generated in. The energy distribution for the Michel NNLOLL events as well as Majoron events with $m_X = 1\,\mathrm{MeV}$ obtained by the event generator is shown in Figure 9.2 together with the theoretical predictions as validation. As can be seen easily, the generator output matches the theoretical input perfectly well up to statistical uncertainties.

9.2 Characterisation of the Detector Response

The detector response is characterised, discussed and validated that self-consistent results are obtained. Based on the response an appropriate mass range is highlighted, where a reasonable Majoron search is feasible. Moreover, the responses to the Majoron model, the NLO Michel model and the NNLOLL Michel model are compared. Last, potential systematic effects are discussed.

To characterise the detector response, there are two main quantities of interest. First, there is the detection efficiency. Second, there is the resolution. In order to estimate both quantities for further analyses, the full detector simulation of the MEG II experiment was used. Given the detector geometry, only what is known as the MEG II interest region ($70° < \theta < 110°$, $-60° < \phi < 60°$) is considered in the following simulations. Unless stated otherwise, simulations associated with the NNLOLL calculations for the Michel decay are used.

As this search will only make use of single positron tracks, the timing requirements are not nearly as crucial as for the $\mu \to e\gamma$ search. Thus a well reconstructed track for this search requires a reasonably reconstructed vector momentum and a cluster in the timing counter. The timing counter cluster is crucial as it is required for triggering purposes. At this stage a proper matching between CDCH track and pTC cluster is not necessary.

By comparing the number of events that match the above reconstruction criteria with the total number of events that was simulated for a certain positron energy, the efficiency is extracted as the ratio of the two numbers. The efficiency as function of the positron energy is drawn in Figure 9.3.

One can observe an excellent efficiency towards the kinematic endpoint above 48 MeV. The detection efficiency for positrons below 42 MeV is poor by design. This behaviour is beneficial to the $\mu \to e\gamma$ search as it rejects background Michel positrons on a detector level and thus reduces pileup in the detectors and the occupancy of the electronics.

If aiming for dedicated measurements in a different positron energy range, this region of high efficiency can be adjusted by tuning the COBRA magnetic field accordingly. For this proof of principle analysis, only the default magnetic field and positron energies above 42 MeV are considered.

In addition, the Majoron mass m_X corresponding to a given positron energy E_e is shown in Figure 9.3. Comparing this curve to the efficiency, on can already see that the MEG II experiment is more susceptible to lower masses in the range between $0\,\mathrm{MeV/c^2}$ to $30\,\mathrm{MeV/c^2}$. The sensitivity will degrade from $30\,\mathrm{MeV/c^2}$ to $50\,\mathrm{MeV/c^2}$ and searches for even higher m_X will be basically impossible.

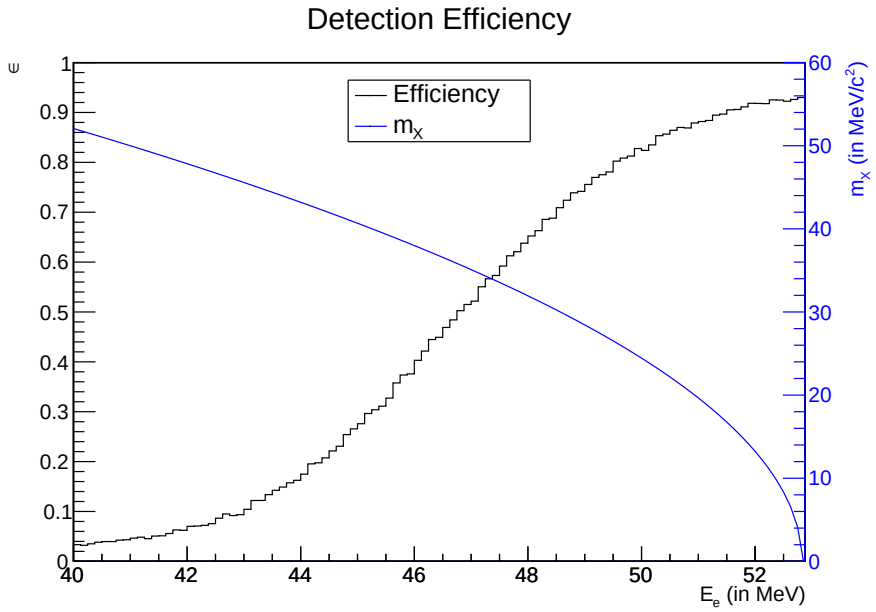

Figure 9.3: Detection efficiency as function of the positron energy (left axis). The Majoron mass m_X corresponding to that positron energy is shown in blue (right axis).

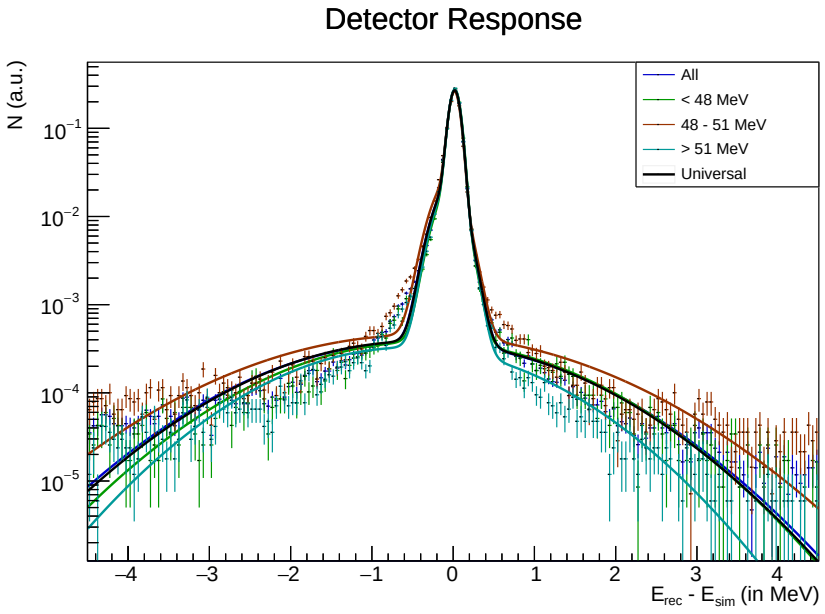

Figure 9.4: Difference between generated and reconstructed positron energy. The "Universal" curve is the average over all fits, as no significant deviations were observed.

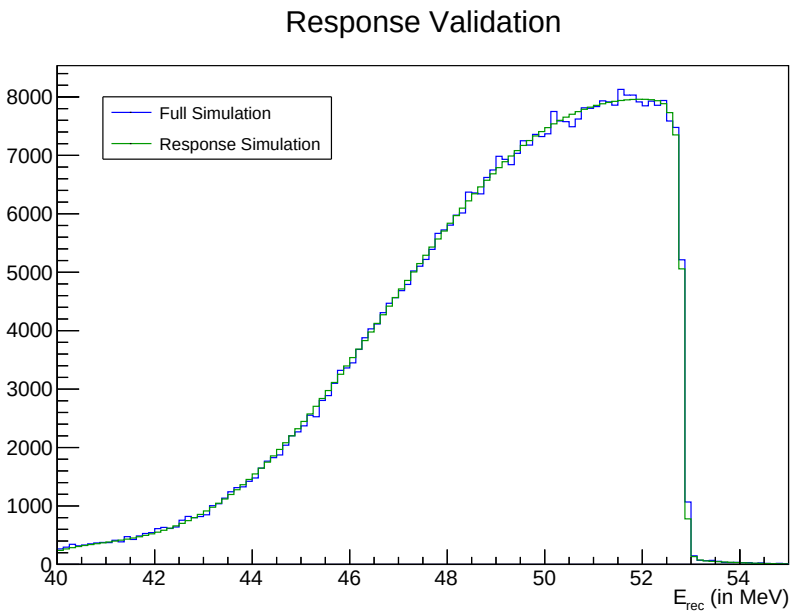

Figure 9.5: NNLOLL spectrum obtained by full detector simulation compared to the convolution of the theoretical function with the detector response functions.

To estimate the positron energy resolution, the difference between generated positron energy E_{sim} and reconstructed positron energy E_{rec} is calculated for each well-reconstructed event. This analysis was performed on the whole energy range as well as three subsets with energies below 48 MeV, from 48 MeV to 51 MeV and above 51 MeV. These cuts were selected to obtain a roughly similar amount of data in each subset.

The resulting distributions are shown in Figure 9.4. Each of the four histogram is fitted independently with the sum of three Gaussians. The black curve (labelled Universal) is obtained by averaging over the individually fitted results. While the central part containing the vast majority of the events is rather well fitted, the tails are not described well by the third gaussian.

To ascertain the validity of the estimated efficiencies as well as the fitted detector resolution functions, these detector response functions were convoluted with the theoretical NNLOLL predictions for the Michel positron energies. The results are presented in Figure 9.5. The convoluted function was scaled such that the corresponding integrals sum up to the same number of events.

The two distributions match to a large extend. Even the tail at the kinematic endpoint towards the unphysical region above 53 MeV is decently reproduced by the convolution. The only real shortcoming can be found at the kinematical endpoint itself. For these two bins a potential underpopulation can be observed for the convoluted function. Thus, sensitivity estimates based on these bins should be considered only very carefully.

Given the fact that the analysis software for the MEG II apparatus is still in its final phase of development and the details of the implemented response functions for each subdetector with the final electronics set up will only be measured later this year in the engineering run, this is deemed as sufficient to get a preliminary estimate of the order of magnitude of the sensitivity.

In a further step, the detector responses of the NLO Michel model used as default and of the predicted 1 MeV/c^2 Majoron signature are compared. By far the most crucial observation is made, when the obtained NNLOLL response is fitted with the NLO response and the residuals are then compared to the Majoron response. This is shown in Figure 9.6.

For easier comparison, both histograms are scaled to the same amplitude. It is obvious that the residuals obtained by fitting the NNLOLL response with the NLO response look quite similar to a potential Majoron signal. This underlines the importance of the improved NNLOLL calculations, which are expected to model the Michel spectrum more accurately than the NLO model. Not having the NNLOLL model and fitting the measurement with the expected NLO response could easily create a fake signal if theoretical errors are not considered properly in the analysis. If considered properly, the sensitivity would be degraded drastically.

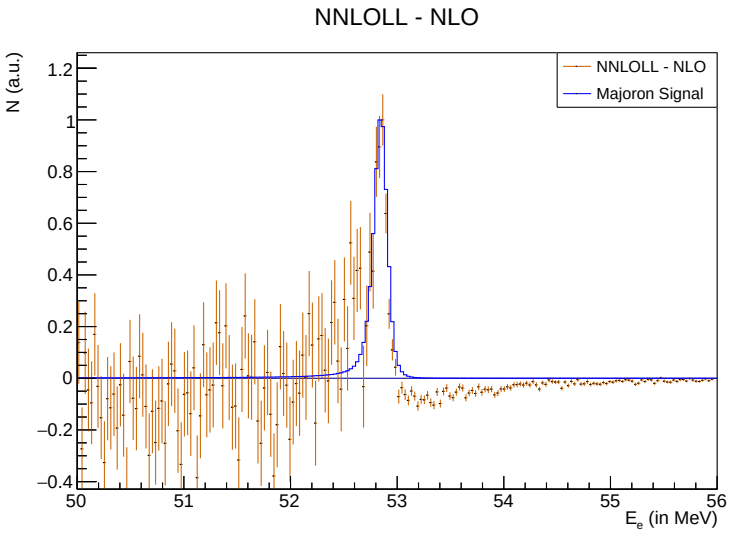

Figure 9.6: Residuals when fitting the NNLOLL response with the NLO response (NNLOLL - NLO). They are compared to the expected Majoron signal for $m_X = 1\,\text{MeV}$. The distributions are scaled to the same amplitude.

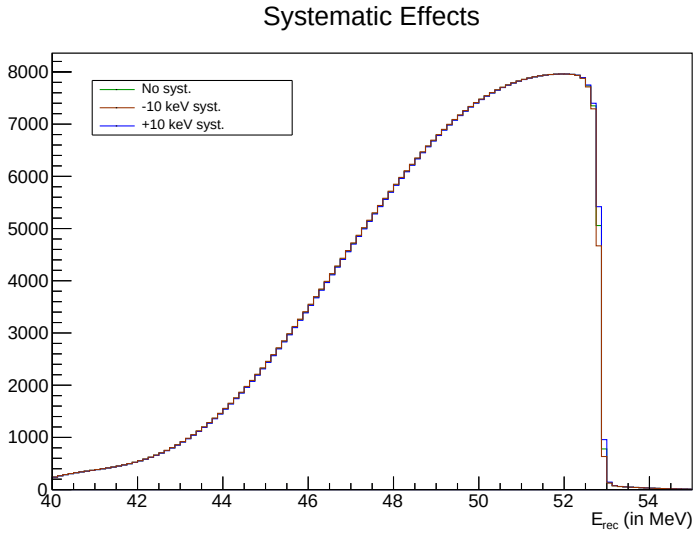

Figure 9.7: Simulated detector response assuming a shift in the reconstruction.

Another issue to be carefully considered are potential systematic effects. Two possible sources are on the one hand the detailed magnetic field map and on the other hand the material budget along the positron track. Deviations in the magnetic field map will cause an accordingly deviating momentum that would match the observed curvature of the track under the assumption of the offset magnetic field. The material along the positron track causes them to loose some of their energy and thus the positron as observed in the CDCH has lower momentum compared to the momentum when it was emitted.

The effect of a 10 keV shift in both directions is shown in Figure 9.7. The histograms are obtained by using the convolution of the theoretical NNLOLL predictions convoluted with the detector response which was modified to accommodate the appropriate shift. For most of the spectrum, there are no clear deviations visible.

However, at the kinematic endpoint, deviations in three bins are observable. Hence the sensitivity to the existence of the $\mu \to eX$ decay over most of the spectrum should be largely unaffected by a systematic shift. The estimation of the mass m_X of the Majoron is however affected in the usual way. The deviations at the endpoint suggest that the sensitivity for massless or almost massless Majorons is worsened in case of systematic shifts.

9.3 Estimation of the Sensitivity

The procedures to estimate the sensitivity are discussed. Finally the sensitivity to the $BR(\mu \to eX)$ is estimated considering a similar angular distribution as for Michel positrons. Eventually, the effects of a systematic shift of the absolute energy scale of the detector are discussed and their impact on the sensitivity estimated.

To estimate the sensitivity of the MEG II apparatus to the potential $\mu \to eX$ decay, the convoluted functions for the detector response are used in order to get a smoother result that avoids amplifying fluctuations that occurred during the full detector simulation. Moreover, based on the expected width of the Majoron peak, the data is binned with a bin width of 125 keV.

As a first and proper approach, the Feldman-Cousins (FC) method has been used to estimate the sensitivity [108]. In a more detailed way, the ROOT [100] Class `TFeldmanCousins` was used to estimate an upper limit for a given number of events under an expected number of background. The sensitivity is then estimated following the approach described by Feldman and Cousins through calculating the average upper limit to be expected from an ensemble of hypothetical experiments.

Given that the number of events in each bin will be large, their distribution is approximated by a Gaussian. To keep the computational effort within limits, the upper limits were evaluated for eleven discrete points evenly distributed within three standard deviations from the expectation value of no Majoron signal.

A first set assuming no systematic effects and a total of 10^6 reconstructed events is shown in Figure 9.8. As it soon became obvious that the computational power required for the full blown FC analysis is immense, the approximation

$$\bar{N}^i_{\text{U.L.}} \approx 1.76\sqrt{N^i_{\text{BG}}} \tag{9.2}$$

was used to estimate the average upper limit on the number $\bar{N}^i_{\text{U.L.}}$ of signal events in bin i given an expected number N^i_{BG} in that bin. The number 1.76 was obtained by fitting. A direct comparison shows, that the approximation appears to be accurate on the order of 1 %. This is deemed more than sufficient as the goal is an order of magnitude estimate of the sensitivity to estimate if MEG II can provide a competitive result on $BR(\mu \to eX)$.

Using this approximation, the expected sensitivity is estimated for up to 10^9 events. The results are shown in Figure 9.9. Note that these sensitivities do not yet consider any kind of systematic effects, i.e. they assume a perfectly well calibrated and understood detector. As expected, the sensitivity worsens for higher Majoron masses m_X corresponding to lower positron energies below 45 MeV.

Moreover, the bin width increases towards lower mass m_X. This is due to the function converting positron energies to Majoron masses. Each bin corresponds to the uniform 125 keV bin width in terms of positron momentum. This also implies that the estimated sensitivities below $8\,\text{MeV}/\text{c}^2$

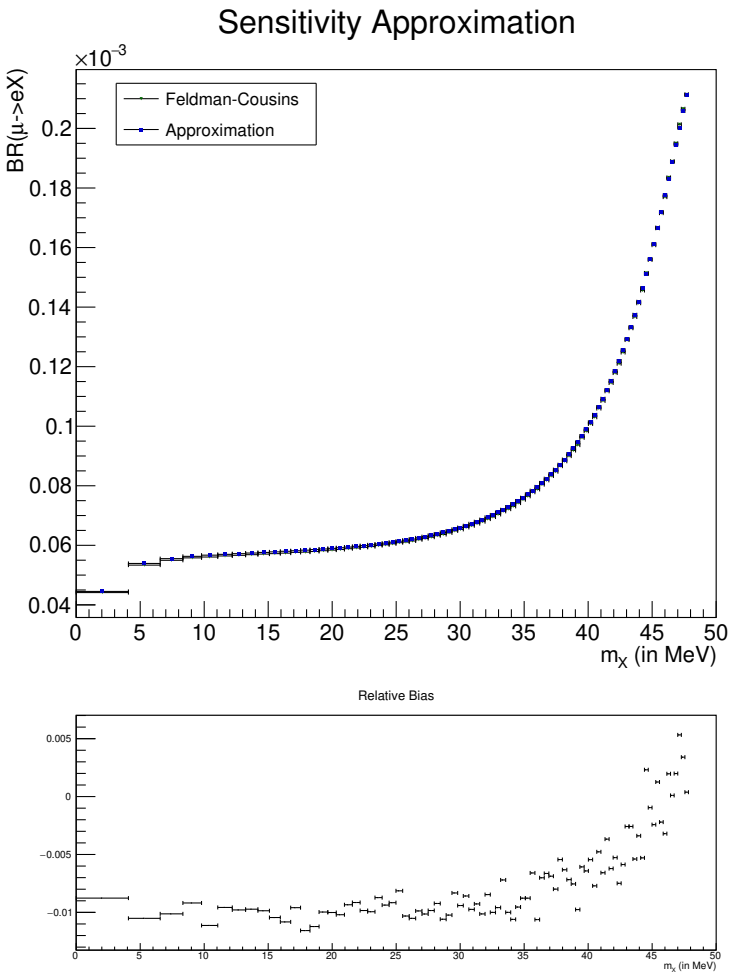

Figure 9.8: Sensitivity estimates without systematic effects on the reconstruction. Comparing full FC calculation to an approximation.

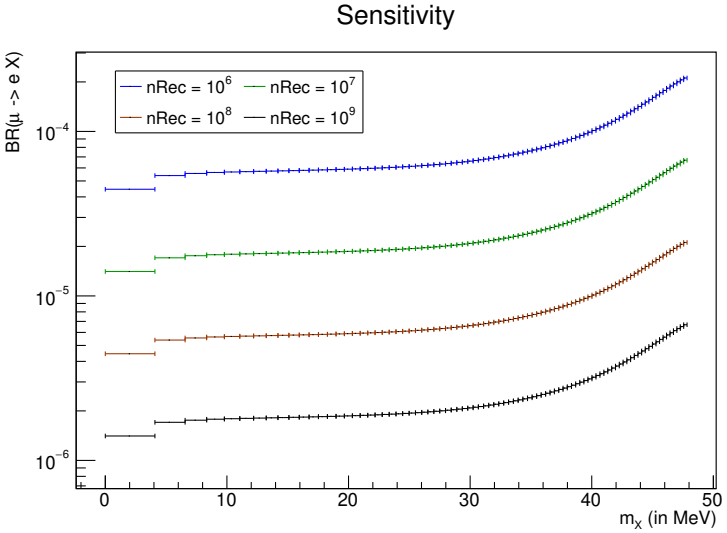

Figure 9.9: Approximated estimates of the sensitivity for different number of reconstructed events.

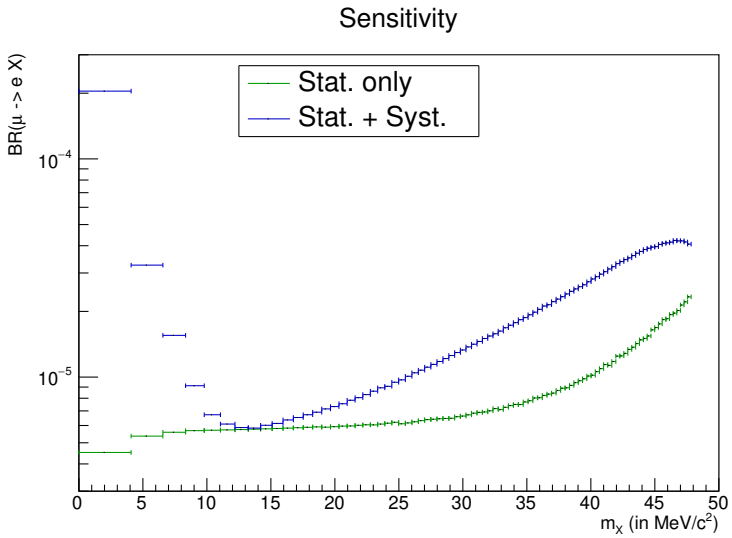

Figure 9.10: Estimated sensitivities without systematic effects and assuming systematic effects up to 10 keV. A number of 10^8 reconstructed events are assumed.

should be considered really carefully as these points correspond to bins at the kinematic endpoint where modelling uncertainties are largest and a systematic shift of the energy reconstruction has the largest impact. Nonetheless, this simulation shows that for about 10^7 to 10^8 reconstructed Michel events a competitive sensitivity for $BR(\mu \to eX)$ can be achieved.

In a final step of this feasibility study, the effect of a systematic shift as introduced in the previous section is investigated. To do so for each bin, the maximum of the estimated number of Michel events amongst the original and the two shifted histograms is considered. Then the full FC analysis is performed using the unperturbed background assumption. For this analysis a number of 10^8 reconstructed events is assumed in consistency with the previous observation. The results are shown in Figure 9.10.

As expected, a clear degradation in terms of sensitivity is observed for bins with $m_X < 8\,\mathrm{MeV/c^2}$ which are associated with the kinematic endpoint of the Michel spectrum. This underlines the importance of a proper detector characterisation and calibration of the absolute energy scale as this is the most effective way to increase the sensitivity in this region.

Moreover, for larger m_X, a degradation can be observed as well. Although this was expected, it is not nearly as bad as for the $m_X < 8\,\mathrm{MeV/c^2}$ region. This can be explained with the shape of the Michel spectrum in combination with the detector response, specifically with the detection efficiency. For the region in between, a decent performance and a competitive sensitivity is still expected.

Note that this study is incomplete, since it considers only the $V-A$ hypotheses, that the $\mu \to eX$ decay follows the same angular distribution as the ordinary Michel decay. This however does not need to be true and the coupling could be different. Assuming a hypothetical $V + A$ coupling, one could improve the signal to noise ratio by selecting an appropriate θ range to be analysed. Investigation in this direction were already initiated inside the collaboration.

Part IV

Conclusions

Chapter 10

Concluding Remarks

10.1 The MEG II Experiment

The SM is the most sophisticated and advanced theoretical description of particle physics available today. It withstood most experimental tests so far and no significant deviation from its predictions is experimentally observed apart from neutrino oscillations. However, there is cosmological evidence such as the matter-antimatter asymmetry in the universe and the existence of dark matter as well as the observations of some anomalies suggesting that the SM is not the final and ultimate theory of everything. Thus the search for physics beyond the SM continues.

MEG II is the latest experiment searching for the cLFV $\mu \to e\gamma$ decay with a sensitivity down to $BR(\mu \to e\gamma) = 6 \times 10^{-14}$. While measuring this decay provides immediate proof of the existence of physics beyond the SM, a new upper limit provides constraints on theories thereof.

10.2 Temperature Control in the Detector Hut

In order to achieve this goal, the experiment requires stable running conditions and careful calibrations. In order to stabilise the experimental environment, a PID control based on a Raspberry Pi was implemented to maintain the detector hut temperature stable. While it performed exceptionally well during the pre-engineering runs, the true test follows in the engineering run later this year when the experiment runs with the complete electronic set up.

10.3 Calibrations using Mott Scattered Positrons

The upgrade from MEG to MEG II included significant changes for the spectrometer. As part of this work, the calibration methods based on Mott scattered positrons was adapted to the new experiment and improved. While only minimal changes to the simulation code were required, large parts of the analysis code were changed.

Using a positron beam of 53 MeV, positrons impinging on the muon stopping target will result in scattered positrons of about the desired signal energy in the spectrometer. Selecting tracks that take at least two turns inside the CDCH, one can perform the double-turn analysis: analysing both turns of the same track individually and comparing the results of the separate fits.

Comparing the momentum differences results in a distribution that can be fitted reasonably well by two Gaussians. For the inner core function, a standard deviation of about 130 keV is obtained. This value is to be compared to the standard deviation of about 80 keV obtained from fitting differences between MC truth and reconstructed values. Similar observations are made for the angular positron variables.

This deviation can be explained by the combination of two factors. First, the double-turn analysis relies on two fitted parameters instead of one. Second, the double-turn method cuts a track in half and thus reduces the statistics in both parts. Especially the first turn usually contains fewer hits than the average fully reconstructed track.

A very similar concept is applied to the pTC, the so called double-cluster method. It searches for two pTC clusters which are matched to a track connecting them. After correcting for the time

of flight, the time difference between the measurements of these two individual clusters exhibit a width with a standard deviation of approximately 50 ps. This is very well consistent with the previously estimated time resolution below 40 ps for a single cluster.

For both methods, simulations suggest that the performance using Mott scattered positrons is closer to the expected performance for $\mu \to e\gamma$ signal positrons compared to ordinary Michel positrons. This proves the benefit of the effort to switch the main PiE5 beam from surface muons to 53 MeV positrons.

Additionally, the possibility to use beam positrons to calibrate the RDC was evaluated. While it is shown that this would be possible, the benefits of this method do not justify the efforts. This is due to the fact that a dedicated beam setting would be required for this method.

10.4 Upgrade of the CEX Auxiliary Detector

The CEX calibration relies on the detection of back to back photons from the reaction $\pi^- p \to \pi^0 n, \pi^0 \to \gamma\gamma$. These have an energy of either 55 MeV or 83 MeV. The first of these two values is close to the expected signal photon energy. To ascertain the back to back geometry, an auxiliary detector is needed.

Two materials are studied for an upgraded version of this auxiliary detector. BrilLanCe offers an outstanding light yield and extremely short decay time while LYSO is convincing due to its high density and correspondingly short radiation length and Moliere radius.

For currently available crystals, LYSO performs better according to the simulations. Coupling such a crystal to a double readout based on SiPMs results in a reconstruction of 55 MeV photons with a resolution of 1.7 % in energy, 30 ps in time, and a few mm in position under the assumption of low noise contribution. Based on these results, the decision to produce a prototype using a LYSO crystal with a length of 10 cm and a diameter of 7.5 cm was made.

Further, the performance of larger crystals was studied. Should they become available, they might be suitable candidates for future high precision measurements in the muon cLFV sector. It was shown that the energy resolution can be pushed clearly below 1 % without major detrimental effects on the reconstruction of the other variables of 55 MeV photons.

10.5 Exotic Physics Searches beyond the SM with MEG II

While the MEG II apparatus is designed for the search of the $\mu \to e\gamma$ decay, it is capable to search for further signatures of physics beyond the SM. As part of this work, two such candidates are presented. First, an investigation of what is referred to as the beryllium anomaly is planned. Second, the search for the decay $\mu \to eX$ where X refers to a yet unknown boson can be performed.

The beryllium anomaly investigation is planned for the upcoming maintenance period of the main proton accelerator at PSI in the beginning of 2022. For this purpose, the CW beam line usually used for XEC calibrations has to be modified by an appropriate vacuum chamber around a new target structure holding a dedicated lithium oxide target.

Furthermore, the magnetic field has to be reduced by about a factor six to allow the emitted electron-positron pair to reach the MEG II spectrometer. With all those adaptions, the MEG II apparatus should be able to collect enough statistics within a few days of data acquisition to perform measurements that are competitive with the measurements by Krasznahorkay et al. [3].

Including the time used to implement the adaptions of the MEG II apparatus, the time required will be on the order of a few weeks. This is still much shorter than the scheduled maintenance break and a result can hopefully be provided in 2022.

The investigation of the decay channel $\mu \to eX$ will be performed on the whole Michel data acquired over the whole running period of the MEG II experiment. Competitive results are to be obtained once 10^7 to 10^8 events are reconstructed. In order to get an adequate sensitivity towards low m_X the absolute energy scale and the response of the detector needs to be perfectly well understood.

Bibliography

[1] A. M. Baldini et al. (MEG Collaboration), *Search for the lepton flavour violating decay $\mu^+ \to e^+\gamma$ with the full dataset of the MEG experiment*, Eur. Phys. J. C **76** (2016), 434.

[2] A. M. Baldini et al. (MEG II Collaboration), *The design of the MEG II experiment*, Eur. Phys. J. C **78** (2018), 380.

[3] A. J. Krasznahorkay et al., *Observation of Anomalous Internal Pair Creation in ^{8}Be: A Possible Indication of a Light, Neutral Boson*, Phys. Rev. Lett. **116** (2016), 042501.

[4] S. L. Glashow, *Partial-symmetries of weak interactions*, Nucl. Phys. **22** (1961), 579.

[5] S. Weinberg, *A Model of Leptons*, Phys. Rev. Lett. **19** (1967), no. 21, 1254.

[6] G. Aad et al. (ATLAS Collaboration, *Observation of a new particle in the search for the Standard Model Higgs boson with the ATLAS detector at the LHC*, Phys. Lett. B **716** (2012), no. 1, 1.

[7] S. Chatrchyan et al. (CMS Collaboration), *Observation of a new boson at a mass of 125 GeV with the CMS experiment at the LHC*, Phys. Lett. B **716** (2012), no. 1, 30.

[8] Y. Fukuda et al. (The Super-Kamiokande Collaboration), *Measurement of the Flux and Zenith-Angle Distribution of Upward Throughgoing Muons by Super-Kamiokande*, Phys. Rev. Lett. **82** (1999), no. 13, 2644.

[9] Q. R. Ahmad et al. (SNO Collaboration), *Direct Evidence for Neutrino Flavor Transformation from Neutral-Current Interactions in the Sudbury Neutrino Observatory*, Phys. Rev. Lett. **89** (2002), no. 1, 011301.

[10] K. et al. (KamLAND Collaboration) Eguchi, *First Results from KamLAND: Evidence for Reactor Antineutrino Disappearance*, Phys. Rev. Lett. **90** (2003), no. 2, 021802.

[11] A. Crivellin et al., *PSI/UZH Workshop: Impact of $B \to \mu^+\mu^-$ on New Physics Searches*, arXiv:1803.10097 [hep-ph] (2018).

[12] B. Abi et al. (Muon $g-2$ Collaboration), *Measurement of the Positive Muon Anomalous Magnetic Moment to 0.46 ppm*, Phys. Rev. Lett. **126** (2021), no. 14, 141801.

[13] K. Arndt et al. (Mu3e Collaboration), *Technical design of the phase I Mu3e experiment*, arXiv:2009.11690v2 [physics.ins-det] (2020).

[14] L. Bartoszek et al., *Mu2e Technical Design Report*, arXiv:1501.05241 [physics.ins-det] (2015).

[15] R. Abramishvili et al. (COMET Collaboration), *COMET Phase-I Technical Design Report*, Prog. Theor. Exp. Phys. **2020** (2020), 033C01.

[16] A. Strumia R. Barbieri, L. Hall, *Violations of lepton flavour and CP in supersymmetric unified theories*, Nucl. Phys. B **445** (1995), no. 2, 219.

[17] F. Kirk, *Explaining the Cabibbo Angle Anomaly and Lepton Flavour Universality Violation in Tau Decays With a Singly-Charged Scalar Singlet*, arXiv:2105.06734 [hep-ph] (2021).

[18] G. M. Pruna, A. Signer, *Lepton-flavour violating decays in theories with dimension 6 operators*, EPJ Web of Conferences **118** (2016), 01031.

[19] A. Signer G. M. Pruna, *The $\mu \to e\gamma$ decay in a systematic effective field theory approach with dimension 6 operators*, J. High Energ. Phys **2014** (2014), 14.

[20] P. Kunze, *Untersuchung der Ultrastrahlung in der Wilsonkammer*, Zeitschrift für Physik **83** (1933), 1.

[21] C. Anderson, S. Neddermeyer, *Cloud Chamber Observations of Cosmic Rays at 4300 Meters Elevation and Near Sea-Level*, Phys. Rev. **50** (1936), 263.

[22] S. Neddermeyer, C. Anderson, *Note on the Nature of Cosmic-Ray Particles*, Phys. Rev. **51** (1937), 884.

[23] J. Street, E. Stevenson, *New Evidence for the Existence of a Particle of Mass Intermediate Between the Proton and Electron*, Phys. Rev. **52** (1937), 1003.

[24] S. Neddermeyer, C. Anderson, *Nature of Cosmic-Ray Particles*, Rev. Mod. Phys. **11** (1939), 191.

[25] B. Rossi, N. Nereson, *Experimental Determination of the Disintegration Curve of Mesotrons*, Phys. Rev. **62** (1942), 417.

[26] B. Rossi, N. Nereson, *Further Measurements on the Disintegration Curve of Mesotrons*, Phys. Rev. **64** (1943), 199.

[27] C. Anderson, S. Neddermeyer, *Mesotron (Intermediate Particle) as a Name for the New Particles of Intermediate Mass*, Nature **142** (1938), 878.

[28] C. Anderson et al., *On the Mass and the Disintegration Products of the Mesotron*, Phys. Rev. **72** (1947), 724.

[29] J. Steinberger, *On the Range of Electrons in Meson Decay*, Phys. Rev. **74** (1948), 500.

[30] R. Leighton et al., *The Energy Spectrum of the Decay Particles and the Mass and Spin of the Mesotron*, Phys. Rev. **75** (1949), 1432.

[31] L. Michel, *Interaction between Four Half-Spin Particles and the Decay of the μ-Meson*, Proc. Phys. Soc. A **63** (1950), 514.

[32] E. Hincks, B. Pontecorvo, *Search for Gamma-Radiation in the 2.2-Microsecond Meson Decay Process*, Phys. Rev. **73** (1948), 257.

[33] R. Sard, E. Althaus, *A Search for Delayed Photons from Stopped Sea Level Cosmic-Ray Mesons*, Phys. Rev. **74** (1948), 1364.

[34] S. Parker, H. L. Anderson, C. Rey, *Search for the Decay $\mu^+ \to e^+ + \gamma^*$*, Phys. Rev. **133** (1964), no. 3B, B768.

[35] H. P. Povel et al., *A new upper limit for the decay $\mu^+ \to e^+ + \gamma^*$*, Phys. Lett. **72B** (1977), no. 2, 183.

[36] R. D. Bolton et al., *Search for rare muon decays with the Crystal Box detector*, Phys. Rev. D **38** (1988), no. 7, 2077.

[37] M. Ahmed et al. (MEGA Collaboration), *Search for the lepton-family-number nonconserving decay $\mu^+ \to e^+\gamma$*, Phys. Rev. D **65** (2002), 112002.

[38] J. Adam et al. (MEG Collaboration), *The MEG detector for $\mu^+ \to e^+\gamma$ decay search*, Eur. Phys. J. C **73** (2013), 2365.

[39] Paul Scherrer Institute, *$\pi E5$ Beamline*, `https://www.psi.ch/en/sbl/pie5-beamline` - 24.5.2021.

[40] A. M. Baldini et al. (MEG Collaboration), *Search for the lepton flavour violating decay $\mu^+ \to e^+\gamma$ with the full dataset of the MEG experiment*, Eur. Phys. J. C **76** (2016), 434.

[41] L. M. Barkov et al, *Search for $\mu^+ \to e^+\gamma$ down to 10^{-14} branching ratio*, 1999, Research Proposal to Paul Scherrer Institute, `https://meg.web.psi.ch/docs/prop_psi` - 17.08.2021.

[42] A. M. Baldini et al. (MEG Collaboration), *Search for lepton flavour violating muon decay mediated by a newlight particle in the MEG experiment*, Eur. Phys. J. C **80** (2020), 858.

[43] Y. Chikashige, R.N. Mohapatra, R.D. Peccei, *Are there real goldstone bosons associated with broken lepton number?*, Phys. Lett. B **98** (1981), no. 4, 265.

[44] G.B. Gelmini, M. Roncadelli, *Left-handed neutrino mass scale and spontaneously broken lepton number*, Phys. Lett. B **99** (1981), no. 5, 411.

[45] J. Schechter, J. W. F. Valle, *Neutrino decay and spontaneous violation of lepton number*, Phys. Rev. D **25** (1982), no. 3, 774.

[46] R. D. Peccei, H. R. Quinn, CP *Conservation in the Presence of Pseudoparticles*, Phys. Rev. Lett. **38** (1977), no. 25, 1440.

[47] R. D. Peccei, H. R. Quinn, *Constraints imposed by* CP *conservation in the presence of pseudoparticles*, Phys. Rev. D **16** (1977), no. 6, 1791.

[48] S. Weinberg, *A New Light Boson?*, Phys. Rev. Lett. **40** (1978), no. 4, 223.

[49] F. Wilczek, *Problem of Strong P and T Invariance in the Presence of Instantons*, Phys. Rev. Lett. **40** (1978), no. 5, 279.

[50] C. Cornella, P. Paradisi, O. Sumensari, *Hunting for ALPs with lepton flavor violation* , J. High Energ. Phys. **2020** (2020), 158.

[51] M. Bauer et al., *Axionlike Particles, Lepton-Flavor Violation, and a New Explanation of a_μ and a_e*, Phys. Rev. Lett. **124** (2020), no. 21, 211803.

[52] D. B. Reiss, *Can the family group be a global symmetry?*, Phys. Lett. B **115** (1982), no. 3, 217–220.

[53] F. Wilczek, *Axions and Family Symmetry Breaking*, Phys. Rev. Lett. **49** (1982), no. 21, 1549.

[54] J. E. Kim, *Light pseudoscalars, particle physics and cosmology*, Phys. Reports **150** (1987), no. 1, 1.

[55] J. Jaeckel, *A family of WISPy dark matter candidates*, Phys. Lett. B **732** (2014), 1.

[56] K. Tsumura, L. Velasco-Sevilla, *Phenomenology of flavon fields at the LHC*, Phys. Rev. D **81** (2010), no. 3, 036012.

[57] M. Bauer, T. Schell, T. Plehn, *Hunting the flavon*, Phys. Rev. D **94** (2016), no. 5, 056003.

[58] Y. Ema et al., *Flaxion: a minimal extension to solve puzzles in the standard model*, J. High Energ. Phys. **2017** (2017), 96.

[59] O. Davidi et al., *The hierarchion, a relaxion addressing the Standard Model's hierarchies*, J. High Energ. Phys. **2018** (2018), 153.

[60] R.Bayes et al. (TWIST Collaboration), *Search for two body muon decay signals*, Phys. Rev. D **91** (2015), no. 5, 052020.

[61] A. Jodidio et al., *Search for right-handed currents in muon decay*, Phys. Rev. D **34** (1986), no. 7, 1967.

[62] R.S. Henderson et al., *Precision planar drift chambers and cradle for the twist muon decay spectrometer*, Nucl. Instr. Meth. A **548** (2005), no. 3, 306.

[63] F Petriello C. Anastasiou, K. Melnikov, *The electron energy spectrum in muon decay through $\mathcal{O}(\alpha^2)$*, J. High Energ. Phys. **2007** (2007), no. 09, 014.

[64] T. Engel, A. Signer, Y. Ulrich, *A subtraction scheme for massive QED*, J. High Energ. Phys. **2020** (2020), 85.

[65] P. Banerjee, T. Engel, A. Signer, Y. Ulrich, *QED at NNLO with McMule*, SciPost Phys. **9** (2020), no. 2, 27.

[66] A. Gurgone, *Search for $\mu \to eX$ with the MEG II experiment: QED corrections with* McMule *and expected sensitivity* , Master's thesis, U. Pisa, 2021.

[67] J. Gulyás et al., *A pair spectrometer for measuring multipolarities of energetic nuclear transitions*, Nucl. Instr. Meth. A **808** (2016), 21.

[68] A. J. Krasznahorkay et al., *New evidence supporting the existence of the hypothetic X17 particle*, arxiv:1910.10459v1 [nucl-ex] (2019).

[69] G. A. Miller X. Zhang, *Can nuclear physics explain the anomaly observed in the internal pair production in the Beryllium-8 nucleus?*, arxiv:1703.04588v1 [nucl-th] (2017).

[70] A. Aleksejevs et al., *A Standard Model Explanation for the "ATOMKI Anomaly"*, arXiv:2102.01127v1 [hep-ph] (2021).

[71] A. M. Baldini et al. (MEG II Collaboration), *MEG Upgrade Proposal*, arXiv:1301.7225v2 [physics.ins-det] (2013).

[72] M. Conversi, E. Pancini, O. Piccioni, *On the Disintegration of Negative Mesons*, Phys. Rev. **71** (1947), no. 3, 209.

[73] G.M Pruna, A. Signer, Y. Ulrich, *Fully differential NLO predictions for the radiative decay of muons and taus*, Phys. Lett. B **772** (2017), 452.

[74] M. Chiappini, *Internal Communication.*

[75] G.F. Tassielli et al., *The drift chamber of the MEG II experiment*, J. Instr. **15** (2020), no. 09, C09051.

[76] M. Francesconi et al., *A new generation of integrated trigger and read out system for the MEG II experiment*, 5th International Conference on Modern Circuits and Systems Technologies, MOCAST 2016.

[77] S. Ogawa, *Internal Communication.*

[78] M. Francesconi, S. Ritt, *Private communications.*

[79] Texas Instruments, *LM35 Precision Centigrade Temperature Sensors*, `https://www.ti.com/lit/ds/symlink/lm35.pdf` - 11.6.2021.

[80] U. Hartmann, *Private Communication.*

[81] cesanta, *Mongoose - Embedded Web Server / Embedded Networking Library*, `https://github.com/cesanta/mongoose` - 11.06.2021.

[82] J. G. Ziegler, N.B. Nichols, *Optimum Settings for Automatic Controlers*, Trans. ASME **64** (1942), 759.

[83] N. F. Mott, *The scattering of fast electrons by atomic nuclei*, Proc. R. Soc. Lond. A **124** (1929), 425.

[84] R. Hofstadter, *Nuclear and Nucleon Scattering of High-Energy Electrons*, Annu. Rev. Nucl. Sci **7** (1957), 231.

[85] G. Rutar, *In Search of Charged Lepton Flavor Violating Decays at PSI*, Ph.D. thesis, Eidgenössische Technische Hochschule Zürich, 2017.

[86] R. Hofstadter, *Electron Scattering and Nuclear Structure*, Rev. Mod. Phys **28** (1956), 214.

[87] S. Agostinelli et al. (GEANT4 Collaboration), GEANT4—*a simulation toolkit*, Nucl. Instr. Meth. A **506** (2003), 250.

[88] P. W. Cattaneo, *The architecture of MEG simulation and analysis software*, Eur. Phys. J. Plus **126** (2011), 60.

[89] G. Boca et al., *The laser-based time calibration system for the MEG II pixelated Timing Counter*, Nucl. Instr. Meth. A **947** (2019), 162672.

[90] A. Papa, P. Schwendimann, *A First Large Calorimeter Prototype Based on Lanthanum Bromide Coupled to Silicon Photomultipliers: Status and Prospects*, Nucl. Instr. Meth. A **936** (2019), 130.

[91] A. Papa, P. Schwendimann, *Development of new large calorimeter prototypes based on $LaBr_3$(Ce) and LYSO crystals coupled to silicon photomultipliers: A direct comparison*, Nucl. Instr. Meth. A **958** (2020), 162999.

[92] P. Schwendimann, A. Papa, *Study of 3D calorimetry based on LYSO or $LaBr_3$:Ce crystals for future high energy precision physics*, J. Instr. **15** (2020), C06018.

[93] C. Patrignani et al. (Particle Data Group), *Review of Particle Physics*, Chin. Phys. C **40** (2016), no. 10, 100001.

[94] Saint-Gobain Ceramics & Plastics Inc., *Lanthanum Bromide and Enhanced Lanthanum Bromide Scintillation Materials*, 2017.

[95] A. Papa, *Private communication with Saint-Gobain.*

[96] EPIC-Crystal, *LYSO(Ce) Scintillator*, available online, `https://www.epic-crystal.com/oxide-scintillators/lyso-ce-scintillator.html` - 8.6.2021.

[97] D. Groom, *Atomic and Nuclear Properties of Materials*, `https://pdg.lbl.gov/2021/AtomicNuclearProperties/index.html` - 8.6.2021.

[98] Hamamatsu Photonics, *MPPC (Multi-Pixel Photon Counter) S13360 Series*, 2016.

[99] sensL, *J-Series High PDE and Timing Resolution, TSV Package*, 2017.

[100] R. Brun, F. Rademakers, *ROOT: An object oriented data analysis framework*, Nucl. Instrum. Meth. A **389** (1997), 81.

[101] A. Papa, *Private discussion.*

[102] `https://www.epic-crystal.com/` - 13.6.2021.

[103] A. Papa, *Private communication with Epic-Crystal when placing the order.*

[104] A. Papa, *Internal presentation.*

[105] G. Cavoto et al., *Proposal for a search of the $X(17\,\mathrm{MeV})$ boson with the MEG-II apparatus*, 2020, internal document.

[106] A. Papa, *Private communication.*

[107] A. M. Baldini et al. (MEG Collaboration), *Muon polarization in the MEG experiment: predictions and measurements*, Eur. Phys. J. C **76** (2016), 223.

[108] G. J. Feldman, R. D. Cousins, *Unified approach to the classical statistical analysis of small signals*, Phys. Rev. D **57** (1998), no. 7, 3873.

Acronyms

AIF	Annihilation In Flight
BR	Branching Ratio
BTS	Beam Transport Solenoid
CEX	Charge EXchange (referring to $\pi^- p^+ \to \pi^0 n$)
COBRA	COnstant Bending RAdius (refers to MEG and MEG II magnet)
CDCH	Cylindric Drift CHamber
C.L.	Confidence Level
cLFV	Charged Lepton Flavour Violation (*or Violating*)
CRC	Cosmic Ray Counter
CW	Cockcroft-Walton (referring to an accelerator)
DAQ	Data AcQuisition
DS	DownStream
FNAL	Fermi National Accelerator Laboratory
GEM, GEM4	Generator of Events for MEG (refers to MEG simulation program)
IPC	Internal Pair Conversion
LO	Leading Order
JPARC	Japan Proton Accelerator Research Complex
LXe	Liquid Xenon
LY	Light Yield
LYSO	Lutetium Yttrium OxyorthoSilicate
MC	Monte Carlo (referring to simulations)
MPPC	Multi-Pixel Photon Counter
MWPC	MultiWire Proportional Chamber
NLO	Next to Leading Order (referring to theory calculations)
NNLO	Next to Next to Leading Order (referring to theory calculations)
NNLOLL	NNLO plus Leading Logarithms (referring to theory calculations)
PDE	PhotoDetection Efficiency
PMT	PhotoMultiplier Tube
PSI	Paul Scherrer Institut
pTC	Pixelated Timing Counter
RDC	Radiative Decay Counter
RMD	Radiative Muon Decay ($\mu \to e\nu\nu\gamma$)
SIN	Schweizer Institut für Nuklearforschung, merged 1988 into PSI
SiPM	Silicon PhotoMultiplier
SM	Standard Model (of particle physics)
US	UpStream
XEC	XEnon Calorimeter